

# Adaptive Modeling of Wave Propagation in Heterogeneous Elastic Solids

Albert Romkes and J. Tinsley Oden

*Institute for Computational Engineering and Sciences  
The University of Texas at Austin  
Austin, Texas 78712*

May 2003

**Abstract:** This document presents the results of a detailed research investigation on a fundamental problem in wave mechanics: the propagation of stress waves in heterogeneous elastic solids. This phenomenon is fundamental to many disciplines in engineering and mathematical physics: seismology, earthquake engineering, structure acoustics, composite materials, and many other areas. The theory and methodologies of hierarchical modeling of heterogeneous materials are extended to elastodynamic cases to make possible the control of the modeling error in the local average stress. One-dimensional steady state and transient applications are given.

# Report Documentation Page

*Form Approved*  
*OMB No. 0704-0188*

Public reporting burden for the collection of information is estimated to average 1 hour per response, including the time for reviewing instructions, searching existing data sources, gathering and maintaining the data needed, and completing and reviewing the collection of information. Send comments regarding this burden estimate or any other aspect of this collection of information, including suggestions for reducing this burden, to Washington Headquarters Services, Directorate for Information Operations and Reports, 1215 Jefferson Davis Highway, Suite 1204, Arlington VA 22202-4302. Respondents should be aware that notwithstanding any other provision of law, no person shall be subject to a penalty for failing to comply with a collection of information if it does not display a currently valid OMB control number.

1. REPORT DATE <b>MAY 2003</b>	2. REPORT TYPE	3. DATES COVERED -			
4. TITLE AND SUBTITLE <b>Adaptive Modeling of Wave Propagation in Heterogeneous Elastic Solids</b>		5a. CONTRACT NUMBER			
		5b. GRANT NUMBER			
		5c. PROGRAM ELEMENT NUMBER			
6. AUTHOR(S)		5d. PROJECT NUMBER			
		5e. TASK NUMBER			
		5f. WORK UNIT NUMBER			
7. PERFORMING ORGANIZATION NAME(S) AND ADDRESS(ES) <b>Office of Naval Research, One Liberty Center, 875 North Randolph Street Suite 1425, Arlington, VA, 22203-1995</b>		8. PERFORMING ORGANIZATION REPORT NUMBER			
9. SPONSORING/MONITORING AGENCY NAME(S) AND ADDRESS(ES)		10. SPONSOR/MONITOR'S ACRONYM(S)			
		11. SPONSOR/MONITOR'S REPORT NUMBER(S)			
12. DISTRIBUTION/AVAILABILITY STATEMENT <b>Approved for public release; distribution unlimited</b>					
13. SUPPLEMENTARY NOTES <b>The original document contains color images.</b>					
14. ABSTRACT <b>see report</b>					
15. SUBJECT TERMS					
16. SECURITY CLASSIFICATION OF:			17. LIMITATION OF ABSTRACT	18. NUMBER OF PAGES	19a. NAME OF RESPONSIBLE PERSON
a. REPORT <b>unclassified</b>	b. ABSTRACT <b>unclassified</b>	c. THIS PAGE <b>unclassified</b>		<b>82</b>	

# Contents

<b>1</b>	<b>Introduction</b>	<b>1</b>
<b>2</b>	<b>The Elastic Wave Problem</b>	<b>3</b>
2.1	Model Problem and Notations . . . . .	3
2.2	The Weak Formulation . . . . .	5
<b>3</b>	<b>Modeling Error Estimation</b>	<b>6</b>
3.1	Exact and Approximate Material Models . . . . .	6
3.2	The Modeling Errors . . . . .	7
3.3	Elliptic Error Representations . . . . .	9
3.4	Computable Upper and Lower Error Bounds . . . . .	10
3.5	Modeling Error Estimates . . . . .	13
3.5.1	Local Error Estimates . . . . .	13
3.5.2	Global Error Estimates . . . . .	15
3.6	Numerical Experiments . . . . .	17
3.6.1	Steady State Case I: a Composite Material with Periodic Microstructure . . . . .	17
3.6.2	Steady State Case II: Effect of Damping . . . . .	30
3.6.3	Steady State Case III: a Non-Uniformly Layered Material . . . . .	32
3.6.4	Transient Test Problem . . . . .	40
<b>4</b>	<b>Adaptive Modeling of the Wave Problem</b>	<b>45</b>
4.1	Modeling Error Indicators . . . . .	45
4.2	The Adaptive Algorithm . . . . .	46
4.3	Numerical Examples . . . . .	48
4.3.1	Steady State Waves . . . . .	48
4.3.2	Transient Bandlimited Waves . . . . .	57
<b>5</b>	<b>Concluding Remarks</b>	<b>67</b>
	<b>References</b>	<b>69</b>
	<b>Appendix A - Derivation of Optimal Lower Bounds <math>\eta_{\text{low}(,i)}^\pm</math></b>	<b>72</b>

# Tables

3.1	Effectivity indices with respect to $\ \hat{\mathbf{e}}_1\ _{\mathcal{H}}$ and $\ \hat{\varepsilon}_1\ _{\mathcal{H}}$ (upper part), and $\ \hat{\mathbf{e}}_0\ _{\mathcal{H}}$ and $\ \hat{\varepsilon}_0\ _{\mathcal{H}}$ (lower part), for a periodically layered material and a radial frequency of 500 Hz. . . . .	25
3.2	Effectivity indices of upper and lower bounds to the terms coming from the polarization formula expansion (3.16), for a periodically layered material, and for radial frequency of 500 Hz. . . . .	25
3.3	Relative error and effectivity indices of the modeling error estimators, for a periodically layered material, and radial frequency of 500 Hz. . . . .	25
3.4	Effectivity indices with respect to $\ \hat{\mathbf{e}}_1\ _{\mathcal{H}}$ and $\ \hat{\varepsilon}_1\ _{\mathcal{H}}$ (upper part), and $\ \hat{\mathbf{e}}_0\ _{\mathcal{H}}$ and $\ \hat{\varepsilon}_0\ _{\mathcal{H}}$ (lower part), for a periodically layered material and radial frequency of 1000 Hz. . . . .	26
3.5	Effectivity indices with respect to $\ \hat{\mathbf{e}}_1\ _{\mathcal{H}}$ and $\ \hat{\varepsilon}_1\ _{\mathcal{H}}$ (upper part), and $\ \hat{\mathbf{e}}_0\ _{\mathcal{H}}$ and $\ \hat{\varepsilon}_0\ _{\mathcal{H}}$ (lower part), for a periodically layered material and radial frequency of 2000 Hz. . . . .	27
3.6	Effectivity indices with respect to $\ \hat{\mathbf{e}}_1\ _{\mathcal{H}}$ and $\ \hat{\varepsilon}_1\ _{\mathcal{H}}$ (upper part), and $\ \hat{\mathbf{e}}_0\ _{\mathcal{H}}$ and $\ \hat{\varepsilon}_0\ _{\mathcal{H}}$ (lower part), for a periodically layered material and radial frequency of 4000 Hz. . . . .	27
3.7	Effectivity indices of upper and lower bounds to the terms coming from the polarization formula expansion (3.16), for a periodically layered material and radial frequency of 1000 Hz. . . . .	28
3.8	Effectivity indices of upper and lower bounds to the terms coming from the polarization formula expansion (3.16), for a periodically layered material and radial frequency of 2000 Hz. . . . .	28
3.9	Effectivity indices of upper and lower bounds to the terms coming from the polarization formula expansion (3.16), for a periodically layered material and radial frequency of 4000 Hz. . . . .	28
3.10	Relative error and effectivity indices of the modeling error estimators, for a periodically layered material and radial frequency of 1000 Hz. . . . .	29
3.11	Relative error and effectivity indices of the modeling error estimators, for a periodically layered material and radial frequency of 2000 Hz. . . . .	29
3.12	Relative error and effectivity indices of the modeling error estimators, for a periodically layered material and radial frequency of 4000 Hz. . . . .	29
3.13	Effectivity indices with respect to $\ \hat{\mathbf{e}}_1\ _{\mathcal{H}}$ and $\ \hat{\varepsilon}_1\ _{\mathcal{H}}$ (upper part), and $\ \hat{\mathbf{e}}_0\ _{\mathcal{H}}$ and $\ \hat{\varepsilon}_0\ _{\mathcal{H}}$ (lower part), for a periodically layered material and a radial frequency of 4000 Hz. . . . .	30

3.14	Effectivity indices of upper and lower bounds to the terms coming from the polarization formula expansion (3.16), for a periodically layered material and a radial frequency of 4000 Hz. . . . .	31
3.15	Relative error and effectivity indices of the modeling error estimators, for a periodically layered material and a radial frequency of 4000 Hz. . .	31
3.16	Effectivity indices with respect to $\ \hat{\mathbf{e}}_1\ _{\mathcal{H}}$ and $\ \hat{\varepsilon}_1\ _{\mathcal{H}}$ (upper part), and $\ \hat{\mathbf{e}}_0\ _{\mathcal{H}}$ and $\ \hat{\varepsilon}_0\ _{\mathcal{H}}$ (lower part) for a non-uniformly layered material. . . .	38
3.17	Effectivity indices of upper and lower bounds to the terms coming from the polarization formula expansion (3.16), for a non-uniformly layered material. . . . .	38
3.18	Relative error and effectivity indices of the modeling error estimators, for a non-uniformly layered material. . . . .	39
3.19	Bounds on the modeling error and error estimators for the transient test problem, for $t = [0, 0.05]$ s. . . . .	44
4.1	Data review of the adaptive modeling process for the steady state wave with a radial frequency of 200 Hz. . . . .	50
4.2	Data review of the adaptive modeling process for the steady state wave with a radial frequency of 3000 Hz. . . . .	52
4.3	Data review of the adaptive modeling process for the steady state wave with a radial frequency of 4000 Hz. . . . .	55
4.4	Relative errors and effectivity indices for the estimator $\gamma_{est,t}$ after the first iteration step, when $\omega_{\max} = 1000$ Hz. . . . .	58
4.5	Summary on iterative adaption process for $\omega_{\max}=1000$ Hz. . . . .	60
4.6	Ratios of the upper bounds on the error and the quantity of interest, and effectivity indices for the upper bounds on the error estimator, after the first iteration step. . . . .	61
4.7	Ratios of the upper bounds on the error and the quantity of interest, and effectivity indices for the upper bounds on the error estimator, after the last iteration step. . . . .	61

# Figures

2.1	The model problem. . . . .	4
3.1	Steady state problem for a composite material with periodic microstructure. . . . .	19
3.2	Steady state solutions of a periodically layered material with impedance ratio $\tau = 7.30$ and for a radial frequency of 500 Hz, normalized by $\ \hat{\mathbf{u}}_0\ _{L^\infty(\Omega)}$ and $\ \hat{\mathbf{p}}_0\ _{L^\infty(\Omega)}$ . . . . .	20
3.3	Steady state solutions of a periodically layered material with impedance ratio $\tau = 7.30$ and for a radial frequency of 1000 Hz, normalized by $\ \hat{\mathbf{u}}_0\ _{L^\infty(\Omega)}$ and $\ \hat{\mathbf{p}}_0\ _{L^\infty(\Omega)}$ . . . . .	21
3.4	Steady state solutions of a periodically layered material with impedance ratio $\tau = 7.30$ and a radial frequency of 2000 Hz, normalized by $\ \hat{\mathbf{u}}_0\ _{L^\infty(\Omega)}$ and $\ \hat{\mathbf{p}}_0\ _{L^\infty(\Omega)}$ . . . . .	22
3.5	Steady state solutions of a periodically layered material with impedance ratio $\tau = 7.30$ and a radial frequency of 4000 Hz, normalized by $\ \hat{\mathbf{u}}_0\ _{L^\infty(\Omega)}$ and $\ \hat{\mathbf{p}}_0\ _{L^\infty(\Omega)}$ . . . . .	23
3.6	Steady state problem for a non-uniformly layered material. . . . .	32
3.7	Steady state solutions of a non-uniformly layered material for a radial frequency of 1000 Hz, normalized by $\ \hat{\mathbf{u}}_0\ _{L^\infty(\Omega)}$ and $\ \hat{\mathbf{p}}_0\ _{L^\infty(\Omega)}$ . . . . .	34
3.8	Steady state solutions of a non-uniformly layered material for a radial frequency of 2000 Hz, normalized by $\ \hat{\mathbf{u}}_0\ _{L^\infty(\Omega)}$ and $\ \hat{\mathbf{p}}_0\ _{L^\infty(\Omega)}$ . . . . .	35
3.9	Steady state solutions of a non-uniformly layered material for a radial frequency of 3000 Hz, normalized by $\ \hat{\mathbf{u}}_0\ _{L^\infty(\Omega)}$ and $\ \hat{\mathbf{p}}_0\ _{L^\infty(\Omega)}$ . . . . .	36
3.10	Steady state solutions of a non-uniformly layered material for a radial frequency of 4000 Hz, normalized by $\ \hat{\mathbf{u}}_0\ _{L^\infty(\Omega)}$ and $\ \hat{\mathbf{p}}_0\ _{L^\infty(\Omega)}$ . . . . .	37
3.11	Transient test problem with initial displacement field. . . . .	41
3.12	Transient solutions due to an initial pulse at $x = 20$ m with width $\delta = 0.2$ m, normalized by the maximum displacement $ \mathbf{u}_0(x, t) $ , $x \in \Omega$ , $t \in [0, 0.05]$ . . . . .	42
3.13	Transient solutions for the stresses in the domain of interest, normalized by the maximum stress $ E_0 \frac{d\mathbf{u}_0}{dx}(x, t) $ , $x \in \Omega$ , $t \in [0, 0.05]$ . . . . .	43
4.1	Flow diagram of the adaptive modeling algorithm. . . . .	47
4.2	Steady state problem of a beam with 3 zones of inhomogeneities. . . . .	49
4.3	Snapshot solutions of the adaptive modeling analysis for the steady state wave, with $\omega=200$ Hz, normalized by $\ \mathbf{u}_0\ _{L^\infty(\Omega)}$ . . . . .	51

4.4	Snapshot solutions of the adaptive modeling analysis for the steady state wave, with $\omega=3000$ Hz. . . . .	53
4.5	Snapshot solutions of the adaptive modeling analysis for the steady state wave, with $\omega=4000$ Hz. . . . .	56
4.6	Transient problem of a beam with 4 zones of inhomogeneities. . . . .	58
4.7	Bandlimited wave, $\omega_{max} = 1000$ Hz: Comparison of the exact solution with the homogenized solution (left), and the adapted solution (right); all are normalized by maximum of $E\mathbf{d}u(x,t)/dx$ , $x \in \Omega$ , $t \in [0, 0.057]$ . . .	62
4.8	Bandlimited wave, $\omega_{max} = 2000$ Hz: Comparison of the exact solution with the homogenized solution (left), and the adapted solution (right); all are normalized by maximum of $E\mathbf{d}u(x,t)/dx$ , $x \in \Omega$ , $t \in [0, 0.057]$ . . .	64
4.9	Bandlimited wave, $\omega_{max} = 3000$ Hz: Comparison of the exact solution with the homogenized solution (left), and the adapted solution (right); all are normalized by maximum of $E\mathbf{d}u(x,t)/dx$ , $x \in \Omega$ , $t \in [0, 0.057]$ . . .	65
4.10	Bandlimited wave, $\omega_{max} = 4000$ Hz: Comparison of the exact solution with the homogenized solution (left), and the adapted solution (right); all are normalized by maximum of $E\mathbf{d}u(x,t)/dx$ , $x \in \Omega$ , $t \in [0, 0.057]$ . . .	66

# 1 Introduction

Today, the use of *composite* materials is wide spread in industrial and military applications. These materials generally exhibit a complex microstructure: mechanical, geometrical and topological features which are realized at scales small in comparison with characteristic dimensions of typical structural components. It is well known that these micro-scale features and the mechanical properties of subscale constituents govern the overall response and service life of the structure. Despite this popularity in engineering applications, the analysis of the response of such heterogeneous materials to service loads is a very complex undertaking and has been the subject of research for several decades.

For more than half a century, work on the mechanics of materials has focused on determining so-called effective properties: averaged or smoothed properties that reflect in some global sense the response of specimens of the material to external loads. These average properties are typically what are determined by standard laboratory tests, *e.g.*: extension, compression, or torsion of rods. A major goal of contemporary research has been to determine bounds on the various material parameters. Some of the most revered work in mechanics over several decades has been devoted to this subject. As well known examples, the works of Hill [14], Hashin and Shtrikman [13], Balendran and Nemat-Nasser [1], and Nemat-Nasser and Hori [15] are noted. The averaging methods also spawned new mathematical research into what is called homogenization of partial differential equations. The classical works by Bensoussan *et al* [5] and Sanchez-Palencia [23] are examples that provide a mathematical justification by assuming periodicity of the microstructure. In more recent literature, modern methods of imaging and computations have been used to derive effective properties of actual material specimens. Examples are the works done by Ghosh *et al* [10, 11] (Voronoi Cell Finite Element Method); Fu *et al* [8] (Boundary Element Method) or Terada *et al* [25] (using digital data of the microstructure, obtained by X-ray Computerized Tomography).

In a similar vein, a multi-scale approach has been used by Guedes and Kikuchi [12] and Terada and Kikuchi [24]. They use homogenization techniques to obtain overall properties for the macro-scale and include asymptotic corrections to account for micro-mechanical effects (periodicity of the microstructure is assumed). Ghosh, Lee and Moorthy [9] use a similar multi-scale technique to study elasto-plastic material behavior. Fish *et al* [6, 7] apply a multi-scale technique to problems of wave propagation through heterogeneous materials as well, but enhance the method by also introducing multiple temporal scales to capture the dispersion phenomenon caused by the material inhomogeneity.

All the previous approaches can be characterized by their restriction to materials

with periodic micro-structures. In recent years, a completely new line of research on heterogeneous materials has emerged in which full account of micro-mechanical features of materials can be made in predicting macro-mechanical behavior. This area is referred to as *Hierarchical Modeling* and involves the use of only enough micro-scale information to determine essential features of the macro response to within preset levels of accuracy. Homogenization is used only as a step in a broader algorithm. Oden and Zohdi [21] and Zohdi and coworkers [29, 28] introduced a hierarchical adaptive modeling method for problems in elastostatics based on global error bounds. The method is aimed at providing a hierarchy of descriptions of the physics (or scales), that can be used in different subdomains of the material. Instead of heuristically choosing a level of description for each subdomain, a mathematical tool in the form of *a posteriori* error estimates of the modeling error is used to identify what level of sophistication is needed in each subdomain.

The original method was referred to as the *Homogenized Dirichlet Projection Method* (HDPM). It involves two levels of descriptions: a homogenized macro description and the exact micro-mechanical description. The algorithm proceeds as follows: initially homogenized material properties are used throughout the entire domain; next, *a posteriori* error estimates of the modeling error are obtained and an iteration process is started in which in critical regions of the material the fine-scale problem is solved by using the homogenized solution as Dirichlet boundary data on the boundary of the subdomain; the iteration process continues by including more and more critical regions into the fine-scale analysis until the error estimate meets certain user-preset tolerances.

Where the previous procedure uses *global* error estimates, Oden and Vemaganti [19, 20, 26, 27] advanced this work by introducing the *Goal-Oriented Adaptive Local Solution Algorithm* (GOALS), where error estimates in *local* quantities of interest are used. Such estimates allow one to use *goal oriented* adaptive strategies, in which a model is adapted so as to yield accurate characterization of specific features of the response identified by the analyst.

As mentioned before, these works were all done within the framework of elastostatics. Recently, an extension of the GOALS philosophy to general goal oriented engineering applications has been proposed by Oden and Prudhomme [17, 18]. Their approach entails a residual-based analysis of the modeling error and has been inspired by the work of Becker and Rannacher [2] on goal oriented estimation of discretization errors.

This investigation presents an extension of the GOALS philosophy to the elastodynamic problem by extending the existing theory to cover complex-valued solutions and sesquilinear forms encountered in frequency-domain formulations of the wave equation. The notations and the model problem are first introduced in Chapter 2. A detailed analysis of the modeling error for the wave equation in the frequency domain is then given in Chapter 3, which is subsequently incorporated in Chapter 4. There, an adaptive modeling technique is proposed, representing the extension of the GOALS algorithm to the elastodynamic case. The latter two chapters also include one-dimensional steady state and transient numerical applications and verifications of the new methodology. Lastly, Chapter 5 lists some concluding remarks.

It is noted that part of this work is also contained in [22].

## 2 The Elastic Wave Problem

In Section 2.1, the notations and the model problem of elastic wave propagation are introduced. Subsequently, the weak formulation of the wave equation in the frequency domain is defined in Section 2.2.

### 2.1 Model Problem and Notations

Let  $\Omega \subset \mathbb{R}^2$  be a bounded open domain with Lipschitz boundary  $\partial\Omega$ , and:

$$\partial\Omega = \overline{\Gamma_u \cup \Gamma_t}, \quad \Gamma_u \cap \Gamma_t = \emptyset,$$

where  $\Gamma_u$  denotes the part of the boundary with prescribed displacements  $\mathbf{U}$ , and  $\Gamma_t$  the part subjected to traction and damping conditions. The domain  $\Omega$  is the interior of an *elastic* solid material with a microstructure that exhibits highly oscillatory material properties (see Figure 2.1). Since we assume each of the constituents to be *linearly* elastic, the relation between the stress tensor  $\sigma$  and strain tensor  $\varepsilon$  is governed by the following linear relation:

$$\sigma = \mathbf{E}\varepsilon, \tag{2.1}$$

where  $\mathbf{E} = \mathbf{E}(\mathbf{x}) \in L^\infty(\Omega)^{N^2 \times N^2}$  denotes the fourth order elasticity tensor, which satisfies the following symmetry and ellipticity conditions:

$$\begin{aligned} E_{ijkl}(\mathbf{x}) &= E_{jikl}(\mathbf{x}) = E_{ijlk}(\mathbf{x}) = E_{klij}(\mathbf{x}), \\ \alpha_0 \xi_{ij} \xi_{ij} &\leq E_{ijkl}(\mathbf{x}) \xi_{ij} \xi_{kl} \leq \alpha_1 \xi_{ij} \xi_{ij}, \end{aligned}$$

$$\begin{aligned} 1 \leq i, j, k, l \leq 3, \quad \alpha_0, \alpha_1 \in \mathbb{R}, \quad \alpha_0 > 0, \quad \alpha_1 > 0, \\ \xi_{ij} = \xi_{ji} \in \mathbb{R}^{2 \times 2}, \quad \text{for } \mathbf{x} \in \mathbb{R}^2, \quad \text{a.e.} \end{aligned}$$

The deformations in the material are assumed to remain small, such that the strain-displacement relationships are linear:

$$\varepsilon = \frac{1}{2} (\nabla \mathbf{u} + (\nabla \mathbf{u})^T). \tag{2.2}$$

In this analysis, *stress wave* propagation is considered only. This means that both the stresses and displacements are continuous in  $\Omega$ . Now, at  $t = 0$  the initial displacement

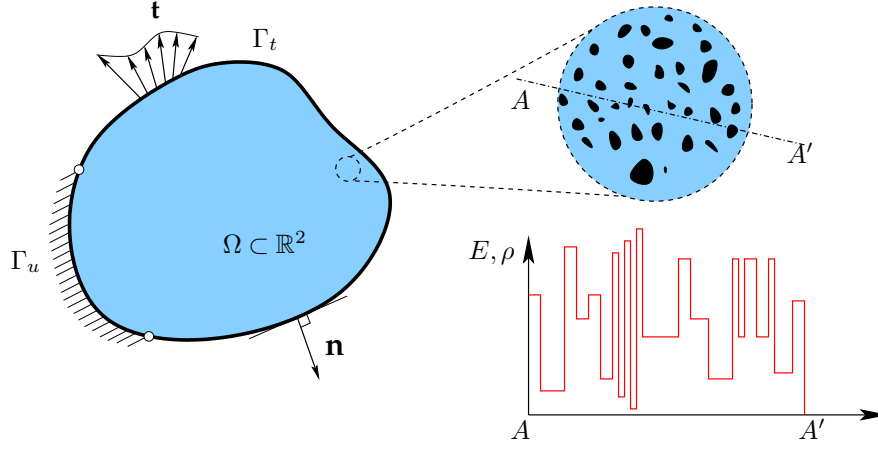


Figure 2.1: The model problem.

and velocity fields are given by  $\mathbf{U}_0 \in (H^1(\Omega))^2$  and  $\mathbf{V}_0 \in (H^1(\Omega))^2$ , respectively. The linear elastodynamic model problem can then be formulated as the following initial boundary value problem (IBVP):

For  $\mathbf{x} \in \Omega$ ,  $t \geq 0$ , find  $\mathbf{u}(\mathbf{x}, t)$  such that:

$$\rho(\mathbf{x})\ddot{\mathbf{u}}(\mathbf{x}, t) - \nabla \cdot (\mathbf{E}(\mathbf{x})\nabla\mathbf{u}(\mathbf{x}, t)) = \mathbf{f}(\mathbf{x}, t), \quad \text{in } \Omega,$$

$$\begin{aligned} \mathbf{E}\nabla\mathbf{u}(t) \cdot \mathbf{n} + \beta\dot{\mathbf{u}}(t) &= \mathbf{t}(t), & \text{on } \Gamma_t \forall t > 0, \\ \mathbf{u}(t) &= \mathbf{U}(t), & \text{on } \Gamma_u \forall t > 0, \end{aligned} \tag{2.3}$$

$$\begin{aligned} \mathbf{u}(\mathbf{x}, 0) &= \mathbf{U}_0(\mathbf{x}), & \text{in } \Omega \text{ at } t = 0, \\ \dot{\mathbf{u}}(\mathbf{x}, 0) &= \mathbf{V}_0(\mathbf{x}), & \text{in } \Omega \text{ at } t = 0, \end{aligned}$$

where the function  $\mathbf{f} \in (L^2(\Omega))^2$  represents the body forces,  $\rho \in L^\infty(\Omega)$ ,  $\rho > 0$  a.e. in  $\Omega$ , the mass density distribution of the material, and  $\beta \in L^\infty(\Gamma_t)$  the damping coefficient. Notice that the tractions  $\mathbf{t}$  are in  $L^2(\Gamma_t)$  and that  $\mathbf{U}_0$  and  $\mathbf{V}_0$  are assumed to be consistent with the boundary data.

In Chapter 4, an adaptive modeling technique is proposed that solves the wave problem in the frequency domain. Toward this purpose, we apply a classical Fourier transformation, defined as follows:

$$\hat{\mathbf{u}}(\mathbf{x}, \omega) = \mathcal{F}(\mathbf{u}(\mathbf{x}, t)) = \int_0^\infty \mathbf{u}(\mathbf{x}, t) e^{-i\omega t} dt,$$

where,  $i^2 = -1$ ,  $\omega$  represents the radial frequency, and  $\hat{\mathbf{u}}(\mathbf{x}, \omega)$ , the Fourier transform of  $\mathbf{u}(\mathbf{x}, t)$ , is a complex-valued function. The equivalent formulation of (2.3) can then

be recast as:

For every  $\omega$ , find  $\hat{\mathbf{u}}(\mathbf{x}, \omega)$  such that:

$$\begin{aligned}
 -\rho\omega^2\hat{\mathbf{u}}(\mathbf{x}, \omega) - \nabla \cdot \mathbf{E}\nabla\hat{\mathbf{u}}(\mathbf{x}, \omega) &= \hat{\mathbf{f}}(\mathbf{x}, \omega) + i\omega\rho\mathbf{U}_0(\mathbf{x}) \\
 &\quad + \rho\mathbf{V}_0(\mathbf{x}), \quad \text{in } \Omega, \\
 \mathbf{E}\nabla\hat{\mathbf{u}}(\omega) \cdot \mathbf{n} + \beta\omega i\hat{\mathbf{u}}(\omega) &= \hat{\mathbf{t}}(\omega) + \beta\mathbf{U}_0, \quad \text{on } \Gamma_t, \\
 \hat{\mathbf{u}}(\omega) &= \hat{\mathbf{U}}(\omega), \quad \text{on } \Gamma_u.
 \end{aligned}
 \tag{2.4}$$

where  $\hat{\mathbf{f}}$ ,  $\hat{\mathbf{t}}$ , and  $\hat{\mathbf{U}}$  denote the Fourier transforms of  $\mathbf{f}$ ,  $\mathbf{t}$ , and  $\mathbf{U}$ , respectively. Upon solving (2.4) for every frequency, the solution  $\mathbf{u}(\mathbf{x}, t)$  is retrieved by applying the inverse Fourier transformation:

$$\mathbf{u}(\mathbf{x}, t) = \mathcal{F}^{-1}(\hat{\mathbf{u}}(\mathbf{x}, \omega)) = \frac{1}{2\pi} \int_{-\infty}^{\infty} \hat{\mathbf{u}}(\mathbf{x}, \omega) e^{i\omega t} d\omega.$$

## 2.2 The Weak Formulation

The space of *complex*-valued test functions  $V$  is defined as follows:

$$V = \{\mathbf{v} \in (H^1(\Omega))^2 : \mathbf{v}|_{\Gamma_u} = 0\}. \tag{2.5}$$

The equivalent variational formulation of the model problem (2.4) is governed by:

For every  $\omega$  find  $\hat{\mathbf{u}} \in \{\hat{\mathbf{U}}\} + V$  such that :

$$\mathcal{B}(\hat{\mathbf{u}}, \mathbf{v}) = \mathcal{L}(\mathbf{v}), \quad \forall \mathbf{v} \in V, \tag{2.6}$$

where the sesquilinear form  $\mathcal{B}(\cdot, \cdot)$  and linear form  $\mathcal{L}(\cdot)$  are defined as follows:

$$\begin{aligned}
 \mathcal{L} : V &\longrightarrow \mathbb{C}, \quad \mathcal{B} : V \times V \longrightarrow \mathbb{C}, \\
 \mathcal{L}(\mathbf{v}) &= \int_{\Omega} \{\hat{\mathbf{f}} + i\rho\omega\mathbf{U}_0 + \rho\mathbf{V}_0\} : \bar{\mathbf{v}} d\mathbf{x} + \int_{\Gamma_t} (\hat{\mathbf{t}} + \beta\mathbf{U}_0) : \bar{\mathbf{v}} ds \\
 \mathcal{B}(\hat{\mathbf{u}}, \mathbf{v}) &= \mathcal{A}(\hat{\mathbf{u}}, \mathbf{v}) - \omega^2\mathcal{C}(\hat{\mathbf{u}}, \mathbf{v}) + i\omega\mathcal{D}(\hat{\mathbf{u}}, \mathbf{v}), \\
 \mathcal{A}(\hat{\mathbf{u}}, \mathbf{v}) &= \int_{\Omega} \mathbf{E}\nabla\hat{\mathbf{u}} : \nabla\bar{\mathbf{v}} d\mathbf{x}, \\
 \mathcal{C}(\hat{\mathbf{u}}, \mathbf{v}) &= \int_{\Omega} \rho\hat{\mathbf{u}} : \bar{\mathbf{v}} d\mathbf{x}, \\
 \mathcal{D}(\hat{\mathbf{u}}, \mathbf{v}) &= \int_{\Gamma_t} \beta\hat{\mathbf{u}} : \bar{\mathbf{v}} d\mathbf{x},
 \end{aligned}
 \tag{2.7}$$

where  $\bar{\mathbf{v}}$  denotes the complex conjugate of  $\mathbf{v}$ . The sesquilinear forms  $\mathcal{A}(\cdot, \cdot)$ ,  $\mathcal{C}(\cdot, \cdot)$ , and  $\mathcal{D}(\cdot, \cdot)$  incorporate respectively the elastic deformation, inertia, and damping conditions of the elastic body into the variational formulation.

# 3 Modeling Error Estimation

In this chapter, estimates are derived of the *modeling error* in the local average stress, induced by the employment of approximate material models for the elastic wave equation in the frequency domain. These estimates are employed in the adaptive modeling algorithm in Chapter 4 to assess the modeling error.

Section 3.1 begins with definitions of the exact and approximate variational formulations of the wave problem in the frequency domain. Subsequently, in Section 3.2, the variational problems are presented that govern the corresponding modeling errors. Elliptic representations of the error functions are derived in Section 3.3, which are first used in Section 3.4 to derive upper and lower error bounds. Secondly, *a posteriori* global and local error estimates are derived in Section 3.5. One-dimensional numerical verifications of the error estimates and bounds are shown in Section 3.6.

## 3.1 Exact and Approximate Material Models

The quantity of interest is defined in functional form and, since the wave problem is solved in the complex frequency domain, its equivalent representation is needed in this setting. Thus, if  $Q(\mathbf{u}) \in \mathbb{R}$  denotes the quantity of interest in the real-valued time domain, then its equivalent in the complex-valued frequency domain,  $\hat{Q}(\hat{\mathbf{u}})$ , is governed by the following transformations:

$$\begin{array}{ccc} W & \xrightarrow{Q} & \mathbb{R} \\ \downarrow \mathcal{F} & & \downarrow \mathcal{F} \\ V & \xrightarrow{\hat{Q}} & \mathbb{C} \end{array} \quad \hat{Q} = \mathcal{F} \circ (Q \circ \mathcal{F}^{-1}),$$

where  $W$  denotes the space of admissible displacements in time domain. In this work, the quantity of interest is the *average stress* over a small subdomain  $S \subset \Omega$  in the direction of a user-specified vector  $\nu$ :

$$\hat{Q}(\hat{\mathbf{u}}) = \frac{1}{|S|} \int_S (\mathbf{E} \nabla \hat{\mathbf{u}} \cdot \nu) \, dx. \quad (3.1)$$

Thus, the primal and dual problem [17] for the exact description of the material model, are given by:

$\begin{aligned} \mathcal{B}(\hat{\mathbf{u}}, \mathbf{v}) &= \mathcal{L}(\mathbf{v}), & \forall \mathbf{v} \in V, & \text{ primal problem} \\ \mathcal{B}(\mathbf{w}, \hat{\mathbf{p}}) &= \hat{Q}(\mathbf{w}), & \forall \mathbf{w} \in V, & \text{ dual problem} \end{aligned}$	(3.2)
------------------------------------------------------------------------------------------------------------------------------------------------------------------------------------------------------------------------------------------------------------------------------------	-------

where  $\hat{\mathbf{p}}$  denotes the influence function [17] with respect to the quantity of interest  $\hat{\mathcal{Q}}(\cdot)$ , and the functionals  $\mathcal{B}(\cdot, \cdot)$  and  $\mathcal{L}(\cdot)$  are defined in (2.7).

Now, the approximate problem is posed by using an approximate description of the material model, characterized by the functions  $\mathbf{E}_0(\mathbf{x})$  and  $\rho_0(\mathbf{x})$ . These functions represent approximations of the actual distribution of the modulus of elasticity,  $\mathbf{E}(\mathbf{x})$ , and mass density,  $\rho(\mathbf{x})$ .

The approximations  $\mathbf{E}_0(\mathbf{x})$  and  $\rho_0(\mathbf{x})$  may represent averaged or homogenized fields and are expected to be, in general, smoother than  $\mathbf{E}(\mathbf{x})$  and  $\rho(\mathbf{x})$ . In later sections, more explicit definitions of these functions are given. At this point,  $\mathbf{E}_0(\mathbf{x})$  and  $\rho_0(\mathbf{x})$  are used to define the following functionals, analogous to those in (2.7):

$$\begin{aligned}\mathcal{B}_0(\hat{\mathbf{u}}_0, \mathbf{v}) &= \mathcal{A}_0(\hat{\mathbf{u}}_0, \mathbf{v}) - \omega^2 \mathcal{C}_0(\hat{\mathbf{u}}_0, \mathbf{v}) + i\omega \mathcal{D}(\hat{\mathbf{u}}_0, \mathbf{v}), \\ \mathcal{A}_0(\hat{\mathbf{u}}_0, \mathbf{v}) &= \int_{\Omega} \mathbf{E}_0 \nabla \hat{\mathbf{u}}_0 : \nabla \bar{\mathbf{v}} dx, \\ \mathcal{C}_0(\hat{\mathbf{u}}_0, \mathbf{v}) &= \int_{\Omega} \rho_0 \hat{\mathbf{u}}_0 : \bar{\mathbf{v}} dx.\end{aligned}\tag{3.3}$$

The approximation of (3.2), can now be introduced as:

$$\begin{array}{l} \mathcal{B}_0(\hat{\mathbf{u}}_0, \mathbf{v}) = \mathcal{L}(\mathbf{v}), \quad \forall \mathbf{v} \in V, \quad \textit{primal problem} \\ \mathcal{B}_0(\mathbf{w}, \hat{\mathbf{p}}_0) = \hat{\mathcal{Q}}(\mathbf{w}), \quad \forall \mathbf{w} \in V. \quad \textit{dual problem} \end{array}\tag{3.4}$$

Note that in the definition of the functional  $\mathcal{B}_0(\cdot, \cdot)$ , the exact representation of the damping condition (the functional  $\mathcal{D}(\cdot, \cdot)$ ) is incorporated. In subsequent applications, this condition acts only on a small part of the boundary and can be easily implemented with low computational cost.

## 3.2 The Modeling Errors

The (modeling) error functions  $\hat{\mathbf{e}}_0$  and  $\hat{\mathbf{e}}_0$  for the primal and dual problem, respectively, are defined as follows:

$$\hat{\mathbf{e}}_0 = \hat{\mathbf{u}} - \hat{\mathbf{u}}_0, \quad \hat{\mathbf{e}}_0 = \hat{\mathbf{p}} - \hat{\mathbf{p}}_0.\tag{3.5}$$

Furthermore, the residual functionals characterizing the accuracy of the approximate solutions, assume the forms:

$$\begin{aligned}\mathcal{R}(\hat{\mathbf{u}}_0, \mathbf{v}) &= \mathcal{L}(\mathbf{v}) - \mathcal{B}(\hat{\mathbf{u}}_0, \mathbf{v}), \quad \mathbf{v} \in V, \\ \bar{\mathcal{R}}(\hat{\mathbf{p}}_0, \mathbf{w}) &= \mathcal{Q}(\mathbf{w}) - \mathcal{B}(\mathbf{w}, \hat{\mathbf{p}}_0), \quad \mathbf{w} \in V.\end{aligned}\tag{3.6}$$

Now, by substituting the variational approximate problems of (3.4) into the two above expressions, explicit expressions for the residual functionals in terms of the approxi-

mate solution pair  $(\hat{\mathbf{u}}_0, \hat{\mathbf{p}}_0)$  are obtained:

$$\boxed{\begin{aligned}\mathcal{R}(\hat{\mathbf{u}}_0, \mathbf{v}) &= - \int_{\Omega} \{ \mathbf{E} \mathcal{I}_0 \nabla \hat{\mathbf{u}}_0 \cdot \overline{\nabla \mathbf{v}} - \rho \omega^2 j_0 \hat{\mathbf{u}}_0 \cdot \overline{\mathbf{v}} \} \, \mathrm{d}\mathbf{x}, \\ \overline{\mathcal{R}}(\hat{\mathbf{p}}_0, \mathbf{w}) &= - \int_{\Omega} \{ \mathbf{E} \mathcal{I}_0 \nabla \mathbf{w} \cdot \overline{\nabla \hat{\mathbf{p}}_0} - \rho \omega^2 j_0 \mathbf{w} \cdot \overline{\hat{\mathbf{p}}_0} \} \, \mathrm{d}\mathbf{x}.\end{aligned}} \quad (3.7)$$

Here the deviation tensor  $\mathcal{I}_0$  and function  $j_0$  are defined in the following manner:

$$\mathcal{I}_0 = \mathbf{I} - \mathbf{E}^{-1} \mathbf{E}_0, \quad j_0(\mathbf{x}) = 1 - \frac{\rho_0(\mathbf{x})}{\rho(\mathbf{x})}. \quad (3.8)$$

Conversely, by substituting the exact formulation (3.2) into (3.6) and by employing the sesquilinear property of  $\mathcal{B}(\cdot, \cdot)$ , the following set of variational problems that govern the error functions  $\hat{\mathbf{e}}_0$  and  $\hat{\varepsilon}_0$  are derived:

$$\boxed{\begin{aligned}\mathcal{B}(\hat{\mathbf{e}}_0, \mathbf{v}) &= \mathcal{R}(\hat{\mathbf{u}}_0, \mathbf{v}), & \forall \mathbf{v} \in V, \\ \mathcal{B}(\mathbf{w}, \hat{\varepsilon}_0) &= \overline{\mathcal{R}}(\hat{\mathbf{p}}_0, \mathbf{w}), & \forall \mathbf{w} \in V.\end{aligned}} \quad (3.9)$$

By applying Theorem 1 in the work by Oden and Prudhomme [17], and noting that both  $\hat{\mathcal{Q}}(\cdot)$  and  $\mathcal{B}(\cdot, \cdot)$  are linear functionals, the following expression is obtained for the error in the quantity of interest:

$$\hat{\mathcal{Q}}(\hat{\mathbf{e}}_0) = \mathcal{R}(\hat{\mathbf{u}}_0, \hat{\mathbf{p}}_0) + \frac{1}{2} [\mathcal{R}(\hat{\mathbf{u}}_0, \hat{\varepsilon}_0) + \overline{\mathcal{R}}(\hat{\mathbf{p}}_0, \hat{\mathbf{e}}_0)].$$

Substitution of (3.9) finally yields:

$$\boxed{\hat{\mathcal{Q}}(\hat{\mathbf{e}}_0) = \underbrace{\mathcal{R}(\hat{\mathbf{u}}_0, \hat{\mathbf{p}}_0)}_{\text{computable}} + \mathcal{B}(\hat{\mathbf{e}}_0, \hat{\varepsilon}_0).} \quad (3.10)$$

In general, the first term in the RHS is a computable term, whereas the second is not. In the case of elastostatics, Oden and Vemaganti [19, 20, 26, 27] accurately estimate the unknown term by using an advantageous property of the corresponding bilinear functional in that case: it defines an inner product on the space of admissible test functions. This enables the estimation of the unknown term by global norms of the error functions, which subsequently can be estimated in terms of the computed approximate solutions. However, due to the minus sign in front of  $\mathcal{C}(\cdot, \cdot)$  and the presence of the damping term  $\mathcal{D}(\cdot, \cdot)$  in the definition of  $\mathcal{B}(\cdot, \cdot)$ , this sesquilinear form does *not* define an inner product on  $V \times V$  and the approach proposed by Oden and Vemaganti cannot directly be applied to the elastodynamic problem.

To overcome this difficulty, elliptic equivalents of the error functions are introduced in Section 3.3, which serve as an intermediate step in estimating the unknown term in (3.10).

### 3.3 Elliptic Error Representations

Elliptic representations  $\hat{\mathbf{e}}_1$  and  $\hat{\mathbf{e}}_1$  of the primal and dual error functions  $\hat{\mathbf{e}}_0$  and  $\hat{\mathbf{e}}_0$  are defined as follows:

$$\boxed{\begin{aligned}\mathcal{H}(\hat{\mathbf{e}}_1, \mathbf{v}) &= \mathcal{B}(\hat{\mathbf{e}}_0, \mathbf{v}) = \mathcal{R}(\hat{\mathbf{u}}_0, \mathbf{v}), \quad \forall \mathbf{v} \in V, \\ \mathcal{H}(\mathbf{w}, \hat{\mathbf{e}}_1) &= \mathcal{B}(\mathbf{w}, \hat{\mathbf{e}}_0) = \overline{\mathcal{R}(\hat{\mathbf{p}}_0, \mathbf{w})}, \quad \forall \mathbf{w} \in V,\end{aligned}} \quad (3.11)$$

where the sesquilinear functional  $\mathcal{H}(\cdot, \cdot)$ , is defined by:

$$\mathcal{H}: V \times V \longrightarrow \mathbb{C}, \quad (3.12)$$

$$\mathcal{H}(\mathbf{u}, \mathbf{v}) = \mathcal{A}(\mathbf{u}, \mathbf{v}) + \omega^2 \mathcal{C}(\mathbf{u}, \mathbf{v}),$$

where the functionals  $\mathcal{A}(\cdot, \cdot)$  and  $\mathcal{C}(\cdot, \cdot)$  are given in (2.7). It is observed that the above functional differs with  $\mathcal{B}(\cdot, \cdot)$  in the plus sign in front of the inertial term  $\mathcal{C}(\cdot, \cdot)$  and the elimination of the damping term  $\mathcal{D}(\cdot, \cdot)$ .

**Remark 3.3.1** *The sesquilinear form  $\mathcal{H}(\cdot, \cdot)$  is positive definite, hermitian, and consequently defines an inner product on  $V \times V$ . The norm that is implicitly defined through the inner product, is then:*

$$\|\mathbf{v}\|_{\mathcal{H}} = \sqrt{\mathcal{H}(\mathbf{v}, \mathbf{v})} = \sup_{\mathbf{w} \in V} \frac{|\mathcal{H}(\mathbf{v}, \mathbf{w})|}{\|\mathbf{w}\|_{\mathcal{H}}}. \quad (3.13)$$

By recalling expression (3.10), the error can be rewritten in terms of the elliptic representations by applying the variational formulation (3.11)<sup>2</sup>, which yields:

$$\hat{\mathcal{Q}}(\hat{\mathbf{e}}_0) = \mathcal{R}(\hat{\mathbf{u}}_0, \hat{\mathbf{p}}_0) + \mathcal{H}(\hat{\mathbf{e}}_0, \hat{\mathbf{e}}_1).$$

By combining (2.7) and (3.12), the last term in the RHS can be expanded as follows:

$$\mathcal{H}(\hat{\mathbf{e}}_0, \hat{\mathbf{e}}_1) = \mathcal{B}(\hat{\mathbf{e}}_0, \hat{\mathbf{e}}_1) + 2\omega^2 \mathcal{C}(\hat{\mathbf{e}}_0, \hat{\mathbf{e}}_1) - i\omega \mathcal{D}(\hat{\mathbf{e}}_0, \hat{\mathbf{e}}_1).$$

Thus,

$$\hat{\mathcal{Q}}(\hat{\mathbf{e}}_0) = \mathcal{R}(\hat{\mathbf{u}}_0, \hat{\mathbf{p}}_0) + \mathcal{B}(\hat{\mathbf{e}}_0, \hat{\mathbf{e}}_1) + 2\omega^2 \mathcal{C}(\hat{\mathbf{e}}_0, \hat{\mathbf{e}}_1) - i\omega \mathcal{D}(\hat{\mathbf{e}}_0, \hat{\mathbf{e}}_1).$$

Substitution of (3.11)<sup>1</sup> then gives:

$$\hat{\mathcal{Q}}(\hat{\mathbf{e}}_0) = \mathcal{R}(\hat{\mathbf{u}}_0, \hat{\mathbf{p}}_0) + \mathcal{H}(\hat{\mathbf{e}}_1, \hat{\mathbf{e}}_1) + 2\omega^2 \mathcal{C}(\hat{\mathbf{e}}_0, \hat{\mathbf{e}}_1) - i\omega \mathcal{D}(\hat{\mathbf{e}}_0, \hat{\mathbf{e}}_1). \quad (3.14)$$

To estimate the error  $\hat{\mathcal{Q}}(\hat{\mathbf{e}}_0)$ , as given in (3.14), the following intermediate error estimator  $\gamma^*$  is proposed:

$$\boxed{\gamma^* = \mathcal{R}(\hat{\mathbf{u}}_0, \hat{\mathbf{p}}_0) + \mathcal{H}(\hat{\mathbf{e}}_1, \hat{\mathbf{e}}_1),} \quad (3.15)$$

where the terms in (3.14) have been neglected that involve  $\hat{\mathbf{e}}_0$ .

**Remark 3.3.2** *At this stage, no theoretical proof of the accuracy of  $\gamma^*$  has been given, but numerical verifications in Section 3.6 show that this estimator provides a remarkably accurate estimate of the modeling error in the local average stress, even for high frequencies and for a wide range of material properties.*

In practical applications, of course one does not want to use  $\gamma^*$  as an estimate of the modeling error, as it involves the solution of  $(\hat{\mathbf{e}}_1, \hat{\varepsilon}_1)$ . These functions are governed by the variational problems in (3.11) and involve the exact description of the material model. Here, the estimator  $\gamma^*$  is introduced as an intermediate step toward deriving computable estimators. Numerical experiments show that  $\gamma^*$  represents an accurate error estimate. Thus, accurately estimating  $\gamma^*$ , indirectly leads to an accurate estimate of the modeling error itself.

The inner product property of  $\mathcal{H}(\cdot, \cdot)$  can now be used (see Remark 3.3.1). According to the *Polarization Formula* [16], the last term in (3.15) can be expanded as follows:

$$\mathcal{H}(\hat{\mathbf{e}}_1, \hat{\varepsilon}_1) = \frac{1}{4} \|\hat{\mathbf{e}}_1 + \hat{\varepsilon}_1\|_{\mathcal{H}}^2 - \frac{1}{4} \|\hat{\mathbf{e}}_1 - \hat{\varepsilon}_1\|_{\mathcal{H}}^2 + \frac{i}{4} \|\hat{\mathbf{e}}_1 + i\hat{\varepsilon}_1\|_{\mathcal{H}}^2 - \frac{i}{4} \|\hat{\mathbf{e}}_1 - i\hat{\varepsilon}_1\|_{\mathcal{H}}^2. \quad (3.16)$$

Hence, (3.15) can be rewritten as:

$$\begin{aligned} \gamma^* = & \mathcal{R}(\hat{\mathbf{u}}_0, \hat{\mathbf{p}}_0) + \frac{1}{4} \|\hat{\mathbf{e}}_1 + \hat{\varepsilon}_1\|_{\mathcal{H}}^2 - \frac{1}{4} \|\hat{\mathbf{e}}_1 - \hat{\varepsilon}_1\|_{\mathcal{H}}^2 \\ & + \frac{i}{4} \|\hat{\mathbf{e}}_1 + i\hat{\varepsilon}_1\|_{\mathcal{H}}^2 - \frac{i}{4} \|\hat{\mathbf{e}}_1 - i\hat{\varepsilon}_1\|_{\mathcal{H}}^2. \end{aligned} \quad (3.17)$$

Now, since the first part in the RHS is computable, estimates and bounds on  $\gamma^*$  can be derived by estimating and bounding the remaining terms involving the norms of  $\hat{\mathbf{e}}_1$  and  $\hat{\varepsilon}_1$ . In the following two sections, a selection of bounds and estimates of these norms is derived and used to propose estimators and bounds of  $\gamma^*$  and, therefore, indirectly of the modeling error in the average stress  $\hat{\mathcal{Q}}(\hat{\mathbf{e}}_0)$  itself.

### 3.4 Computable Upper and Lower Error Bounds

In this section, upper and lower bounds on the error estimator  $\gamma^*$  are derived. As mentioned in the previous section, it is assumed that these bounds hold for the modeling error itself as well.

**Lemma 3.4.1** *Let  $(\hat{\mathbf{u}}_0, \hat{\mathbf{p}}_0)$  and  $(\hat{\mathbf{e}}_1, \hat{\varepsilon}_1)$  be solutions to (3.4) and (3.11), respectively, and let the deviation tensor and function  $\mathcal{I}_0$  and  $j_0$  of (3.8) be piecewise continuous functions in  $\Omega$ . Then the following computable upper and lower bounds hold for the norms in (3.17):*

$$\begin{aligned} \eta_{low}^+ & \leq \|\hat{\mathbf{e}}_1 + \hat{\varepsilon}_1\|_{\mathcal{H}} \leq \eta_{upp}^+, \\ \eta_{low}^- & \leq \|\hat{\mathbf{e}}_1 - \hat{\varepsilon}_1\|_{\mathcal{H}} \leq \eta_{upp}^-, \\ \eta_{low,i}^+ & \leq \|\hat{\mathbf{e}}_1 + i\hat{\varepsilon}_1\|_{\mathcal{H}} \leq \eta_{upp,i}^+, \\ \eta_{low,i}^- & \leq \|\hat{\mathbf{e}}_1 - i\hat{\varepsilon}_1\|_{\mathcal{H}} \leq \eta_{upp,i}^-, \end{aligned} \quad (3.18)$$

where:

$$\begin{aligned}
\eta_{upp}^\pm &= \sqrt{\|\mathcal{I}_0(\hat{\mathbf{u}}_0 \pm \hat{\mathbf{p}}_0)\|_{\mathcal{A}}^2 + \omega^2 \|j_0(\hat{\mathbf{u}}_0 \pm \hat{\mathbf{p}}_0)\|_{\mathcal{C}}^2}, \\
\eta_{upp,i}^\pm &= \sqrt{\|\mathcal{I}_0(\hat{\mathbf{u}}_0 \pm i\hat{\mathbf{p}}_0)\|_{\mathcal{A}}^2 + \omega^2 \|j_0(\hat{\mathbf{u}}_0 \pm i\hat{\mathbf{p}}_0)\|_{\mathcal{C}}^2}, \\
\eta_{low}^\pm &= \frac{|\mathcal{R}(\hat{\mathbf{u}}_0 \pm \hat{\mathbf{p}}_0, \hat{\mathbf{u}}_0 + \theta^\pm \hat{\mathbf{p}}_0)|}{\|\hat{\mathbf{u}}_0 + \theta^\pm \hat{\mathbf{p}}_0\|_{\mathcal{H}}}, \\
\eta_{low,i}^\pm &= \frac{|\mathcal{R}(\hat{\mathbf{u}}_0 \pm i\hat{\mathbf{p}}_0, \hat{\mathbf{u}}_0 + \theta_i^\pm \hat{\mathbf{p}}_0)|}{\|\hat{\mathbf{u}}_0 + \theta_i^\pm \hat{\mathbf{p}}_0\|_{\mathcal{H}}}, \\
\|\mathbf{v}\|_{\mathcal{A}}^2 &= \mathcal{A}(\mathbf{v}, \mathbf{v}), \quad \|\mathbf{v}\|_{\mathcal{C}}^2 = \mathcal{C}(\mathbf{v}, \mathbf{v}),
\end{aligned} \tag{3.19}$$

where the sesquilinear forms  $\mathcal{A}(\cdot, \cdot)$  and  $\mathcal{C}(\cdot, \cdot)$  are defined in (2.7), the residual functional  $\mathcal{R}(\cdot, \cdot)$  is defined in (3.7)<sup>1</sup>, and where  $\theta^\pm$  and  $\theta_i^\pm \in \mathbb{C}$ .

*Proof:* Only the proof for the bounds on the first norm in (3.18) are presented. The proofs for the other norms follow analogously. Applying the definition of the norm  $\|\cdot\|_{\mathcal{H}}$  as given in (3.13), gives:

$$\|\hat{\mathbf{e}}_1 + \hat{\varepsilon}_1\|_{\mathcal{H}} = \sup_{\mathbf{w} \in V} \frac{|\mathcal{H}(\hat{\mathbf{e}}_1 + \hat{\varepsilon}_1, \mathbf{w})|}{\|\mathbf{w}\|_{\mathcal{H}}}.$$

By recalling Remark 3.3.1 that  $\mathcal{H}(\cdot, \cdot)$  is sesquilinear and hermitian, this expression is rewritten as:

$$\|\hat{\mathbf{e}}_1 + \hat{\varepsilon}_1\|_{\mathcal{H}} = \sup_{\mathbf{w} \in V} \frac{|\mathcal{H}(\hat{\mathbf{e}}_1, \mathbf{w}) + \overline{\mathcal{H}(\mathbf{w}, \hat{\varepsilon}_1)}|}{\|\mathbf{w}\|_{\mathcal{H}}},$$

and, subsequently, the variational problems given in (3.11) are introduced, which yields:

$$\|\hat{\mathbf{e}}_1 + \hat{\varepsilon}_1\|_{\mathcal{H}} = \sup_{\mathbf{w} \in V} \frac{|\mathcal{R}(\hat{\mathbf{u}}_0, \mathbf{w}) + \overline{\mathcal{R}(\hat{\mathbf{p}}_0, \mathbf{w})}|}{\|\mathbf{w}\|_{\mathcal{H}}}.$$

If the explicit expressions for the primal and dual residual functional in (3.7) are compared, it is observed that  $\overline{\mathcal{R}(\hat{\mathbf{p}}_0, \mathbf{w})} = \mathcal{R}(\hat{\mathbf{p}}_0, \mathbf{w})$ . Hence,

$$\|\hat{\mathbf{e}}_1 + \hat{\varepsilon}_1\|_{\mathcal{H}} = \sup_{\mathbf{w} \in V} \frac{|\mathcal{R}(\hat{\mathbf{u}}_0 + \hat{\mathbf{p}}_0, \mathbf{w})|}{\|\mathbf{w}\|_{\mathcal{H}}}. \tag{3.20}$$

The lower bound  $\eta_{low}^+$  now follows by applying the definition of the supremum and choosing  $\mathbf{w} = \hat{\mathbf{u}}_0 + \theta^+ \hat{\mathbf{p}}_0$ , where  $\theta^+ \in \mathbb{C}$  is arbitrary. Thus,

$$\|\hat{\mathbf{e}}_1 + \hat{\varepsilon}_1\|_{\mathcal{H}} \geq \frac{|\mathcal{R}(\hat{\mathbf{u}}_0 + \hat{\mathbf{p}}_0, \hat{\mathbf{u}}_0 + \theta^+ \hat{\mathbf{p}}_0)|}{\|\hat{\mathbf{u}}_0 + \theta^+ \hat{\mathbf{p}}_0\|_{\mathcal{H}}}, \quad \forall \theta^+ \in \mathbb{C}.$$

To prove the upper bound, (3.20) is rewritten by using (3.7)<sup>1</sup> and (2.7), and by recalling that  $\mathcal{I}_0$  and  $j_0$  are piecewise continuous, which gives:

$$\|\hat{\mathbf{e}}_1 + \hat{\varepsilon}_1\|_{\mathcal{H}} = \sup_{\mathbf{w} \in \mathcal{V}} \frac{|\mathcal{A}(\mathcal{I}_0(\hat{\mathbf{u}}_0 + \hat{\mathbf{p}}_0), \mathbf{w}) - \omega^2 \mathcal{C}(j_0(\hat{\mathbf{u}}_0 + \hat{\mathbf{p}}_0), \mathbf{w})|}{\|\mathbf{w}\|_{\mathcal{H}}}. \quad (3.21)$$

Applying the triangle and Schwarz inequalities to the nominator of (3.21), gives:

$$\begin{aligned} & |\mathcal{A}(\mathcal{I}_0(\hat{\mathbf{u}}_0 + \hat{\mathbf{p}}_0), \mathbf{w})| + \omega^2 |\mathcal{C}(j_0(\hat{\mathbf{u}}_0 + \hat{\mathbf{p}}_0), \mathbf{w})| \leq \\ & \sqrt{\mathcal{A}(\mathcal{I}_0(\hat{\mathbf{u}}_0 + \hat{\mathbf{p}}_0), \mathcal{I}_0(\hat{\mathbf{u}}_0 + \hat{\mathbf{p}}_0))} \sqrt{\mathcal{A}(\mathbf{w}, \mathbf{w})} \\ & \quad + \omega^2 \sqrt{\mathcal{C}(j_0(\hat{\mathbf{u}}_0 + \hat{\mathbf{p}}_0), j_0(\hat{\mathbf{u}}_0 + \hat{\mathbf{p}}_0))} \sqrt{\mathcal{C}(\mathbf{w}, \mathbf{w})} \\ & \leq \sqrt{\mathcal{A}(\mathcal{I}_0(\hat{\mathbf{u}}_0 + \hat{\mathbf{p}}_0), \mathcal{I}_0(\hat{\mathbf{u}}_0 + \hat{\mathbf{p}}_0)) + \omega^2 \mathcal{C}(j_0(\hat{\mathbf{u}}_0 + \hat{\mathbf{p}}_0), j_0(\hat{\mathbf{u}}_0 + \hat{\mathbf{p}}_0))} \\ & \quad \times \sqrt{\mathcal{A}(\mathbf{w}, \mathbf{w}) + \omega^2 \mathcal{C}(\mathbf{w}, \mathbf{w})} \\ & = \sqrt{\|\mathcal{I}_0(\hat{\mathbf{u}}_0 \pm \hat{\mathbf{p}}_0)\|_{\mathcal{A}}^2 + \omega^2 \|j_0(\hat{\mathbf{u}}_0 \pm \hat{\mathbf{p}}_0)\|_{\mathcal{C}}^2} \|\mathbf{w}\|_{\mathcal{H}}. \end{aligned}$$

Finally, the upper bound  $\eta_{\text{upp}}^+$  is obtained by substituting this expression into (3.21). ■

To obtain near optimal values of the complex numbers  $\theta^\pm$  and  $\theta_i^\pm$ , a procedure summarized in Appendix A is employed. If the upper and lower bounds of this lemma are introduced to (3.17), upper and lower bounds on the real and imaginary parts of  $\gamma^*$  follow automatically.

**Corollary 3.4.1** *Given the bounds  $\eta_{\text{upp}(i)}^\pm$  and  $\eta_{\text{low}(i)}^\pm$ , the real and imaginary parts of  $\gamma^*$  are bounded as follows:*

$$\begin{aligned} \eta_{\text{low}, \text{real}} & \leq \mathcal{R}e\{\gamma^*\} \leq \eta_{\text{upp}, \text{real}}, \\ \eta_{\text{low}, \text{imag}} & \leq \mathcal{I}m\{\gamma^*\} \leq \eta_{\text{upp}, \text{imag}}, \end{aligned} \quad (3.22)$$

where:

$$\begin{aligned} \eta_{\text{low}, \text{real}} & = \mathcal{R}e\{\mathcal{R}(\hat{\mathbf{u}}_0, \hat{\mathbf{p}}_0)\} + \frac{1}{4}\eta_{\text{low}}^+{}^2 - \frac{1}{4}\eta_{\text{upp}}^-{}^2, \\ \eta_{\text{upp}, \text{real}} & = \mathcal{R}e\{\mathcal{R}(\hat{\mathbf{u}}_0, \hat{\mathbf{p}}_0)\} + \frac{1}{4}\eta_{\text{upp}}^+{}^2 - \frac{1}{4}\eta_{\text{low}}^-{}^2, \\ \eta_{\text{low}, \text{imag}} & = \mathcal{I}m\{\mathcal{R}(\hat{\mathbf{u}}_0, \hat{\mathbf{p}}_0)\} + \frac{1}{4}\eta_{\text{low}, i}^+{}^2 - \frac{1}{4}\eta_{\text{upp}, i}^-{}^2, \\ \eta_{\text{upp}, \text{imag}} & = \mathcal{I}m\{\mathcal{R}(\hat{\mathbf{u}}_0, \hat{\mathbf{p}}_0)\} + \frac{1}{4}\eta_{\text{upp}, i}^+{}^2 - \frac{1}{4}\eta_{\text{low}, i}^-{}^2. \end{aligned} \quad (3.23)$$

*Proof:* Only the upper bound on  $\mathcal{R}e\{\gamma^*\}$  is proved, as the proofs for the other bounds follow analogously. Taking the real part of (3.17), gives:

$$\mathcal{R}e\{\gamma^*\} = \mathcal{R}e\{\mathcal{R}(\hat{\mathbf{u}}_0, \hat{\mathbf{p}}_0)\} + \frac{1}{4}\|\hat{\mathbf{e}}_1 + \hat{\varepsilon}_1\|_{\mathcal{H}}^2 - \frac{1}{4}\|\hat{\mathbf{e}}_1 - \hat{\varepsilon}_1\|_{\mathcal{H}}^2.$$

By applying the inequality of (3.18)<sup>1</sup>, one obtains:

$$\mathcal{Re}\{\gamma^*\} \leq \mathcal{Re}\{\mathcal{R}(\hat{\mathbf{u}}_0, \hat{\mathbf{p}}_0)\} + \frac{1}{4}\eta_{\text{upp}}^{+2} - \frac{1}{4}\|\hat{\mathbf{e}}_1 - \hat{\varepsilon}_1\|_{\mathcal{H}}^2.$$

Finally, by substituting (3.18)<sup>2</sup>, the assertion is established:

$$\mathcal{Re}\{\gamma^*\} \leq \mathcal{Re}\{\mathcal{R}(\hat{\mathbf{u}}_0, \hat{\mathbf{p}}_0)\} + \frac{1}{4}\eta_{\text{upp}}^{+2} - \frac{1}{4}\eta_{\text{low}}^{-2}.$$

■

## 3.5 Modeling Error Estimates

In this section, two types of *a posteriori* estimates of the modeling error are derived. Section 3.5.1 introduces estimates of the modeling in the *local* average stress in a sub-domain  $S$  of  $\Omega$ , whereas Section 3.5.2 presents *global* error estimates in the norm  $\|\cdot\|_{\mathcal{H}}$ .

### 3.5.1 Local Error Estimates

Numerical experiments confirm that the bounds on the modeling error of (3.22) indeed are bounds to both  $\gamma^*$  and  $\hat{Q}(\hat{\mathbf{e}}_0)$ . However, for the elastostatic case [19], these types of bounds are a factor of 100 higher and lower than the error. On the basis of extensive numerical experiments it has been observed that for the elastodynamic case, the bounds of (3.22) are a factor 1000 or 10,000 higher and lower than the error.

These bounds are distributed roughly equally around the error. Accordingly, the first estimator  $\gamma_{\text{avg}}$  that is proposed, uses the averages of these bounds. Thus, given the bounds  $\eta_{\text{low,real}}$ ,  $\eta_{\text{low,imag}}$ ,  $\eta_{\text{upp,real}}$ , and  $\eta_{\text{upp,imag}}$  of (3.22) and (3.23), an estimator  $\gamma_{\text{avg}}$  of  $\gamma^*$  is introduced as:

$$\gamma_{\text{avg}} = \frac{1}{2} \left\{ (\eta_{\text{upp,real}} + \eta_{\text{low,real}}) + i(\eta_{\text{upp,imag}} + \eta_{\text{low,imag}}) \right\} \quad (3.24)$$

Numerical tests (see Section 3.6), also suggest that the bounds  $\eta_{\text{upp}}^{\pm}$ ,  $\eta_{\text{upp},i'}^{\pm}$  and  $\eta_{\text{low}}^{\pm}$ ,  $\eta_{\text{low},i}^{\pm}$  have good effectivity indices with respect to the norms  $\|\hat{\mathbf{e}}_1 \pm \hat{\varepsilon}_1\|_{\mathcal{H}}$  and  $\|\hat{\mathbf{e}}_1 \pm i\hat{\varepsilon}_1\|_{\mathcal{H}}$  they bound. The upper bounds  $\eta_{\text{upp}}^{\pm}$  and  $\eta_{\text{upp},i}^{\pm}$  exhibit very good accuracy within 3% for a wide range of problem configurations. Hence, given the bounds  $\eta_{\text{upp}}^{\pm}$ ,  $\eta_{\text{upp},i}^{\pm}$  and  $\eta_{\text{low}}^{\pm}$ ,  $\eta_{\text{low},i}^{\pm}$  of (3.18) and (3.19), estimators  $\gamma_{\text{upp}}$  and  $\gamma_{\text{low}}$  of  $\gamma^*$  are defined such that:

$$\begin{aligned} \gamma_{\text{upp}} &= \mathcal{R}(\hat{\mathbf{u}}_0, \hat{\mathbf{p}}_0) + \frac{1}{4} \left\{ (\eta_{\text{upp}}^{+2} - \eta_{\text{upp}}^{-2}) + i(\eta_{\text{upp},i}^{+2} - \eta_{\text{upp},i}^{-2}) \right\}, \\ \gamma_{\text{low}} &= \mathcal{R}(\hat{\mathbf{u}}_0, \hat{\mathbf{p}}_0) + \frac{1}{4} \left\{ (\eta_{\text{low}}^{+2} - \eta_{\text{low}}^{-2}) + i(\eta_{\text{low},i}^{+2} - \eta_{\text{low},i}^{-2}) \right\}, \end{aligned} \quad (3.25)$$

where  $\gamma_{\text{upp}}$  is derived by estimating the norms  $\|\hat{\mathbf{e}}_1 \pm \hat{\varepsilon}_1\|_{\mathcal{H}}$  and  $\|\hat{\mathbf{e}}_1 \pm i\hat{\varepsilon}_1\|_{\mathcal{H}}$  in the RHS of (3.17) by their corresponding upper bounds  $\eta_{\text{upp}}^{\pm}$ ,  $\eta_{\text{upp},i'}^{\pm}$  and where  $\gamma_{\text{low}}$  is derived similarly by using the lower bounds  $\eta_{\text{low}}^{\pm}$ ,  $\eta_{\text{low},i}^{\pm}$ .

Numerical experiments in Section 3.6 show that the estimators  $\gamma_{\text{avg}}$  and  $\gamma_{\text{low}}$  exhibit poor effectivity indices of a factor 10, for low frequencies, and a factor 100, for high frequencies. For low frequencies, the estimator  $\gamma_{\text{upp}}$  gives the correct order of the magnitude of the error. However, for the higher frequency ranges, the effectivity index of  $\gamma_{\text{upp}}$  also loses accuracy.

Toward deriving an alternative estimator, the variational formulations in (3.11) governing the functions  $\hat{\mathbf{e}}_1$  and  $\hat{\varepsilon}_1$  are recalled, and the sesquilinear and hermitian properties of  $\mathcal{H}(\cdot, \cdot)$  are employed, which yields:

$$\mathcal{H}(\hat{\mathbf{e}}_1 + \hat{\varepsilon}_1, \mathbf{v}) = \mathcal{R}(\hat{\mathbf{u}}_0, \mathbf{v}) + \overline{\mathcal{R}(\hat{\mathbf{p}}_0, \mathbf{v})}, \quad \forall \mathbf{v} \in V.$$

By comparing the explicit expressions for the primal and dual residual functional in (3.7), one observes that  $\overline{\mathcal{R}(\hat{\mathbf{p}}_0, \mathbf{v})} = \mathcal{R}(\hat{\mathbf{p}}_0, \mathbf{v})$ . Hence,

$$\mathcal{H}(\hat{\mathbf{e}}_1 + \hat{\varepsilon}_1, \mathbf{v}) = \mathcal{R}(\hat{\mathbf{u}}_0 + \hat{\mathbf{p}}_0, \mathbf{v}), \quad \forall \mathbf{v} \in V.$$

Applying the definition of the norm  $\|\cdot\|_{\mathcal{H}}$ , as given in (3.13), leads to:

$$\begin{aligned} \|\hat{\mathbf{e}}_1 + \hat{\varepsilon}_1\|_{\mathcal{H}}^2 &= \mathcal{R}(\hat{\mathbf{u}}_0 + \hat{\mathbf{p}}_0, \hat{\mathbf{e}}_1 + \hat{\varepsilon}_1) \\ &= -\mathcal{A}(\mathcal{I}_0(\hat{\mathbf{u}}_0 + \hat{\mathbf{p}}_0), \hat{\mathbf{e}}_1 + \hat{\varepsilon}_1) + \omega^2 \mathcal{C}(j_0(\hat{\mathbf{u}}_0 + \hat{\mathbf{p}}_0), \hat{\mathbf{e}}_1 + \hat{\varepsilon}_1), \end{aligned} \quad (3.26)$$

To simplify notations, in the following treatment,  $(\hat{\mathbf{u}}_0 + \hat{\mathbf{p}}_0)$  and  $(\hat{\mathbf{e}}_1 + \hat{\varepsilon}_1)$  are respectively denoted as  $\tilde{\mathbf{U}}$  and  $\tilde{\varepsilon}$ . From (3.26) one can establish the following upper and lower bounds to  $\|\tilde{\varepsilon}\|_{\mathcal{H}}$ :

$$|\mathcal{A}(\mathcal{I}_0\tilde{\mathbf{U}}, \tilde{\varepsilon})| - |\mathcal{C}(j_0\tilde{\mathbf{U}}, \tilde{\varepsilon})| \leq \|\tilde{\varepsilon}\|_{\mathcal{H}}^2 \leq |\mathcal{A}(\mathcal{I}_0\tilde{\mathbf{U}}, \tilde{\varepsilon})| + |\mathcal{C}(j_0\tilde{\mathbf{U}}, \tilde{\varepsilon})|. \quad (3.27)$$

All numerical experiments in this study have shown that  $\mathcal{A}(\mathcal{I}_0\tilde{\mathbf{U}}, \tilde{\varepsilon}) \leq 0$  and  $\mathcal{C}(j_0\tilde{\mathbf{U}}, \tilde{\varepsilon}) \geq 0$ . This suggests that the upper bound in the above expression generally equates the norm  $\|\tilde{\varepsilon}\|_{\mathcal{H}}$ . In addition, it is observed that the lower bound (see Table 3.2 in Section 3.6.1) provides an accurate estimator of  $\|\tilde{\varepsilon}\|_{\mathcal{H}}$  with effectivity indices very close to 1. Hence, by accurately estimating  $|\mathcal{A}(\mathcal{I}_0\tilde{\mathbf{U}}, \tilde{\varepsilon})|$  and  $|\mathcal{C}(j_0\tilde{\mathbf{U}}, \tilde{\varepsilon})|$ , and by replacing these terms in the bounds of (3.27), an accurate estimate of  $\|\tilde{\varepsilon}\|_{\mathcal{H}}$  is obtained. Toward this purpose, the upper bound  $\eta_{\text{upp}}^+$ , as defined in (3.19), is recalled:

$$\|\tilde{\varepsilon}\|_{\mathcal{H}}^2 \leq \eta_{\text{upp}}^+{}^2 = \|\mathcal{I}_0\tilde{\mathbf{U}}\|_{\mathcal{A}}^2 + \|j_0\tilde{\mathbf{U}}\|_{\mathcal{C}}^2.$$

As mentioned previously,  $\eta_{\text{upp}}^+$  provides high accuracies (within 3%) for estimating  $\|\tilde{\varepsilon}\|_{\mathcal{H}}$ . Comparison of  $\eta_{\text{upp}}^+$  with the upper bound in (3.27), indicates that  $\eta_{\text{upp}}^+$  represents an estimate of the upper bound in (3.27) by assuming that  $|\mathcal{A}(\mathcal{I}_0\tilde{\mathbf{U}}, \tilde{\varepsilon})| \approx \|\mathcal{I}_0\tilde{\mathbf{U}}\|_{\mathcal{A}}^2$  and  $|\mathcal{C}(j_0\tilde{\mathbf{U}}, \tilde{\varepsilon})| \approx \|j_0\tilde{\mathbf{U}}\|_{\mathcal{C}}^2$ . A similar approach is proposed to estimate the lower bound in (3.27) by introducing  $\xi^+$ , defined as follows:

$$\xi^+ = \left| \|\mathcal{I}_0\tilde{\mathbf{U}}\|_{\mathcal{A}}^2 - \|j_0\tilde{\mathbf{U}}\|_{\mathcal{C}}^2 \right|.$$

Numerical experiments in Section 3.6 reveal that  $\xi^+$  exhibits remarkable accuracy within 1% or less for estimating  $\|\hat{\mathbf{e}}_1 + \hat{\varepsilon}_1\|_{\mathcal{H}}$  for a large range of frequencies and problem configurations.

A similar treatment for estimating the norms  $\|\hat{\mathbf{e}}_1 - \hat{\varepsilon}_1\|_{\mathcal{H}}$  and  $\|\hat{\mathbf{e}}_1 \pm i\hat{\varepsilon}_1\|_{\mathcal{H}}$  can be applied, leading to the following estimates of these norms:

$$\begin{aligned}\xi^{\pm} &= \sqrt{\left| \|\mathcal{I}_0(\hat{\mathbf{u}}_0 \pm \hat{\mathbf{p}}_0)\|_{\mathcal{A}}^2 - \|j_0(\hat{\mathbf{u}}_0 \pm \hat{\mathbf{p}}_0)\|_{\mathcal{C}}^2 \right|}, \\ \xi_i^{\pm} &= \sqrt{\left| \|\mathcal{I}_0(\hat{\mathbf{u}}_0 \pm i\hat{\mathbf{p}}_0)\|_{\mathcal{A}}^2 - \|j_0(\hat{\mathbf{u}}_0 \pm i\hat{\mathbf{p}}_0)\|_{\mathcal{C}}^2 \right|}.\end{aligned}\tag{3.28}$$

Subsequently, these estimates are used to propose an estimator  $\gamma_{\text{est}}$  of  $\gamma^*$ , defined as follows:

$$\gamma_{\text{est}} = \mathcal{R}(\hat{\mathbf{u}}_0, \hat{\mathbf{p}}_0) + \frac{1}{4} \left\{ (\xi^{+2} - \xi^{-2}) + i(\xi_i^{+2} - \xi_i^{-2}) \right\}.\tag{3.29}$$

This estimator is obtained by replacing the terms  $\|\hat{\mathbf{e}}_1 \pm \hat{\varepsilon}_1\|_{\mathcal{H}}$  and  $\|\hat{\mathbf{e}}_1 \pm i\hat{\varepsilon}_1\|_{\mathcal{H}}$  in (3.17) by their respective estimators, defined in (3.28).

In Section 3.6, numerical verifications reveal that this estimator exhibits high accuracy for estimating  $\gamma^*$  and the modeling error itself. Improving the accuracy of the estimates of the norms  $\|\cdot\|_{\mathcal{H}}$  in (3.17), by using the estimates  $\xi^{\pm}$  and  $\xi_i^{\pm}$  instead of  $\eta_{\text{upp}}^{\pm}$  and  $\eta_{\text{upp},i}^{\pm}$  improves the overall accuracy of estimating  $\gamma^*$  significantly. It is noteworthy that for high frequency, the estimate  $\gamma_{\text{est}}$  still maintains good accuracy.

**Remark 3.5.1** Estimating  $|\mathcal{A}(\mathcal{I}_0\tilde{\mathbf{U}}, \tilde{\varepsilon})|$  and  $|\mathcal{C}(\mathcal{I}_0\tilde{\mathbf{U}}, \tilde{\varepsilon})|$  in (3.27) with  $\|\mathcal{I}_0\tilde{\mathbf{U}}\|_{\mathcal{A}}^2$  and  $\|j_0\tilde{\mathbf{U}}\|_{\mathcal{C}}^2$  provides an estimate of the lower bound in (3.27), but the estimate itself is not a guaranteed lower bound. Numerical experiments in Section 3.6 show indeed that the estimates  $\xi^{\pm}$  and  $\xi_i^{\pm}$  are generally less than  $\|\hat{\mathbf{e}}_1 \pm \hat{\varepsilon}_1\|_{\mathcal{H}}$  and  $\|\hat{\mathbf{e}}_1 \pm i\hat{\varepsilon}_1\|_{\mathcal{H}}$ , but in some cases they can be slightly larger (e.g. see Tables 3.7 and 3.17).

**Remark 3.5.2** It is assumed that the higher accuracy of  $\xi^{\pm}$  and  $\xi_i^{\pm}$  compared to  $\eta_{\text{upp}}^{\pm}$  and  $\eta_{\text{upp},i}^{\pm}$  can be explained by a cancellation of errors in estimates  $\|\mathcal{I}_0\tilde{\mathbf{U}}\|_{\mathcal{A}}^2$  and  $\|j_0\tilde{\mathbf{U}}\|_{\mathcal{C}}^2$  when these are subtracted to estimate the lower bound in (3.27).

### 3.5.2 Global Error Estimates

**Lemma 3.5.1** Let  $(\hat{\mathbf{e}}_1, \hat{\varepsilon}_1)$  denote the elliptic representation defined in (3.11) and let  $(\hat{\mathbf{u}}_0, \hat{\mathbf{p}}_0)$  denote the solutions of the coarse model (3.4). Then:

$$\begin{aligned}\zeta_{\text{low}} &\leq \|\hat{\mathbf{e}}_1\|_{\mathcal{H}} \leq \zeta_{\text{upp}}, \\ \bar{\zeta}_{\text{low}} &\leq \|\hat{\varepsilon}_1\|_{\mathcal{H}} \leq \bar{\zeta}_{\text{upp}},\end{aligned}$$

where:

$$\begin{aligned}\zeta_{low} &= \frac{|\mathcal{R}(\hat{\mathbf{u}}_0, \hat{\mathbf{u}}_0)|}{\|\hat{\mathbf{u}}_0\|_{\mathcal{H}}}, \\ \bar{\zeta}_{low} &= \frac{|\overline{\mathcal{R}}(\hat{\mathbf{p}}_0, \hat{\mathbf{p}}_0)|}{\|\hat{\mathbf{p}}_0\|_{\mathcal{H}}}, \\ \zeta_{upp} &= \sqrt{\int_{\Omega} \{\mathbf{E}\mathcal{I}_0 \nabla \hat{\mathbf{u}}_0 \cdot \overline{\mathcal{I}_0 \nabla \hat{\mathbf{u}}_0} + \rho\omega^2 j_0 \hat{\mathbf{u}}_0 \cdot \overline{j_0 \hat{\mathbf{u}}_0}\} dx}, \\ \bar{\zeta}_{upp} &= \sqrt{\int_{\Omega} \{\mathbf{E}\mathcal{I}_0 \nabla \hat{\mathbf{p}}_0 \cdot \overline{\mathcal{I}_0 \nabla \hat{\mathbf{p}}_0} + \rho\omega^2 j_0 \hat{\mathbf{p}}_0 \cdot \overline{j_0 \hat{\mathbf{p}}_0}\} dx},\end{aligned}$$

and where the residuals functionals and deviation functions are given in (3.7) and (3.8), respectively.

*Proof:* Only the bounds on  $\|\hat{\mathbf{e}}_1\|_{\mathcal{H}}$  are proved, as the proof for the bounds on  $\|\hat{\varepsilon}_1\|_{\mathcal{H}}$  is similar by using the approximate dual solution  $\hat{\mathbf{p}}_0$  instead of the primal solution  $\hat{\mathbf{u}}_0$ . Recalling the definition of the norm  $\|\cdot\|_{\mathcal{H}}$  and subsequently substituting (3.11)<sup>1</sup>, leads to:

$$\|\hat{\mathbf{e}}_1\|_{\mathcal{H}} = \sup_{\mathbf{w} \in V} \frac{|\mathcal{H}(\hat{\mathbf{e}}_1, \mathbf{w})|}{\|\mathbf{w}\|_{\mathcal{H}}} = \sup_{\mathbf{w} \in V} \frac{|\mathcal{R}(\hat{\mathbf{u}}_0, \mathbf{w})|}{\|\mathbf{w}\|_{\mathcal{H}}}.$$

The lower bound  $\zeta_{low}$  follows quickly from this expression by applying the definition of the supremum and choosing  $\mathbf{w} = \hat{\mathbf{u}}_0$ . To prove the upper bound, recall the explicit expression for the primal residual functional in (3.7)<sup>1</sup>:

$$\|\hat{\mathbf{e}}_1\|_{\mathcal{H}} = \sup_{\mathbf{w} \in V} \frac{\left| \int_{\Omega} \{\mathbf{E}\mathcal{I}_0 \nabla \hat{\mathbf{u}}_0 \cdot \overline{\nabla \mathbf{w}} - \rho\omega^2 j_0 \hat{\mathbf{u}}_0 \cdot \overline{\mathbf{w}}\} dx \right|}{\|\mathbf{w}\|_{\mathcal{H}}}.$$

Applying the triangle and Schwarz inequalities, yields:

$$\begin{aligned}\|\hat{\mathbf{e}}_1\|_{\mathcal{H}} &\leq \sup_{\mathbf{w} \in V} \frac{\left| \int_{\Omega} \mathbf{E}\mathcal{I}_0 \nabla \hat{\mathbf{u}}_0 \cdot \overline{\nabla \mathbf{w}} dx \right| + \left| \int_{\Omega} \rho\omega^2 j_0 \hat{\mathbf{u}}_0 \cdot \overline{\mathbf{w}} dx \right|}{\|\mathbf{w}\|_{\mathcal{H}}} \\ &\leq \sqrt{\int_{\Omega} \{\mathbf{E}\mathcal{I}_0 \nabla \hat{\mathbf{u}}_0 \cdot \overline{\mathcal{I}_0 \nabla \hat{\mathbf{u}}_0} + \rho\omega^2 j_0 \hat{\mathbf{u}}_0 \cdot \overline{j_0 \hat{\mathbf{u}}_0}\} dx}.\end{aligned}$$

■

Numerical verifications of these upper and lower bounds in Section 3.6 show that they can be used to estimate  $\|\hat{\mathbf{e}}_1\|_{\mathcal{H}}$  and  $\|\hat{\varepsilon}_1\|_{\mathcal{H}}$  within reasonable accuracy. However, of more interest are  $\|\mathbf{e}_0\|_{\mathcal{H}}$  and  $\|\varepsilon_0\|_{\mathcal{H}}$ . The following lemma shows that these norms are bounded from below by their elliptic counterparts.

**Lemma 3.5.2** *Given the solution pairs  $(\hat{\mathbf{e}}_0, \hat{\varepsilon}_0)$  and  $(\hat{\mathbf{e}}_1, \hat{\varepsilon}_1)$  to (3.9) and (3.11), respectively, there exist positive  $C_1(\Omega, \beta, \mathbf{E}, \omega)$  and  $C_2(\Omega, \beta, \mathbf{E}, \omega)$ , such that:*

$$\|\hat{\mathbf{e}}_1\|_{\mathcal{H}} \leq C_1 \|\hat{\mathbf{e}}_0\|_{\mathcal{H}}, \quad \|\hat{\varepsilon}_1\|_{\mathcal{H}} \leq C_2 \|\hat{\varepsilon}_0\|_{\mathcal{H}}.$$

*Proof:* Again, only the first of the two inequalities needs to be proved. Now, recalling the definition of the norm  $\|\cdot\|_{\mathcal{H}}$  and subsequently substituting (3.11)<sup>1</sup>, one obtains:

$$\|\hat{\mathbf{e}}_1\|_{\mathcal{H}} = \sup_{\mathbf{w} \in V} \frac{|\mathcal{H}(\hat{\mathbf{e}}_1, \mathbf{w})|}{\|\mathbf{w}\|_{\mathcal{H}}} = \sup_{\mathbf{w} \in V} \frac{|\mathcal{B}(\hat{\mathbf{e}}_0, \mathbf{w})|}{\|\mathbf{w}\|_{\mathcal{H}}}.$$

Substituting the definition of  $\mathcal{B}(\cdot, \cdot)$ , given in (2.7), and by applying the Schwarz inequality, leads to:

$$\begin{aligned} \|\hat{\mathbf{e}}_1\|_{\mathcal{H}} &\leq \sup_{\mathbf{w} \in V} \frac{\sqrt{\mathcal{A}(\mathbf{w}, \mathbf{w}) + \omega^2 \mathcal{C}(\mathbf{w}, \mathbf{w}) + \omega \mathcal{D}(\mathbf{w}, \mathbf{w})}}{\|\mathbf{w}\|_{\mathcal{H}}} \\ &\quad \times \sqrt{\mathcal{A}(\hat{\mathbf{e}}_0, \hat{\mathbf{e}}_0) + \omega^2 \mathcal{C}(\hat{\mathbf{e}}_0, \hat{\mathbf{e}}_0) + \omega \mathcal{D}(\hat{\mathbf{e}}_0, \hat{\mathbf{e}}_0)}. \end{aligned} \quad (3.30)$$

For arbitrary  $\mathbf{v} \in V$ , its trace  $\gamma_0 \mathbf{v}$  on  $\Gamma_t$  is in  $H^{1/2}(\Gamma_t)$ . Thus:

$$\mathcal{D}(\mathbf{v}, \mathbf{v}) \leq \|\beta\|_{L^\infty(\Gamma_t)} \|\gamma_0 \mathbf{v}\|_{L^2(\Gamma_t)}^2 \leq \|\beta\|_{L^\infty(\Gamma_t)} \|\gamma_0 \mathbf{v}\|_{H^{1/2}(\Gamma_t)}^2.$$

The classical trace theorem for functions in  $H^1(\Omega)$ , is used to obtain:

$$\begin{aligned} \mathcal{D}(\mathbf{v}, \mathbf{v}) &\leq C(\Omega) \|\beta\|_{L^\infty(\Gamma_t)} \|\mathbf{v}\|_{H^1(\Omega)}^2 \\ &\leq C(\Omega) \|\beta\|_{L^\infty(\Gamma_t)} \|\mathbf{E}^{-1}\|_{L^\infty(\Gamma_t)} \mathcal{A}(\mathbf{v}, \mathbf{v}). \end{aligned}$$

The proof is completed by backsubstituting this last inequality into (3.30).  $\blacksquare$

In Section 3.6, numerical verifications are presented which show that with sufficient damping,  $\|\hat{\mathbf{e}}_1\|_{\mathcal{H}}$  and  $\|\hat{\varepsilon}_1\|_{\mathcal{H}}$  are close to  $\|\hat{\mathbf{e}}_0\|_{\mathcal{H}}$  and  $\|\hat{\varepsilon}_0\|_{\mathcal{H}}$ . Hence, by estimating the global norms of the elliptic representations of the error functions within reasonable accuracy, a reasonably reliable indication of the global norms of the error functions themselves is obtained.

## 3.6 Numerical Experiments

In this section, several numerical verifications of the bounds and estimates, are presented. Sections 3.6.1 through 3.6.3 consider the case of steady state wave propagation for a wide range of frequencies. In these sections, the effect of several problem parameters on the accuracy of the modeling error estimators are analyzed: Section 3.6.1 concentrates on the effect of the *impedance* ratio of the elastic constituents in the material, Section 3.6.2 considers the influence of damping boundary conditions, and finally Section 3.6.3 shows the case where the material has two zones in which the characteristic length of the inhomogeneity is different. A transient test problem is given in Section 3.6.4.

### 3.6.1 Steady State Case I: a Composite Material with Periodic Microstructure

Consider the problem configuration shown in Figure 3.1: a beam with length  $L$  is clamped at its left edge ( $x = 0$ ) and supported at its right edge by a damper with

damping coefficient  $\beta = \sqrt{E(L)\rho(L)}$ . The beam has a material microstructure which is made out of two elastic constituents with material properties  $\{E_1, \rho_1\}$  and  $\{E_2, \rho_2\}$ , that are periodically layered throughout the beam with a constant layer thickness  $d$ . For this test problem, the source terms (the RHS in (2.4)) are characterized by an initial displacement field. Thus,  $\mathbf{V}_0(x) = 0$  and  $\mathbf{U}_0(x)$  is a symmetric pulse located around the center point of the beam  $x_0$  with width  $\delta$ :

$$\mathbf{U}_0(x) = \frac{1}{\delta^4} [x - (x_0 - \delta)]^2 [x - (x_0 + \delta)]^2 [1 - H(x - (x_0 - \delta))] [1 - H(x - (x_0 + \delta))], \quad (3.31)$$

where  $H(x - a)$  denotes the Heaviside function. The quantity of interest for this numerical example is the average stress on a small domain  $S = (24, 25) \subset \Omega$ :

$$\hat{Q}(\hat{\mathbf{u}}) = \int_{x=24}^{x=25} \left( E \frac{d\hat{\mathbf{u}}}{dx} \right) dx.$$

To obtain the solution pairs  $(\hat{\mathbf{u}}, \hat{\mathbf{p}})$  and  $(\hat{\mathbf{u}}_0, \hat{\mathbf{p}}_0)$  to (3.2) and (3.4), respectively, an overkill computation is performed by using approximately 800 quadratic elements. The approximate material model  $\{E_0, \rho_0\}$  is obtained by employing a standard classical asymptotic homogenization technique [23]. Hence,  $\{E_0, \rho_0\}$  are constant throughout the beam.

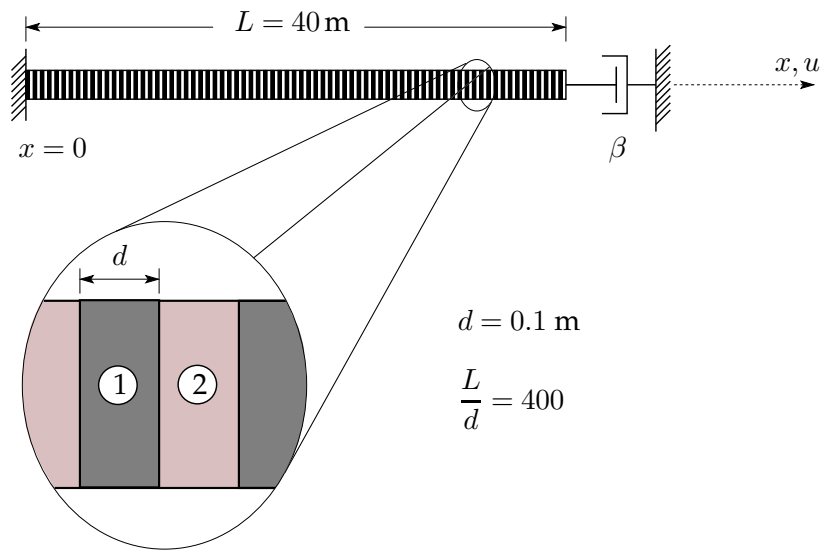
In Figures 3.2 through 3.5, the solutions  $(\hat{\mathbf{u}}, \hat{\mathbf{p}})$  and  $(\hat{\mathbf{u}}_0, \hat{\mathbf{p}}_0)$  are shown for radial frequencies  $\omega$  of 500, 1000, 2000, and 4000 Hz. In these figures, the fine scale solutions  $(\hat{\mathbf{u}}, \hat{\mathbf{p}})$  are plotted as solid red lines and the coarse scale solutions  $(\hat{\mathbf{u}}_0, \hat{\mathbf{p}}_0)$  as dashed green lines. These figures are obtained for the case where the beam consists out of a carbon-epoxy composite; a material that is commonly used in engineering applications:

$E_1 = 120 \text{ GPa}, \quad \rho_1 = 8 \text{ g/cm}^3, \quad (\text{Carbon fiber})$
$E_2 = 6 \text{ GPa}, \quad \rho_2 = 3 \text{ g/cm}^3, \quad (\text{Epoxy})$

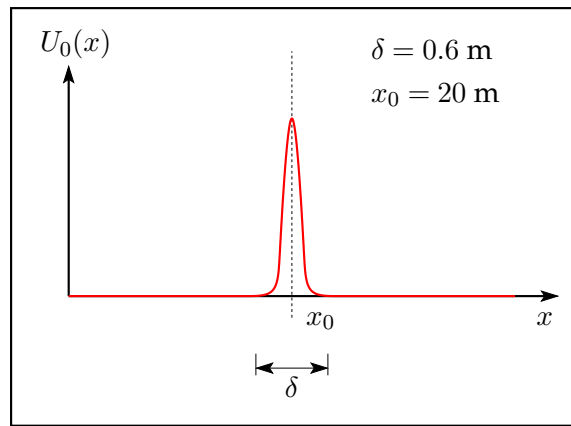
which corresponds to an *impedance ratio*,  $\tau = \sqrt{\frac{E_1 \rho_1}{E_2 \rho_2}}$ , of approximately 7.3. This value is more likely to trigger dispersion. The corresponding homogenized material properties for the coarse scale problem (3.4) are approximately:

$$E_0 = 11.4 \text{ GPa}, \quad \rho_0 = 5.5 \text{ g/cm}^3.$$

A first observation from Figures 3.2 through 3.5, is that for the low frequencies of 500 and 1000 Hz, the approximate solution  $\hat{\mathbf{u}}_0 \approx \hat{\mathbf{u}}$ . In this frequency range, the wave lengths are considerably larger than the characteristic length of the inhomogeneity  $d$ . Consequently, the wave structure is insensitive to the heterogeneous layers and propagates as if the material is homogeneous. For these frequencies, the error in the average stress is entirely caused by the mismatch of  $E(x)$  and  $E_0$  in the domain of interest. For higher frequencies, however, the waves start to notice the inhomogeneity. At  $\omega = 2000$  Hz, the amplitudes of the two solutions already are slightly different. At  $\omega = 4000$  Hz,



(a) Problem configuration.



(b) Initial displacement field

Figure 3.1: Steady state problem for a composite material with periodic microstructure.

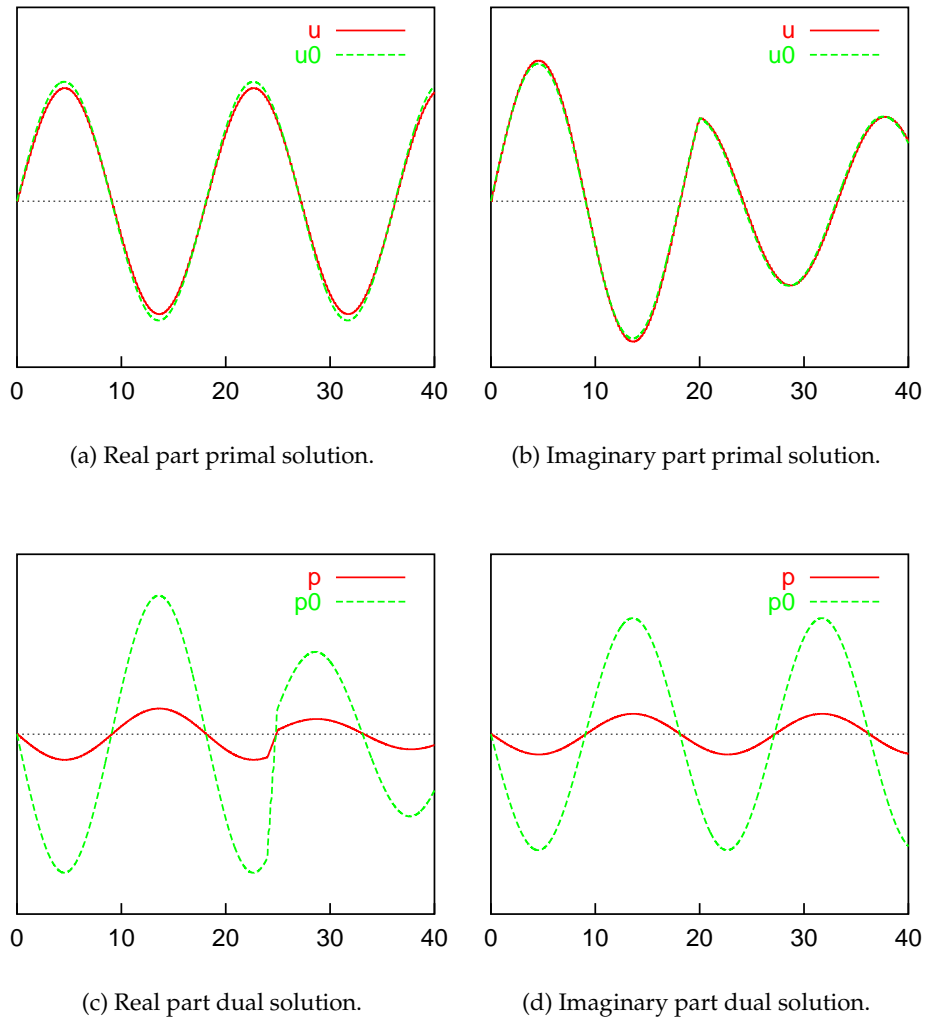


Figure 3.2: Steady state solutions of a periodically layered material with impedance ratio  $\tau = 7.30$  and for a radial frequency of 500 Hz, normalized by  $\|\hat{\mathbf{u}}_0\|_{L^\infty(\Omega)}$  and  $\|\hat{\mathbf{p}}_0\|_{L^\infty(\Omega)}$ .

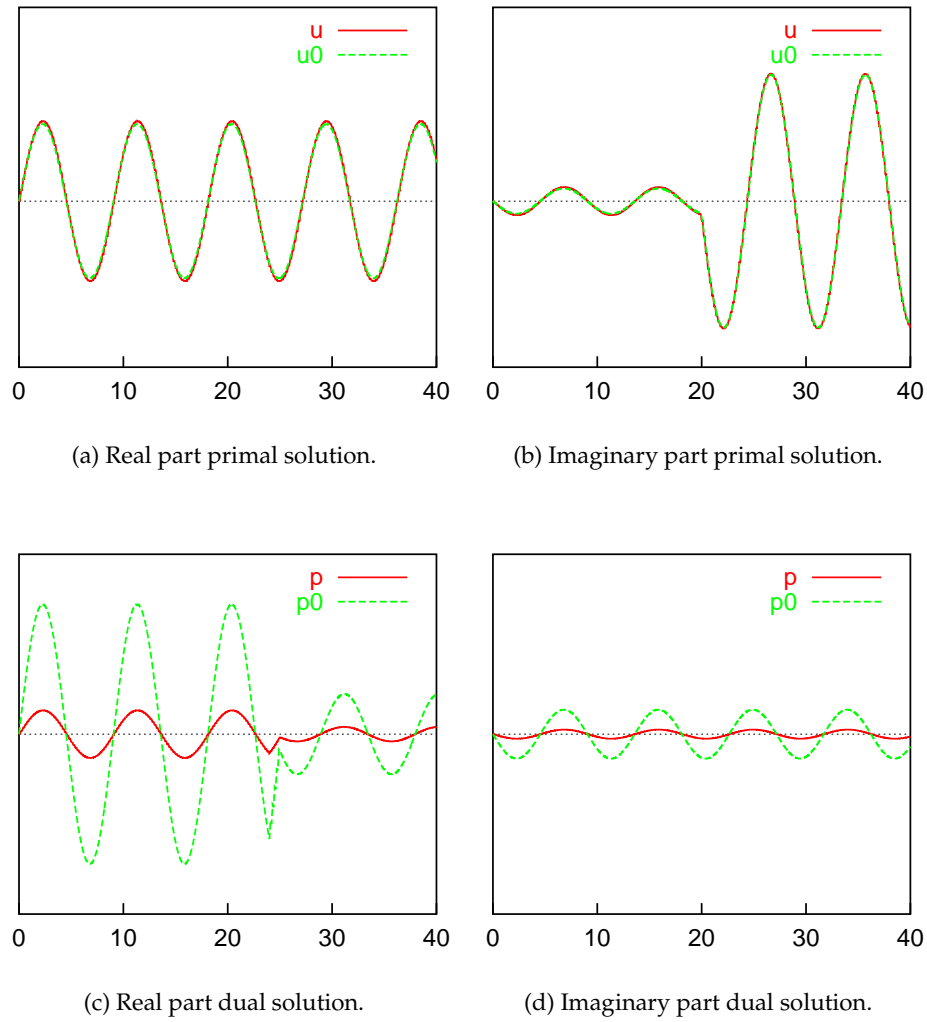


Figure 3.3: Steady state solutions of a periodically layered material with impedance ratio  $\tau = 7.30$  and for a radial frequency of 1000 Hz, normalized by  $\|\hat{\mathbf{u}}_0\|_{L^\infty(\Omega)}$  and  $\|\hat{\mathbf{p}}_0\|_{L^\infty(\Omega)}$ .

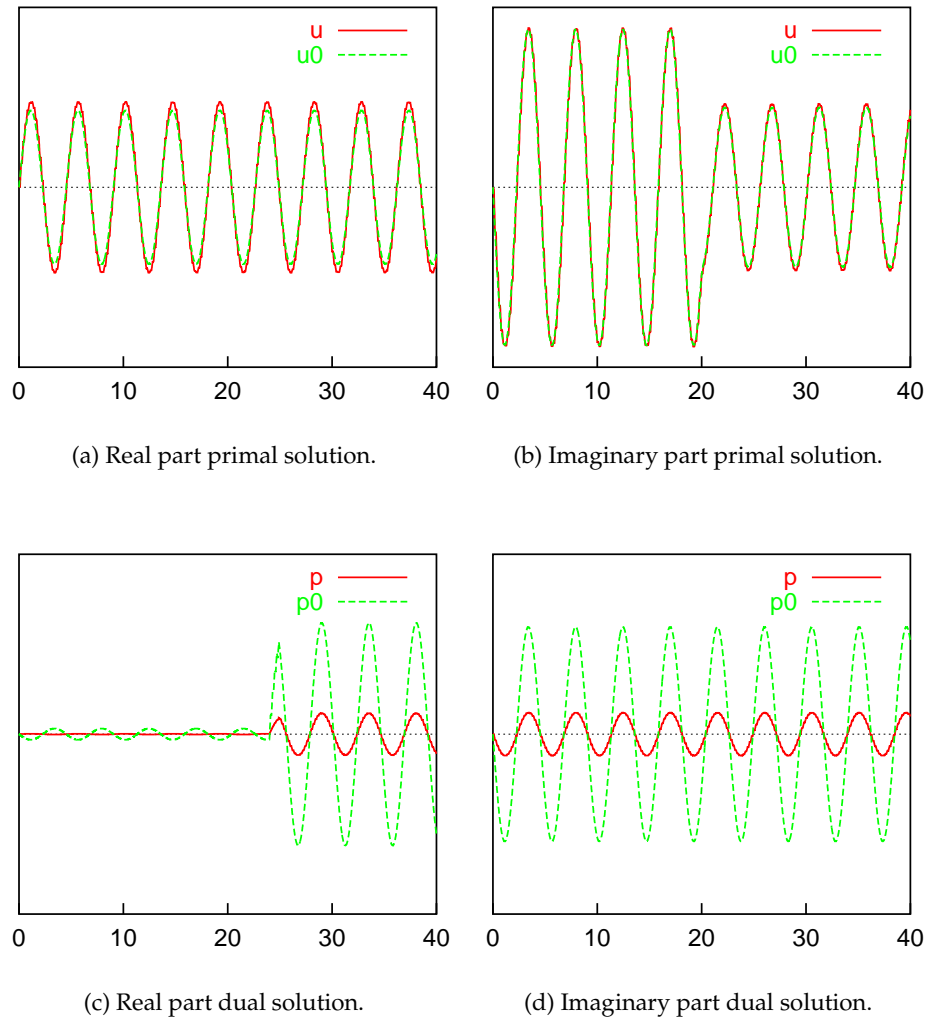
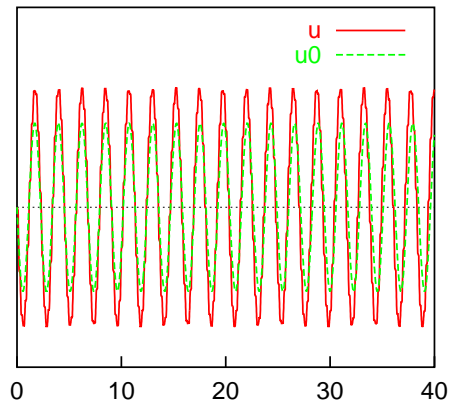
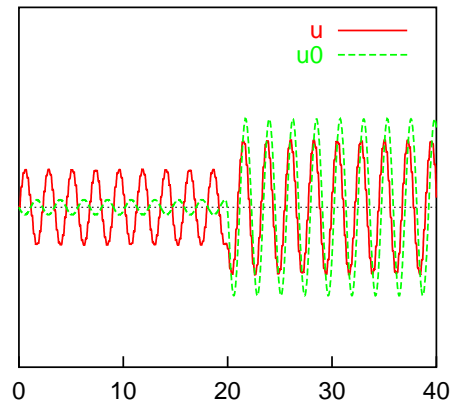


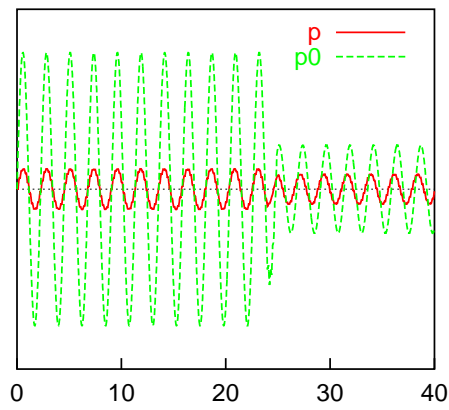
Figure 3.4: Steady state solutions of a periodically layered material with impedance ratio  $\tau = 7.30$  and a radial frequency of 2000 Hz, normalized by  $\|\hat{\mathbf{u}}_0\|_{L^\infty(\Omega)}$  and  $\|\hat{\mathbf{p}}_0\|_{L^\infty(\Omega)}$ .



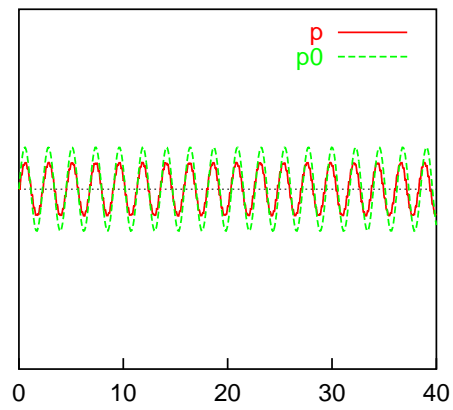
(a) Real part primal solution.



(b) Imaginary part primal solution.



(c) Real part dual solution.



(d) Imaginary part dual solution.

Figure 3.5: Steady state solutions of a periodically layered material with impedance ratio  $\tau = 7.30$  and a radial frequency of 4000 Hz, normalized by  $\|\hat{\mathbf{u}}_0\|_{L^\infty(\Omega)}$  and  $\|\hat{\mathbf{p}}_0\|_{L^\infty(\Omega)}$ .

the inhomogeneity of the microstructure dominates the solution. The amplitudes of  $\hat{\mathbf{u}}$  and  $\hat{\mathbf{u}}_0$  differ considerably and there is a noticeable difference in phase.

The dual solutions  $\hat{\mathbf{p}}$  and  $\hat{\mathbf{p}}_0$  are *global* functions. This is a distinctive difference with the elastostatic case [19, 27, 20, 26], where the dual solutions have very local behavior, damping out quickly from local responses. The ellipticity of the elastostatic problem keeps the sensitivity of the solutions local. However, for the elastodynamic case, the hyperbolic nature of the wave problem causes the primal solution to be sensitive to global features. As a consequence, the dual solution shows global behavior. This is one of the major complications in both modeling error estimation and adaptive modeling of the wave problem. It requires a successful adaptive modeling scheme to be able to perform nonlocal adaptation to control the modeling error.

Returning to Figures 3.2 through 3.5, one sees that apart from the amplitude mismatches between  $\hat{\mathbf{p}}$  and  $\hat{\mathbf{p}}_0$ , the dual solutions show similar behavior as their primal counterparts. The higher amplitude mismatch is caused by the fact that the force term in the dual problem has a much larger amplitude, due to the presence of the elasticity modulus.

For a radial frequency  $\omega = 500$  Hz, Tables 3.1 through 3.3 show results on the accuracy of the bounds and estimators derived in Sections 3.5.1 and 3.5.2. To test the influence of the material properties, results for three different impedance ratios:  $\tau = 1.82, 3.65,$  and  $7.30$  are presented.

In Table 3.1, the effectivity indices are listed for the global bounds of Lemma 3.5.1. In the upper part, the effectivity indices with respect to the global error norms  $\|\hat{\mathbf{e}}_1\|_{\mathcal{H}}$  and  $\|\hat{\varepsilon}_1\|_{\mathcal{H}}$  are shown. The upper bounds  $\zeta_{\text{upp}}$  and  $\bar{\zeta}_{\text{upp}}$  have good effectivity indices, close to 1.0, which improve as the impedance ratio increases. The lower bounds  $\zeta_{\text{low}}$  and  $\bar{\zeta}_{\text{low}}$  have poor accuracy for low impedance ratios, but improve significantly as the ratio increases. The lower part in Table 3.1 shows the accuracy with respect to the global error norms  $\|\hat{\mathbf{e}}_0\|_{\mathcal{H}}$  and  $\|\hat{\varepsilon}_0\|_{\mathcal{H}}$ . It is clear that the global norms of the elliptic representations  $(\hat{\mathbf{e}}_1, \hat{\varepsilon}_1)$  are very close to the actual error norms. Consequently, as the effectivity indices reveal, the upper bounds  $\zeta_{\text{upp}}$  and  $\bar{\zeta}_{\text{upp}}$  are close to the error norms as well and represent accurate estimators of the global error norms, to within 2.6 and 10% accuracy, respectively. In Table 3.2, the effectivity indices are listed for the upper and lower bounds  $\eta_{\text{upp}(i)}^{\pm}$  and  $\eta_{\text{low}(i)}^{\pm}$  of Lemma 3.4.1. Also, the effectivity indices for  $\alpha_{(i)}^{\pm}$  are shown. These terms represent the lower bounds given in (3.27). The upper bounds  $\eta_{\text{upp}(i)}^{\pm}$  are very accurate estimators within 1.5%. For low  $\tau$ , the lower bounds  $\eta_{\text{low}(i)}^{\pm}$  have poor accuracy, but they improve to within 5% accuracy as  $\tau$  increases. The accuracy of the estimators  $\xi_{(i)}^{\pm}$  that are proposed in Section 3.5.1 and are derived by estimating the terms  $\alpha_{(i)}^{\pm}$ , is remarkable. Their accuracy lies within 0.5% and is rather insensitive to the impedance ratio  $\tau$ .

From the results in Table 3.2, one would expect that the proposed error estimators  $\gamma_{\text{upp}}$  and  $\gamma_{\text{est}}$  (see Section 3.5.1) should be accurate estimators of the modeling error in the average stress. Table 3.3 lists the effectivity indices of these estimators, where the effectivity index is defined by the following ratio:

$$\text{effectivity index} = \frac{|\text{estimator}|}{|\hat{\mathcal{Q}}(\hat{\mathbf{e}}_0)|}$$

$\tau$	1.82	3.65	7.30
$\zeta_{\text{upp}}$	1.026	1.005	1.026
$\zeta_{\text{low}}$	0.560	0.709	0.881
$\bar{\zeta}_{\text{upp}}$	1.013	1.005	1.016
$\bar{\zeta}_{\text{low}}$	0.618	0.761	0.891
$\ \hat{\mathbf{e}}_1\ _{\mathcal{H}}$	0.999	0.999	0.999
$\ \hat{\varepsilon}_1\ _{\mathcal{H}}$	0.908	0.902	0.927
$\zeta_{\text{upp}}$	1.026	1.005	1.026
$\zeta_{\text{low}}$	0.560	0.709	0.881
$\bar{\zeta}_{\text{upp}}$	0.921	0.907	0.942
$\bar{\zeta}_{\text{low}}$	0.561	0.687	0.826

Table 3.1: Effectivity indices with respect to  $\|\hat{\mathbf{e}}_1\|_{\mathcal{H}}$  and  $\|\hat{\varepsilon}_1\|_{\mathcal{H}}$  (upper part), and  $\|\hat{\mathbf{e}}_0\|_{\mathcal{H}}$  and  $\|\hat{\varepsilon}_0\|_{\mathcal{H}}$  (lower part), for a periodically layered material and a radial frequency of 500 Hz.

$\tau$	1.82	3.65	7.30
$\eta_{\text{upp},(i)}^{\pm}$	1.013	1.005	1.016
$\eta_{\text{low},(i)}^{\pm}$	0.785	0.842	0.914
$\alpha_{(i)}^{\pm}$	0.998	0.999	0.999
$\xi_{(i)}^{\pm}$	0.995	1.000	0.998

Table 3.2: Effectivity indices of upper and lower bounds to the terms coming from the polarization formula expansion (3.16), for a periodically layered material, and for radial frequency of 500 Hz.

$\tau$	1.82	3.65	7.30
$ \hat{Q}(\hat{\mathbf{e}}_0)/\hat{Q}(\hat{\mathbf{u}}) $	0.807(0)	0.197(1)	0.463(1)
$\gamma^*$	1.002	0.977	1.030
$\gamma_{\text{upp}}$	1.008	1.145	3.098
$\gamma_{\text{low}}$	4.251	11.008	20.050
$\gamma_{\text{avg}}$	2.328	5.108	8.545
$\gamma_{\text{est}}$	1.052	0.887	0.976

Table 3.3: Relative error and effectivity indices of the modeling error estimators, for a periodically layered material, and radial frequency of 500 Hz.

Indeed, the accuracy for  $\gamma_{\text{est}}$  is remarkably good. The effectivity index for this estimator varies closely around 1.0 for all impedance ratios. The estimator  $\gamma_{\text{upp}}$  provides a good estimate for low impedance ratios and becomes increasingly inaccurate as  $\tau$  increases. As expected from the results in Table 3.2, the estimators  $\gamma_{\text{low}}$  and  $\gamma_{\text{avg}}$  have poorer effectivity indices due to the inaccuracy of the lower bounds  $\eta_{\text{low}(i)}^{\pm}$ . Note that  $\gamma_{\text{avg}}$  represents a decent estimator for low  $\tau$  (within the order of the error), but is very sensitive to material impedance ratio.

The effectivity indices for the “intermediate” estimator  $\gamma^*$ , which is derived by eliminating the  $\hat{\mathbf{e}}_0$  terms from (3.14) (see Section 3.3), show that this estimator is a good intermediate estimate. By ignoring the  $\hat{\mathbf{e}}_0$  terms, little accuracy is lost. The accuracy remains within 10%.

Also, in Table 3.3, the relative error is listed. Even at this low frequency, the modeling error can be large: one order higher than the quantity of interest itself. As later examples show, the error can be a factor 100 or 1000 higher. This is a characteristic feature of the wave problem. The orders of the modeling error can be substantially larger than for the elastostatics case. This forms a first indication that control of the relative modeling error to within 5 or 2% will be computationally expensive and, most likely, not feasible in most applications. Tables 3.4 through 3.12 list the results for higher radial frequencies of 1000, 2000, and 4000 Hz. Comparing these results with those we discussed previously (for 500 Hz), it is observed from Tables 3.4 through 3.6 that the effectivity of the global bounds  $\zeta_{\text{upp}}$ ,  $\bar{\zeta}_{\text{upp}}$ ,  $\zeta_{\text{low}}$ , and  $\bar{\zeta}_{\text{low}}$  vary only slightly within an accuracy of  $\pm 5\%$ , as the frequency increases.

In Tables 3.7 through 3.9, the effectivity indices for the bounds  $\eta_{\text{upp}(i)}^{\pm}$  and  $\eta_{\text{low}(i)}^{\pm}$  show a similar behavior, with a 5% increase and decrease, respectively. However, again the effectivity indices for  $\xi_{(i)}^{\pm}$  behave remarkably well. Only a slight change of accuracy is noticed: in the order of 1% or less. Consequently, the accuracy of the corresponding estimator  $\gamma_{\text{est}}$  remains good even as the frequencies increase (see Tables 3.10 through 3.12). The order of the change of accuracy is much larger than for the bounds

$\tau$	1.82	3.65	7.30
$\zeta_{\text{upp}}$	1.024	1.005	1.028
$\zeta_{\text{low}}$	0.566	0.716	0.880
$\bar{\zeta}_{\text{upp}}$	1.021	1.007	1.022
$\bar{\zeta}_{\text{low}}$	0.583	0.758	0.888
$\ \hat{\mathbf{e}}_1\ _{\mathcal{H}}$	0.998	0.999	0.999
$\ \hat{\varepsilon}_1\ _{\mathcal{H}}$	0.849	0.892	0.907
$\zeta_{\text{upp}}$	1.023	1.004	1.028
$\zeta_{\text{low}}$	0.565	0.715	0.880
$\bar{\zeta}_{\text{upp}}$	0.868	0.899	0.927
$\bar{\zeta}_{\text{low}}$	0.495	0.677	0.805

Table 3.4: Effectivity indices with respect to  $\|\hat{\mathbf{e}}_1\|_{\mathcal{H}}$  and  $\|\hat{\varepsilon}_1\|_{\mathcal{H}}$  (upper part), and  $\|\hat{\mathbf{e}}_0\|_{\mathcal{H}}$  and  $\|\hat{\varepsilon}_0\|_{\mathcal{H}}$  (lower part), for a periodically layered material and radial frequency of 1000 Hz.

$\xi_{(i)}^\pm$ , since these terms estimate norms of large magnitude. Hence, a small variation in accuracy of  $\xi_{(i)}^\pm$  is amplified by large terms, resulting in a higher variation of the accuracy of  $\gamma_{\text{est}}$ . However, the variation stays within an order of 1 or 2 with respect to the modeling error, and consequently  $\gamma_{\text{est}}$  still remains an accurate estimator.

$\tau$	1.82	3.65	7.30
$\zeta_{\text{upp}}$	1.025	1.005	1.028
$\zeta_{\text{low}}$	0.563	0.718	0.880
$\bar{\zeta}_{\text{upp}}$	1.025	1.005	1.027
$\bar{\zeta}_{\text{low}}$	0.573	0.724	0.882
$\ \hat{\mathbf{e}}_1\ _{\mathcal{H}}$	0.997	0.995	0.998
$\ \hat{\varepsilon}_1\ _{\mathcal{H}}$	0.837	0.840	0.887
$\zeta_{\text{upp}}$	1.023	1.001	1.027
$\zeta_{\text{low}}$	0.561	0.715	0.878
$\bar{\zeta}_{\text{upp}}$	0.858	0.845	0.912
$\bar{\zeta}_{\text{low}}$	0.480	0.608	0.783

Table 3.5: Effectivity indices with respect to  $\|\hat{\mathbf{e}}_1\|_{\mathcal{H}}$  and  $\|\hat{\varepsilon}_1\|_{\mathcal{H}}$  (upper part), and  $\|\hat{\mathbf{e}}_0\|_{\mathcal{H}}$  and  $\|\hat{\varepsilon}_0\|_{\mathcal{H}}$  (lower part), for a periodically layered material and radial frequency of 2000 Hz.

$\tau$	1.82	3.65	7.30
$\zeta_{\text{upp}}$	1.027	1.005	1.028
$\zeta_{\text{low}}$	0.562	0.716	0.880
$\bar{\zeta}_{\text{upp}}$	1.027	1.006	1.028
$\bar{\zeta}_{\text{low}}$	0.567	0.723	0.881
$\ \hat{\mathbf{e}}_1\ _{\mathcal{H}}$	0.986	0.995	0.916
$\ \hat{\varepsilon}_1\ _{\mathcal{H}}$	0.824	0.837	0.883
$\zeta_{\text{upp}}$	1.013	1.000	0.942
$\zeta_{\text{low}}$	0.554	0.713	0.806
$\bar{\zeta}_{\text{upp}}$	0.847	0.843	0.907
$\bar{\zeta}_{\text{low}}$	0.468	0.606	0.778

Table 3.6: Effectivity indices with respect to  $\|\hat{\mathbf{e}}_1\|_{\mathcal{H}}$  and  $\|\hat{\varepsilon}_1\|_{\mathcal{H}}$  (upper part), and  $\|\hat{\mathbf{e}}_0\|_{\mathcal{H}}$  and  $\|\hat{\varepsilon}_0\|_{\mathcal{H}}$  (lower part), for a periodically layered material and radial frequency of 4000 Hz.

$\tau$	1.82	3.65	7.30
$\eta_{\text{upp},(i)}^{\pm}$	1.021	1.007	1.022
$\eta_{\text{low},(i)}^{\pm}$	0.635	0.826	0.876
$\xi_{(i)}^{\pm}$	0.987	1.002	0.999

Table 3.7: Effectivity indices of upper and lower bounds to the terms coming from the polarization formula expansion (3.16), for a periodically layered material and radial frequency of 1000 Hz.

$\tau$	1.82	3.65	7.30
$\eta_{\text{upp},(i)}^{\pm}$	1.025	1.005	1.027
$\eta_{\text{low},(i)}^{\pm}$	0.583	0.732	0.843
$\xi_{(i)}^{\pm}$	0.984	0.997	0.991

Table 3.8: Effectivity indices of upper and lower bounds to the terms coming from the polarization formula expansion (3.16), for a periodically layered material and radial frequency of 2000 Hz.

$\tau$	1.82	3.65	7.30
$\eta_{\text{upp},(i)}^{\pm}$	1.027	1.006	1.028
$\eta_{\text{low},(i)}^{\pm}$	0.554	0.727	0.838
$\xi_{(i)}^{\pm}$	0.987	0.998	0.997

Table 3.9: Effectivity indices of upper and lower bounds to the terms coming from the polarization formula expansion (3.16), for a periodically layered material and radial frequency of 4000 Hz.

$\tau$	1.82	3.65	7.30
$ \hat{Q}(\hat{\mathbf{e}}_0)/\hat{Q}(\hat{\mathbf{u}}) $	0.860(0)	0.199(1)	0.449(1)
$\gamma^*$	1.036	0.998	0.989
$\gamma_{\text{upp}}$	0.663	1.014	2.639
$\gamma_{\text{low}}$	16.188	7.825	10.623
$\gamma_{\text{avg}}$	7.973	3.975	4.178
$\gamma_{\text{est}}$	1.617	1.000	1.138

Table 3.10: Relative error and effectivity indices of the modeling error estimators, for a periodically layered material and radial frequency of 1000 Hz.

$\tau$	1.82	3.65	7.30
$ \hat{Q}(\hat{\mathbf{e}}_0)/\hat{Q}(\hat{\mathbf{u}}) $	0.793(0)	0.219(1)	0.382(1)
$\gamma^*$	1.002	1.108	0.732
$\gamma_{\text{upp}}$	1.436	0.800	17.993
$\gamma_{\text{low}}$	14.257	46.083	90.183
$\gamma_{\text{avg}}$	6.731	22.96	36.096
$\gamma_{\text{est}}$	1.063	1.710	3.283

Table 3.11: Relative error and effectivity indices of the modeling error estimators, for a periodically layered material and radial frequency of 2000 Hz.

$\tau$	1.82	3.65	7.30
$ \hat{Q}(\hat{\mathbf{e}}_0)/\hat{Q}(\hat{\mathbf{u}}) $	0.705(0)	0.221(1)	0.425(1)
$\gamma^*$	0.858	1.027	0.999
$\gamma_{\text{upp}}$	3.981	1.107	14.219
$\gamma_{\text{low}}$	46.875	24.932	78.083
$\gamma_{\text{avg}}$	21.509	12.301	31.960
$\gamma_{\text{est}}$	1.876	1.114	0.921

Table 3.12: Relative error and effectivity indices of the modeling error estimators, for a periodically layered material and radial frequency of 4000 Hz.

### 3.6.2 Steady State Case II: Effect of Damping

In this section, the effect of the damping boundary condition on the accuracy of the estimators is investigated. It is well known that diminishing the damping in the system, has a destabilizing effect on the problem formulation. To verify that such a destabilizing influence does not affect the accuracy of the error estimators, a set of numerical verifications is performed, using the same problem configuration as in Section 3.6.1 (see also Figure 3.1), but now the damping coefficient  $\beta$  is decreased by multiplying this coefficient by a constant parameter  $\beta^*$ .

In Table 3.13, results for a radial frequency of 4000 Hz and a set of decreasing values of  $\beta^*$  are shown for the effectivity indices of the global norm estimators of Lemma 3.5.1. The accuracy with respect to the norms  $\|\hat{\mathbf{e}}_1\|_{\mathcal{H}}$  and  $\|\hat{\varepsilon}_1\|_{\mathcal{H}}$  appears to be indifferent to the variation of the damping coefficient. However, the results clearly indicate that as damping decreases,  $\|\hat{\mathbf{e}}_1\|_{\mathcal{H}}$  and  $\|\hat{\varepsilon}_1\|_{\mathcal{H}}$  become poor lower bounds to respectively  $\|\hat{\mathbf{e}}_0\|_{\mathcal{H}}$  and  $\|\hat{\varepsilon}_0\|_{\mathcal{H}}$ ; especially  $\|\hat{\mathbf{e}}_0\|_{\mathcal{H}}$ . As a direct result, the bounds  $\zeta_{\text{upp}}$ ,  $\zeta_{\text{low}}$ ,  $\bar{\zeta}_{\text{upp}}$ , and  $\bar{\zeta}_{\text{low}}$ , become very poor estimators of the global error bounds when there is very little damping in the system.

Fortunately, the accuracy of the bounds  $\eta_{\text{upp}(,i)}^{\pm}$ ,  $\eta_{\text{low}(,i)}^{\pm}$ , and  $\xi_{(,i)}^{\pm}$  is indifferent to the variation of  $\beta$ , as is shown in Table 3.14. In addition, Table 3.15 illustrates that the intermediate estimator  $\gamma^*$ , as given in (3.17), is just slightly sensitive to the variation in the damping, but still remains close to 1. Recalling the derivations in Section 3.5.1 and apply these two observations, one would expect that the estimators  $\gamma_{\text{est}}$  and  $\gamma_{\text{upp}}$  would maintain their accuracy as  $\beta^*$  varies.

From Table 3.15, we conclude, however, that there is a noticeable change in accuracy. The accuracy of  $\gamma_{\text{est}}$  still remains acceptable, yet has changed an order of 2. This can be explained by the fact that the top row in Table 3.15 indicates a dramatic drop

$\beta^*$	$10^0$	$10^{-1}$	$10^{-2}$	$10^{-4}$	$10^{-8}$
$\zeta_{\text{upp}}$	1.028	1.028	1.028	1.028	1.028
$\zeta_{\text{low}}$	0.880	0.880	0.880	0.880	0.880
$\bar{\zeta}_{\text{upp}}$	1.028	1.028	1.028	1.028	1.028
$\bar{\zeta}_{\text{low}}$	0.881	0.881	0.881	0.881	0.881
$\ \hat{\mathbf{e}}_1\ _{\mathcal{H}}$	0.916	0.207	0.133	0.132	0.132
$\ \hat{\varepsilon}_1\ _{\mathcal{H}}$	0.883	0.805	0.719	0.718	0.718
$\zeta_{\text{upp}}$	0.942	0.213	0.137	0.135	0.135
$\zeta_{\text{low}}$	0.806	0.183	0.117	0.116	0.116
$\bar{\zeta}_{\text{upp}}$	0.907	0.827	0.740	0.738	0.738
$\bar{\zeta}_{\text{low}}$	0.778	0.709	0.634	0.632	0.632

Table 3.13: Effectivity indices with respect to  $\|\hat{\mathbf{e}}_1\|_{\mathcal{H}}$  and  $\|\hat{\varepsilon}_1\|_{\mathcal{H}}$  (upper part), and  $\|\hat{\mathbf{e}}_0\|_{\mathcal{H}}$  and  $\|\hat{\varepsilon}_0\|_{\mathcal{H}}$  (lower part), for a periodically layered material and a radial frequency of 4000 Hz.

in the relative modeling error. We now recall the following equation:

$$\begin{aligned} \gamma^* = & \mathcal{R}(\hat{\mathbf{u}}_0, \hat{\mathbf{p}}_0) + \frac{1}{4} \|\hat{\mathbf{e}}_1 + \hat{\varepsilon}_1\|_{\mathcal{H}}^2 - \frac{1}{4} \|\hat{\mathbf{e}}_1 - \hat{\varepsilon}_1\|_{\mathcal{H}}^2 \\ & + \frac{i}{4} \|\hat{\mathbf{e}}_1 + i\hat{\varepsilon}_1\|_{\mathcal{H}}^2 - \frac{i}{4} \|\hat{\mathbf{e}}_1 - i\hat{\varepsilon}_1\|_{\mathcal{H}}^2. \end{aligned} \quad (3.17)$$

As shown in Section 3.5.1, the estimates  $\gamma_{\text{est}}$  and  $\gamma_{\text{upp}}$  are derived from this expression by estimating the norms in the RHS. These norms are extremely large and as the error and  $\gamma^*$  become smaller, it will require a higher accuracy on the estimates of the norms to maintain the overall accuracy of the error estimators. Since the accuracy on the norm estimates remains practically unchanged, a loss in accuracy of the estimate of the modeling error in the average stress is obtained.

It is observed that  $\gamma_{\text{est}}$  provides an excellent indicator of the modeling error for all frequencies.

$\beta^*$	$10^0$	$10^{-1}$	$10^{-2}$	$10^{-4}$	$10^{-8}$
$\eta_{\text{upp},(i)}^\pm$	1.028	1.028	1.028	1.028	1.028
$\eta_{\text{low},(i)}^\pm$	0.838	0.837	0.837	0.837	0.837
$\xi_{(i)}^\pm$	0.997	0.998	0.998	0.998	0.998

Table 3.14: Effectivity indices of upper and lower bounds to the terms coming from the polarization formula expansion (3.16), for a periodically layered material and a radial frequency of 4000 Hz.

$\beta^*$	$10^0$	$10^{-1}$	$10^{-2}$	$10^{-4}$	$10^{-8}$
$\frac{ \hat{\mathcal{Q}}(\hat{\mathbf{e}}_0) }{ \hat{\mathcal{Q}}(\hat{\mathbf{u}}) }$	0.425(1)	0.738(0)	0.414(0)	0.409(0)	0.409(0)
$\gamma^*$	0.999	1.197	1.366	1.372	1.372
$\gamma_{\text{upp}}$	14.219	18.225	20.826	20.906	20.906
$\gamma_{\text{est}}$	0.921	2.072	2.505	2.516	2.516

Table 3.15: Relative error and effectivity indices of the modeling error estimators, for a periodically layered material and a radial frequency of 4000 Hz.

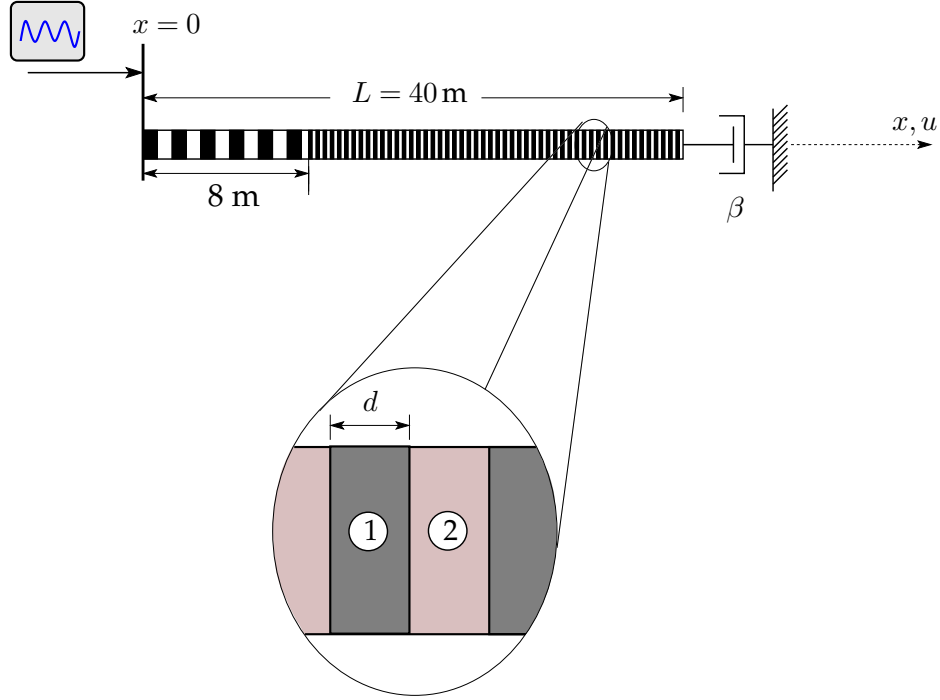


Figure 3.6: Steady state problem for a non-uniformly layered material.

### 3.6.3 Steady State Case III: a Non-Uniformly Layered Material

In the previous examples, the material of the beam has a periodic microstructure. In this section, the more interesting nonperiodic case is analyzed. Consider the problem configuration illustrated in Figure 3.6: the beam is constructed of a carbon-epoxy composite material (see Section 3.6.1 for material properties), but now there are two different zones with different layer thicknesses. In the first zone, between  $x = 0$  to  $x = 8$ , the layers have thickness  $d = 0.5$  m, whereas in the remaining part of the beam,  $d = 0.05$  m. Thus, between the two zones, the layer thicknesses differ a factor 10 and there should be different dispersion sensitivities because of this scale difference. In the first zone, dispersion should be an issue at lower frequencies.

A damping boundary condition at the right edge of the beam ( $\beta = \sqrt{E(L)\rho(L)}$ ) is applied as before, but now a nonhomogeneous Dirichlet boundary condition is imposed at the left edge, where  $\hat{\mathbf{u}}(0) = 0.1$ . The source terms in the RHS of (2.4) are all identically zero (no initial displacement or velocity field). For a given frequency  $\omega$ , the physical interpretation of this problem would be that if the edge at  $x = 0$  is driven with this frequency  $\omega$ , the steady state solution of this beam is given by  $\mathbf{u}(x, t) = \mathcal{R}e \{ \hat{\mathbf{u}}(x, \omega) e^{i\omega t} \}$ . The quantity of interest for this numerical example is the average stress on a small domain  $S$  that is bordering with the right edge of the beam:  $S = (39, 40)$ . Thus,

$$\hat{Q}(\hat{\mathbf{u}}) = \int_{x=39}^{x=40} \left( E \frac{d\hat{\mathbf{u}}}{dx} \right) dx.$$

An overkill solution is computed by using approximately 800 quadratic elements to compute the solution pairs  $(\hat{\mathbf{u}}, \hat{\mathbf{p}})$  and  $(\hat{\mathbf{u}}_0, \hat{\mathbf{p}}_0)$  to (3.2) and (3.4), respectively. Again,

the approximate material model is determined by applying an asymptotic homogenization technique and the resulting values are:

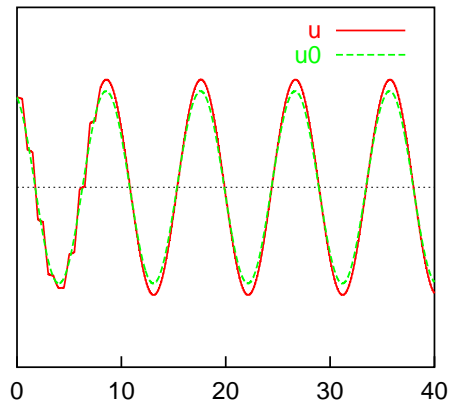
$$E_0 = 11.4 \text{ GPa}, \quad \rho_0 = 5.5 \text{ g/cm}^3.$$

In Figures 3.7 through 3.10, the solutions  $(\hat{\mathbf{u}}, \hat{\mathbf{p}})$  and  $(\hat{\mathbf{u}}_0, \hat{\mathbf{p}}_0)$  are shown for radial frequencies  $\omega$  of 1000, 2000, 3000, and 4000 Hz. In these figures, the fine scale solutions  $(\hat{\mathbf{u}}, \hat{\mathbf{p}})$  are plotted as solid red lines and the coarse scale solutions  $(\hat{\mathbf{u}}_0, \hat{\mathbf{p}}_0)$  as green dashed green lines. For  $\omega = 1000$  and 2000 Hz, the wave lengths are significantly larger than the dimensions of the inhomogeneity in the material. Apart from a small perturbation in the left zone, the exact solution  $\hat{\mathbf{u}}$  acts as if it is propagating through a homogeneous material. Analogous to the results for the low frequencies in Section 3.6.1, the modeling error is caused by the mismatch in  $E$  and  $E_0$ . For  $\omega = 3000$  Hz (see Figure 3.9), the wave length has reached such a dimension that it is greatly disturbed by the layers in the left zone of the beam. Not only an amplitude mismatch with the homogenized solution is noticeable, but also a small phase difference. Whenever the wave reaches the remainder of the beam, where the dimension of the inhomogeneity is much smaller, its wavelength is too large to effectively notice the inhomogeneity and propagates as if in homogeneous media. It is clear that the dispersion, created by passing through the left zone causes a significant contribution to the error in the average stress in the domain of interest. This example illustrates the global character of the wave problem. The accuracy of the solution in  $S$  for this frequency is very dependent on the material features at the other end of the domain in the left zone.

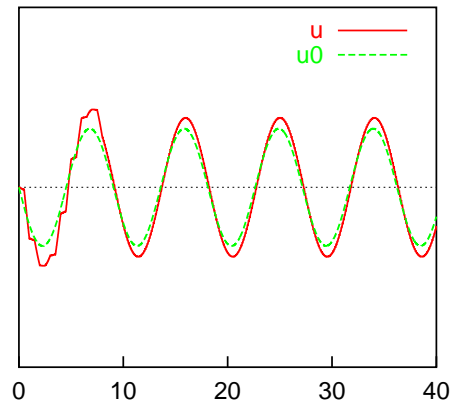
In Figure 3.10, the solutions for  $\omega = 4000$  Hz are presented and here the wave length has reached a dimension such that it is greatly affected by the inhomogeneity and attenuates dramatically as it propagates through the left zone. The frequency for this wave is within one of the so-called *stop-bands* [3, 4] of this inhomogeneity. The solutions for the dual solution show similar behavior: for low frequencies there is again an amplitude mismatch between  $\hat{\mathbf{p}}$  and  $\hat{\mathbf{p}}_0$  (see Section 3.6.1), but they are identical in phase. For higher frequencies, we again notice a slight difference in phase between  $\hat{\mathbf{p}}$  and  $\hat{\mathbf{p}}_0$ .

For the set of radial frequencies  $\omega$  of 1000, 2000, 3000, and 4000 Hz, Table 3.16 lists the effectivity indices for the global bounds of Lemma 3.5.1. The first four rows present the effectivity indices with respect to the global error norms  $\|\hat{\mathbf{e}}_1\|_{\mathcal{H}}$  and  $\|\hat{\varepsilon}_1\|_{\mathcal{H}}$ . Again, the upper bounds  $\zeta_{\text{upp}}$  and  $\bar{\zeta}_{\text{upp}}$  have good effectivity indices, close to 1. As  $\omega$  increases, the accuracy deteriorates slightly around 2%. For  $\zeta_{\text{low}}$  and  $\bar{\zeta}_{\text{low}}$ , the effectivity indices are poorer, close to 0.88 and the accuracy diminishes slightly, but still within 1%. The lower part in Table 3.16 shows the accuracy with respect to the global error norms  $\|\hat{\mathbf{e}}_0\|_{\mathcal{H}}$  and  $\|\hat{\varepsilon}_0\|_{\mathcal{H}}$ . It is clear that the global norms of the elliptic representations  $(\hat{\mathbf{e}}_1, \hat{\varepsilon}_1)$  are very close to the actual error norms when the frequency is low, but deviate as the frequency increases. Due to this effect,  $\zeta_{\text{upp}}$  and  $\bar{\zeta}_{\text{upp}}$  are very accurate estimators of  $\|\hat{\mathbf{e}}_0\|_{\mathcal{H}}$  and  $\|\hat{\varepsilon}_0\|_{\mathcal{H}}$  for lower frequencies, but the corresponding accuracies deteriorate approximately 15% as  $\omega$  reaches 4000 Hz. A similar result is observed for  $\zeta_{\text{low}}$  and  $\bar{\zeta}_{\text{low}}$ : at  $\omega = 4000$  Hz their effectivity indices have reached a level of approximately 0.73.

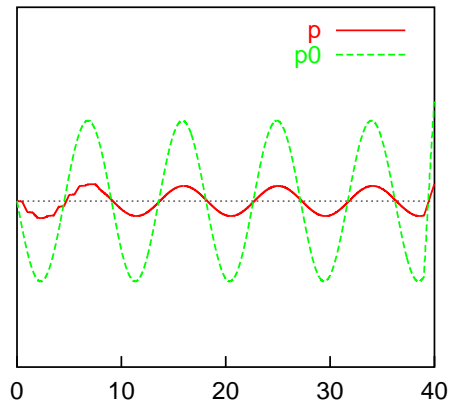
In Table 3.17, the effectivity indices for the upper and lower bounds  $\eta_{\text{upp}(i)}^{\pm}$  and  $\eta_{\text{low}(i)}^{\pm}$  of Lemma 3.4.1 are presented. The upper bounds are very accurate estimators for the low frequencies, within 2.0%, and lose 2% accuracy as  $\omega$  increases. Again, the



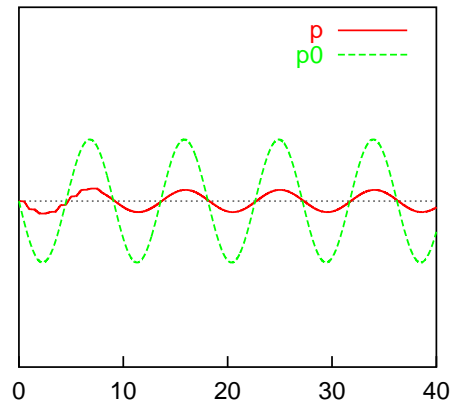
(a) Real part primal solution.



(b) Imaginary part primal solution.

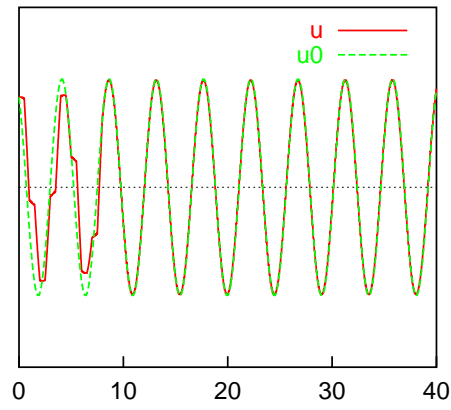


(c) Real part dual solution.

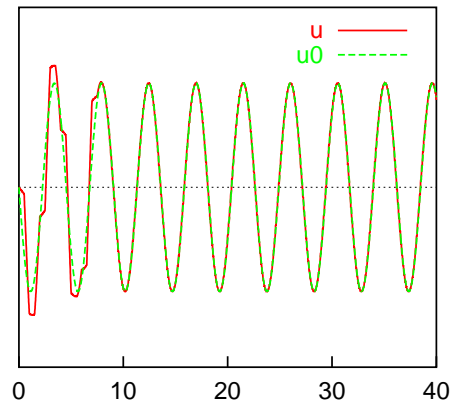


(d) Imaginary part dual solution.

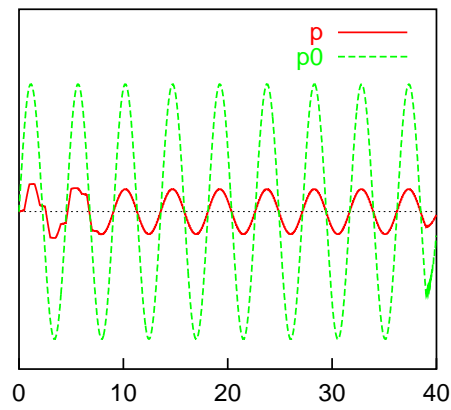
Figure 3.7: Steady state solutions of a non-uniformly layered material for a radial frequency of 1000 Hz, normalized by  $\|\hat{\mathbf{u}}_0\|_{L^\infty(\Omega)}$  and  $\|\hat{\mathbf{p}}_0\|_{L^\infty(\Omega)}$ .



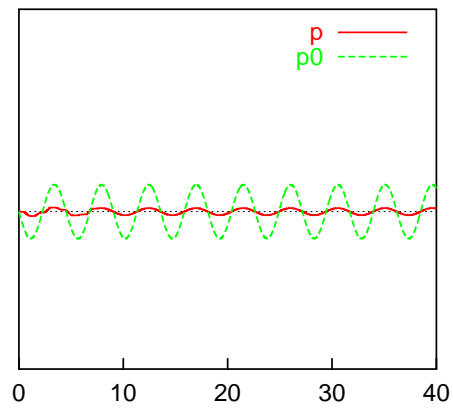
(a) Real part primal solution.



(b) Imaginary part primal solution.

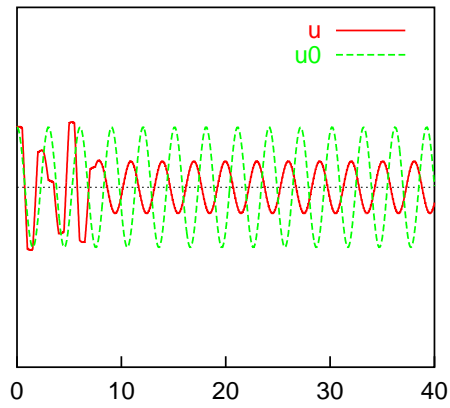


(c) Real part dual solution.

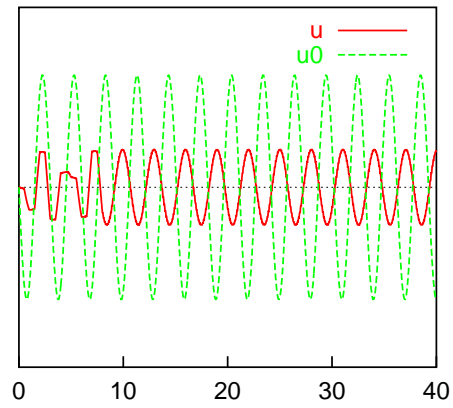


(d) Imaginary part dual solution.

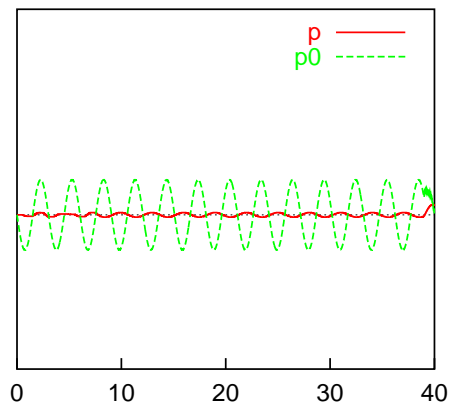
Figure 3.8: Steady state solutions of a non-uniformly layered material for a radial frequency of 2000 Hz, normalized by  $\|\hat{\mathbf{u}}_0\|_{L^\infty(\Omega)}$  and  $\|\hat{\mathbf{p}}_0\|_{L^\infty(\Omega)}$ .



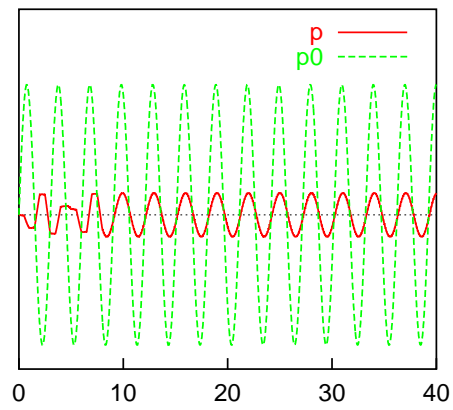
(a) Real part primal solution.



(b) Imaginary part primal solution.

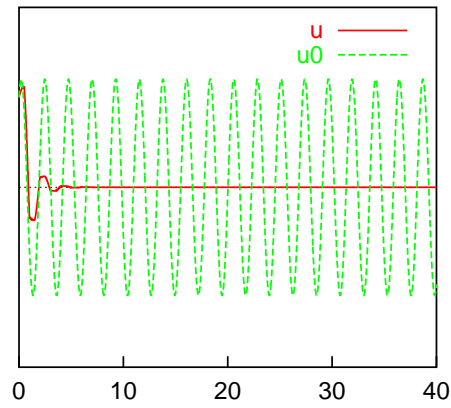


(c) Real part dual solution.

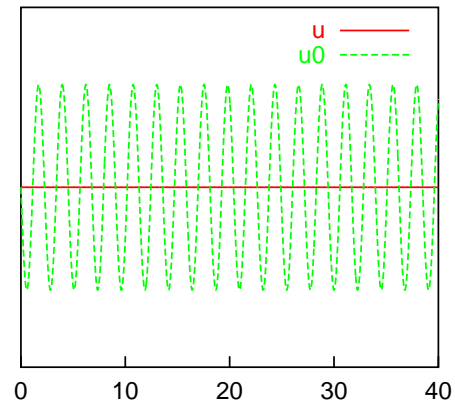


(d) Imaginary part dual solution.

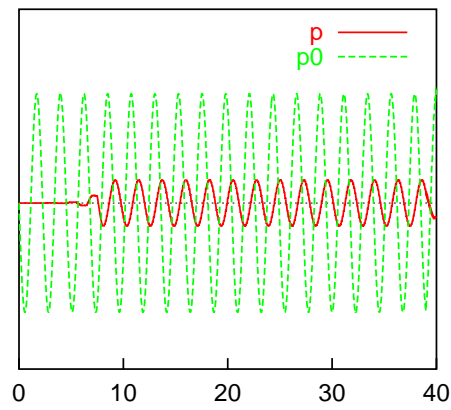
Figure 3.9: Steady state solutions of a non-uniformly layered material for a radial frequency of 3000 Hz, normalized by  $\|\hat{\mathbf{u}}_0\|_{L^\infty(\Omega)}$  and  $\|\hat{\mathbf{p}}_0\|_{L^\infty(\Omega)}$ .



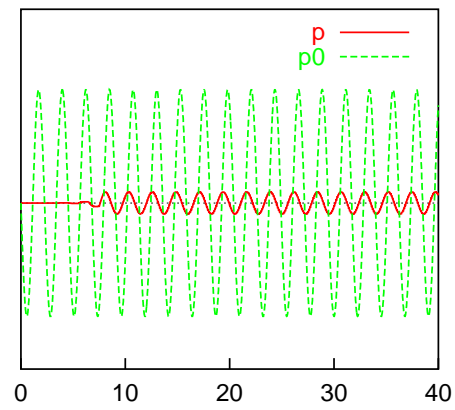
(a) Real part primal solution.



(b) Imaginary part primal solution.



(c) Real part dual solution.



(d) Imaginary part dual solution.

Figure 3.10: Steady state solutions of a non-uniformly layered material for a radial frequency of 4000 Hz, normalized by  $\|\hat{\mathbf{u}}_0\|_{L^\infty(\Omega)}$  and  $\|\hat{\mathbf{p}}_0\|_{L^\infty(\Omega)}$ .

$\omega$ (Hz)	1000	2000	3000	4000
$\zeta_{\text{upp}}$	1.027	1.028	1.029	1.030
$\zeta_{\text{low}}$	0.880	0.881	0.882	0.882
$\bar{\zeta}_{\text{upp}}$	1.016	1.027	1.029	1.031
$\bar{\zeta}_{\text{low}}$	0.891	0.883	0.882	0.884
$\ \hat{\mathbf{e}}_1\ _{\mathcal{H}}$	0.993	0.990	0.760	0.833
$\ \hat{\varepsilon}_1\ _{\mathcal{H}}$	0.928	0.882	0.858	0.826
$\zeta_{\text{upp}}$	1.021	1.018	0.782	0.859
$\zeta_{\text{low}}$	0.875	0.872	0.670	0.736
$\bar{\zeta}_{\text{upp}}$	0.943	0.906	0.884	0.852
$\bar{\zeta}_{\text{low}}$	0.828	0.779	0.758	0.730

Table 3.16: Effectivity indices with respect to  $\|\hat{\mathbf{e}}_1\|_{\mathcal{H}}$  and  $\|\hat{\varepsilon}_1\|_{\mathcal{H}}$  (upper part), and  $\|\hat{\mathbf{e}}_0\|_{\mathcal{H}}$  and  $\|\hat{\varepsilon}_0\|_{\mathcal{H}}$  (lower part) for a non-uniformly layered material.

$\omega$ (Hz)	1000	2000	3000	4000
$\eta_{\text{upp},(i)}^{\pm}$	1.016	1.027	1.029	1.031
$\eta_{\text{low},(i)}^{\pm}$	0.913	0.844	0.838	0.840
$\xi_{(i)}^{\pm}$	1.000	0.999	1.000	1.001

Table 3.17: Effectivity indices of upper and lower bounds to the terms coming from the polarization formula expansion (3.16), for a non-uniformly layered material.

lower bounds have poorer effectivity indices than the upper bounds, and in addition lose about 5% accuracy as  $\omega$  increases. The effectivity indices for the estimators  $\xi_{(i)}^{\pm}$  once again distinguish themselves by both good effectivity indices, close to 1, and a very small sensitivity to the frequencies.

This directly affects the accuracy of the estimator  $\gamma_{\text{est}}$ . In Table 3.18, one can see that it maintains good accuracy for all the frequencies, with effectivity indices ranging from approximately 1, for low frequencies, up to 2.3 for high frequencies. The slight decrease in accuracy is caused by the accuracy of the intermediate estimator  $\gamma^*$ . This estimator is obtained by ignoring  $\mathcal{C}(\hat{\mathbf{e}}_0, \hat{\mathbf{e}}_1)$  (see (3.14) and (3.15)), which represents an inertial feature within the error. For higher frequencies, this term becomes more influential. However, the effectivity indices show that the accuracy is not dramatically affected by eliminating this term.

The estimators  $\gamma_{\text{avg}}$  and  $\gamma_{\text{low}}$  again represent poor estimates and their accuracy deteriorates even further as the frequency increases. The estimator  $\gamma_{\text{upp}}$  shows a reasonable accuracy for low frequencies.

$\omega$ (Hz)	1000	2000	3000	4000
$ \hat{\mathcal{Q}}(\hat{\mathbf{e}}_0)/\hat{\mathcal{Q}}(\hat{\mathbf{u}}) $	0.395(1)	0.471(1)	0.169(2)	0.265(5)
$\gamma^*$	0.840	1.021	2.649	3.401
$\gamma_{\text{upp}}$	3.709	11.146	17.756	17.945
$\gamma_{\text{low}}$	17.104	60.907	101.469	101.419
$\gamma_{\text{avg}}$	6.779	24.899	41.879	41.763
$\gamma_{\text{est}}$	0.789	1.176	2.202	2.338

Table 3.18: Relative error and effectivity indices of the modeling error estimators, for a non-uniformly layered material.

### 3.6.4 Transient Test Problem

In this section, we present an illustrative example of how the results from the previous steady state cases can be applied to analyze transient problems. We consider the carbon-epoxy composite beam, as shown in Figure 3.11. The material microstructure is periodic uniformly throughout the beam, where the carbon layers have thickness  $d = 0.05$  m, and the epoxy layers have thickness  $d = 0.15$  m. Again, damping boundary conditions are prescribed at the right edge of the beam and homogeneous Dirichlet boundary conditions at the left edge. At  $t = 0$  s, the velocity field is identically zero, *i.e.*  $\mathbf{V}_0(x) = 0$ , and the initial displacement field  $\mathbf{U}_0(x)$  is prescribed by the pulse function in (3.31) with width  $\delta = 0.2$  m.

Now, the solutions  $\mathbf{u}(x, t)$  and  $\mathbf{u}_0(x, t)$  are computed for  $0 \leq t < 0.05$  s, by using an overkill discretization of the frequency spectrum of 60 frequencies. For each of these frequencies, (3.2) and (3.4) are solved by using an overkill mesh of 800 quadratic elements. The solutions in time are subsequently computed by applying a discrete inverse Fourier transformation.

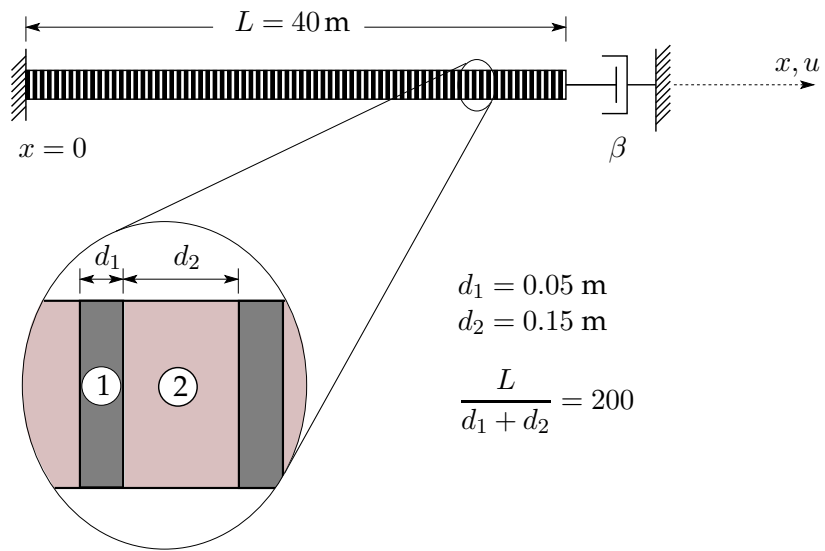
For this specific example, the quantity of interest is the average stress on the small subdomain  $S = (24, 25)$ . The approximate homogenized material properties are found to be equal to:

$$E_0 = 7.8 \text{ GPa}, \quad \rho_0 = 4.2 \text{ g/cm}^3.$$

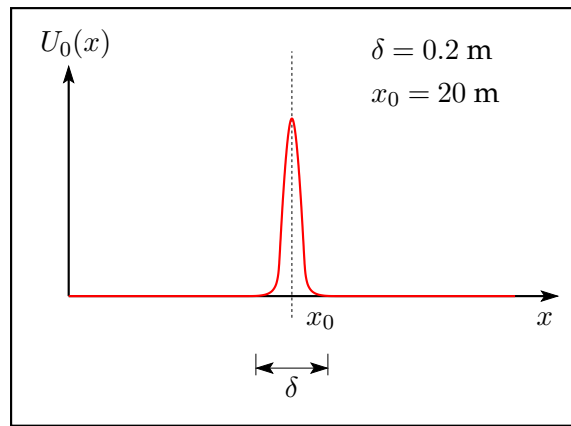
In Figure 3.12, the solutions in time are plotted for six consecutive time steps. The fine scale solution  $\mathbf{u}(x, t)$  is plotted as a solid red line and the coarse scale solution  $\mathbf{u}_0(x, t)$  as a green dashed line. Figure 3.12a, shows two major waves at  $t = 5$  ms for both solutions: one that propagates toward the left edge and one toward the right edge. In Figure 3.12b, the left-advancing waves reach the clamped edge and are about to be reflected, whereas the the other waves are damped at the right edge. The four following graphs show the reflected waves propagating toward the right edge of the beam. For the later time steps  $t = 25, 30,$  and  $35$  ms, the dispersion effect is very noticeable. Compared to the homogenized solution, the initial peak of the fine scale solution  $\mathbf{u}(x, t)$  is considerably smaller. Also, the presence of the trailing waves for  $\mathbf{u}(x, t)$  becomes apparent. These waves are much larger in amplitude than the minor waves following the initial pulse of the homogenized solution  $\mathbf{u}_0(x, t)$ .

Figure 3.13 shows the solutions in time for the stresses. Again, the stress for the fine-scale problem,  $\sigma(x, t) = E(x) \frac{\partial \mathbf{u}(x, t)}{\partial x}$ , is drawn as a solid red line, whereas the stress for the coarse scale problem,  $\sigma_0(x, t) = E_0 \frac{\partial \mathbf{u}_0(x, t)}{\partial x}$ , is drawn as a dashed green line. The solutions are shown for a set of time steps where the reflected waves are passing through the domain  $20 < x < 30$  m. The domain of interest  $S = (24, 25)$  is indicated in these graphs as well. A behavior similar to the previous figure is observed: due to the dispersion effect, the amplitudes of the fine-scale solution differ significantly, and the response is trailing behind with the homogenized solution. Clearly, for this example, a material model based on homogenized material properties does not suffice to describe the wave problem accurately.

Having computed  $\hat{Q}(\hat{\mathbf{e}}_0)$ ,  $\gamma^*$ , and  $\gamma_{est}$ ; the upper bounds on these quantities in the time period  $t \in [0, 0.05]$  can be computed. This is illustrated on a simple example of an arbitrary function  $f(x, t)$  for which the Fourier transform  $\hat{f}(x, \omega)$  is known at a set



(a) Problem configuration.



(b) Initial displacement field

Figure 3.11: Transient test problem with initial displacement field.

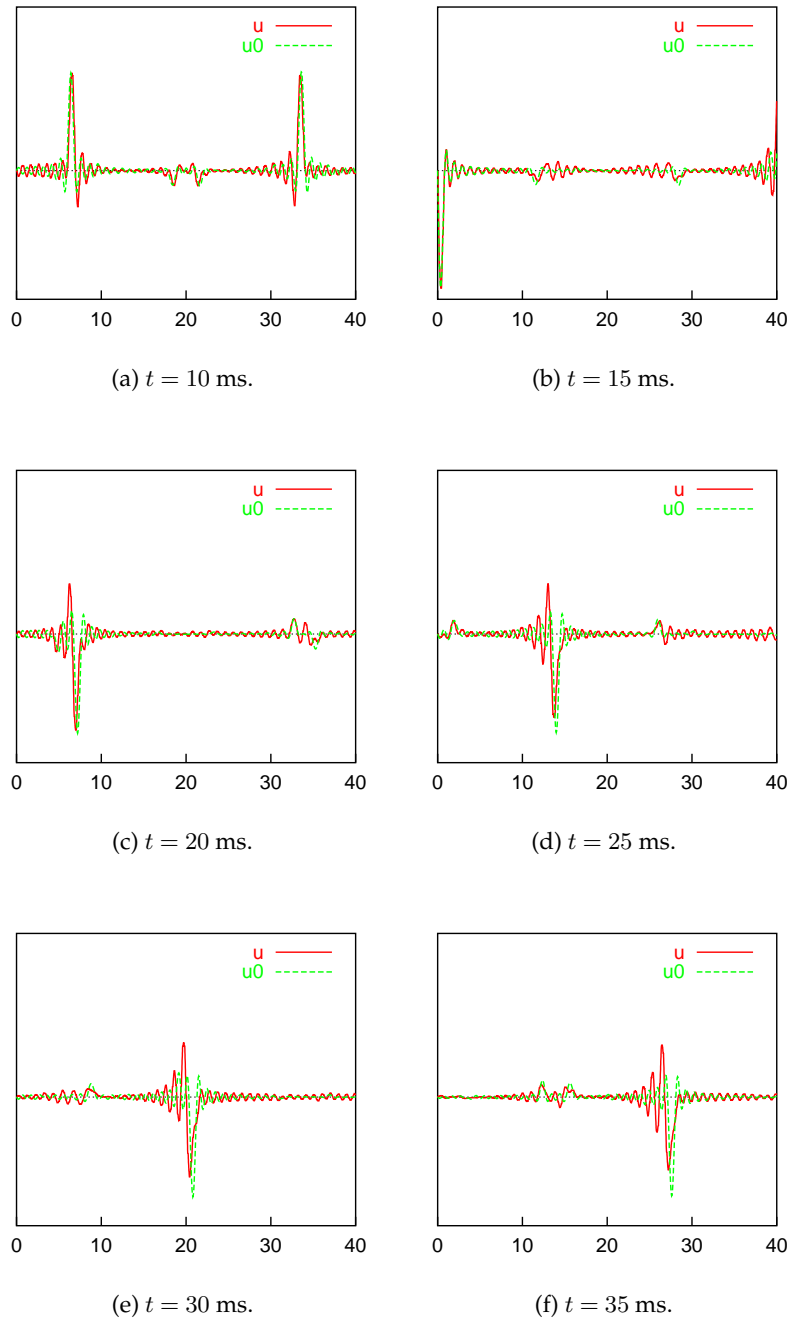


Figure 3.12: Transient solutions due to an initial pulse at  $x = 20$  m with width  $\delta = 0.2$  m, normalized by the maximum displacement  $|\mathbf{u}_0(x, t)|$ ,  $x \in \Omega$ ,  $t \in [0, 0.05]$ .

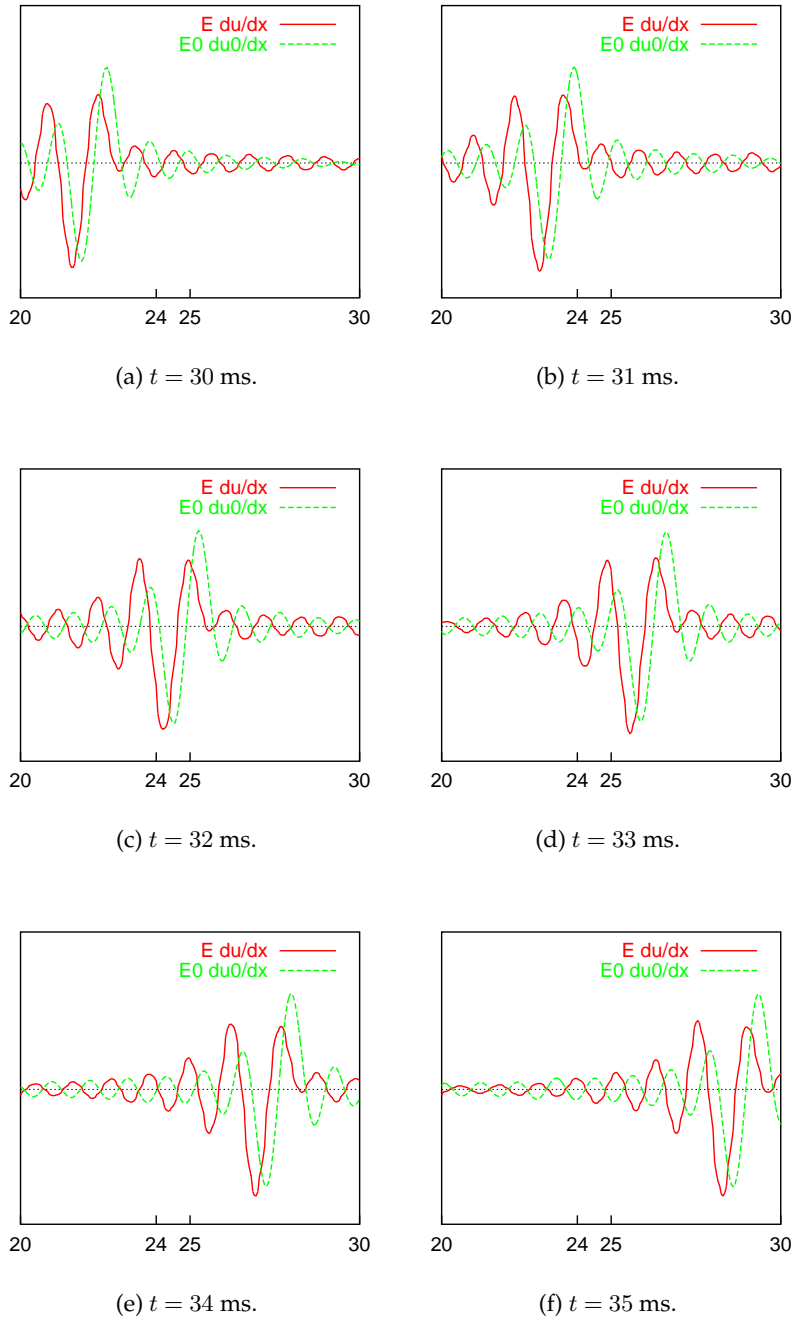


Figure 3.13: Transient solutions for the stresses in the domain of interest, normalized by the maximum stress  $|E_0 \frac{d\mathbf{u}_0}{dx}(x, t)|$ ,  $x \in \Omega$ ,  $t \in [0, 0.05]$ .

of frequencies  $\omega_n$ , such that:

$$\omega_n = \frac{2\pi n}{T}, \quad n \leq N,$$

$t \in [0, T]$ . The discrete inverse Fourier transform is [3]:

$$\begin{aligned} f(x, t) &= \frac{1}{T} \left[ \mathcal{R}e \left\{ \hat{f}(x, 0) \right\} + 2\mathcal{R}e \left\{ \sum_{n=1}^N \hat{f}(x, \omega_n) e^{i\omega_n t} \right\} \right] \\ &= \frac{1}{T} \left[ \mathcal{R}e \left\{ \hat{f}(x, 0) \right\} + 2 \sum_{n=1}^N \left( \mathcal{R}e \left\{ \hat{f}(x, \omega_n) \right\} \cos(\omega_n t) \right. \right. \\ &\quad \left. \left. - \mathcal{I}m \left\{ \hat{f}(x, \omega_n) \right\} \sin(\omega_n t) \right) \right]. \end{aligned} \quad (3.32)$$

By applying the triangle inequality, we an upper bound on  $f(x, t)$  is obtained for the time-period  $[0, T]$ :

$$|f(x, t)| \leq \frac{1}{T} \left[ \left| \mathcal{R}e \left\{ \hat{f}(x, 0) \right\} \right| + 2 \sum_{n=1}^N \left( \left| \mathcal{R}e \left\{ \hat{f}(x, \omega_n) \right\} \right| + \left| \mathcal{I}m \left\{ \hat{f}(x, \omega_n) \right\} \right| \right) \right]. \quad (3.33)$$

If this equation is used to compare the results computed for  $\hat{Q}(\hat{\mathbf{e}}_0)$ ,  $\gamma^*$ , and  $\gamma_{\text{est}}$ , then upper bounds of these quantities in time are obtained. In Table 3.19, these bounds and the corresponding effectivity indices are listed. The value for  $\gamma_{\text{est}}$  is pushed away from 1.0 to approximately 2.4 due to the higher effectivity indices for the high frequencies (see also the steady state results in Section 3.6.1). This effectivity index still suffices to use  $\gamma_{\text{est}}$  to assess the modeling error in the average stress with reasonable accuracy, or within the right order. Note that the bound on  $Q(\mathbf{e}_0)$  is approximately 3.7 times higher than the bound on  $Q(\mathbf{u})$ .

	Bound (GPa)	Effectivity Index
$Q(\mathbf{e}_0)$	7.51	
$\gamma^*$	7.31	0.97
$\gamma_{\text{est}}$	18.0	2.39

Table 3.19: Bounds on the modeling error and error estimators for the transient test problem, for  $t = [0, 0.05]$  s.

# 4 Adaptive Modeling of the Wave Problem

The concept of goal-oriented adaptive modeling was introduced by Oden and Vemaganti [19, 20, 26, 27] for the analysis of problems in elastostatics. The basic philosophy of this concept is to develop a mathematical model or description out of a hierarchy of available models, to describe the occurrence of a physical event to within a preset solution accuracy.

In this chapter, this approach is extended to the engineering problem of wave propagation in heterogeneous materials. In this case, the applications are restricted to situations in which the goal is the average stress in a small subdomain in the elastic body. In Section 4.2, an adaptive algorithm is proposed for the development of the material model to control the modeling error. The algorithm employs *error indicators* to decide where in the material model the adaptation should be implemented. These error indicators are derived in Section 4.1. Finally, in Section 4.3, the application of the adaptive modeling algorithm is demonstrated for a set of one-dimensional examples.

## 4.1 Modeling Error Indicators

Recalling (3.15) and applying the triangle and Schwarz inequalities, one obtains the following:

$$|\gamma^*| \leq |\mathcal{R}(\hat{\mathbf{u}}_0, \hat{\mathbf{p}}_0)| + \|\hat{\mathbf{e}}_1\|_{\mathcal{H}} \|\hat{\mathbf{e}}_1\|_{\mathcal{H}}.$$

By applying Lemma 3.5.1 on the norms in the RHS, gives:

$$|\gamma^*| \leq |\mathcal{R}(\hat{\mathbf{u}}_0, \hat{\mathbf{p}}_0)| + \zeta_{\text{upp}} \bar{\zeta}_{\text{upp}}. \quad (4.1)$$

Now, let the subdomain partition  $\{\Theta_k\}$  of  $\Omega$  be defined as follows:

$$\Omega = \text{int} \left( \bigcup_{k=1}^M \overline{\Theta_k} \right), \quad \Theta_i \cap \Theta_j = \emptyset, \quad \forall i \neq j. \quad (4.2)$$

Then (4.1) suggests that the restrictions to  $\{\Theta_k\}$  of each of the terms in the RHS give an indication of the contribution of the subdomains to  $|\gamma^*|$ . Since  $\gamma^*$  forms a reliable estimate of the modeling error (see Section 3.6), these indicators can be extrapolated

to estimating the modeling error itself. Thus, the following quantities  $\{\mathcal{E}_k\}$ , defined on  $\{\Theta_k\}$ , are proposed as error indicators of the modeling error:

$$\boxed{\mathcal{E}_k = |\mathcal{R}_k(\hat{\mathbf{u}}_0, \hat{\mathbf{p}}_0)| + \zeta_k \bar{\zeta}_k}, \quad (4.3)$$

where

$$\begin{aligned} \mathcal{R}_k(\hat{\mathbf{u}}_0, \hat{\mathbf{p}}_0) &= \int_{\Theta_k} \{ \mathbf{E} \mathcal{I}_0 \nabla \hat{\mathbf{u}}_0 \cdot \overline{\nabla \hat{\mathbf{p}}_0} - \rho \omega^2 j_0 \hat{\mathbf{u}}_0 \cdot \overline{\hat{\mathbf{p}}_0} \} \, \mathbf{d}\mathbf{x}, \\ \zeta_k &= \sqrt{\int_{\Theta_k} \{ \mathbf{E} \mathcal{I}_0 \nabla \hat{\mathbf{u}}_0 \cdot \overline{\mathcal{I}_0 \nabla \hat{\mathbf{u}}_0} + \rho \omega^2 j_0 \hat{\mathbf{u}}_0 \cdot \overline{j_0 \hat{\mathbf{u}}_0} \} \, \mathbf{d}\mathbf{x}}, \\ \bar{\zeta}_k &= \sqrt{\int_{\Theta_k} \{ \mathbf{E} \mathcal{I}_0 \nabla \hat{\mathbf{p}}_0 \cdot \overline{\mathcal{I}_0 \nabla \hat{\mathbf{p}}_0} + \rho \omega^2 j_0 \hat{\mathbf{p}}_0 \cdot \overline{j_0 \hat{\mathbf{p}}_0} \} \, \mathbf{d}\mathbf{x}}, \end{aligned}$$

where the deviation tensor  $\mathcal{I}_0$  and function  $j_0$  are given in (3.8).

## 4.2 The Adaptive Algorithm

In this section, a detailed description of the adaptive modeling algorithm, proposed for the analysis of wave propagation through heterogeneous materials, is given. The occurrence of geometric dispersion [3, 4] is a major complication in modeling elastic wave propagation. Contrary to the elastostatic case, the sensitivity of the solutions is very global, as the numerical examples in Section 3.6 show.

Since dispersion is determined by the ratio between the wave-length and the dimension of the inhomogeneity, it follows directly that there is a great dependence on the wave frequency. Therefore, the choice for a frequency domain analysis seems to be reasonable. The basic idea is that by decomposing the wave into a spectrum of steady state waves with frequency  $\omega$ , those frequencies are identified that are sensitive to the material inhomogeneity. Subsequently, the adaptation of the material model can be applied for these frequencies.

In the following, a step by step account of the adaptive modeling algorithm is given, which is illustrated schematically in Figure 4.1:

*Step 1.* The domain  $\Omega$  is partitioned into subdomains  $\{\Theta_k\}$ , as given by (4.2), where one of the subdomains is  $S$ , the area on which the quantity of interest is defined (see (3.1)). The set  $\{\Theta_k\}$  is chosen such that each subdomain  $k$  contains inhomogeneities of similar dimensions.

In this study, the coarse model  $\{E_0, \rho_0\}$ , is chosen as the homogenized (constant) material properties that are obtained by applying a classical homogenization technique [23]. In general applications, the user has the freedom to choose any abstract approximate material to start the algorithm.

*Step 2.* The wave problem is decomposed into a set of steady state waves, with frequencies  $\{\omega_n\}$ , where  $n = 1, 2, \dots, N$ . For the analysis of one steady state wave, of course  $N = 1$ , whereas for a wave with a discrete frequency spectrum we have  $N \geq 1$ . For the analysis of transient waves with continuous frequency spectra,

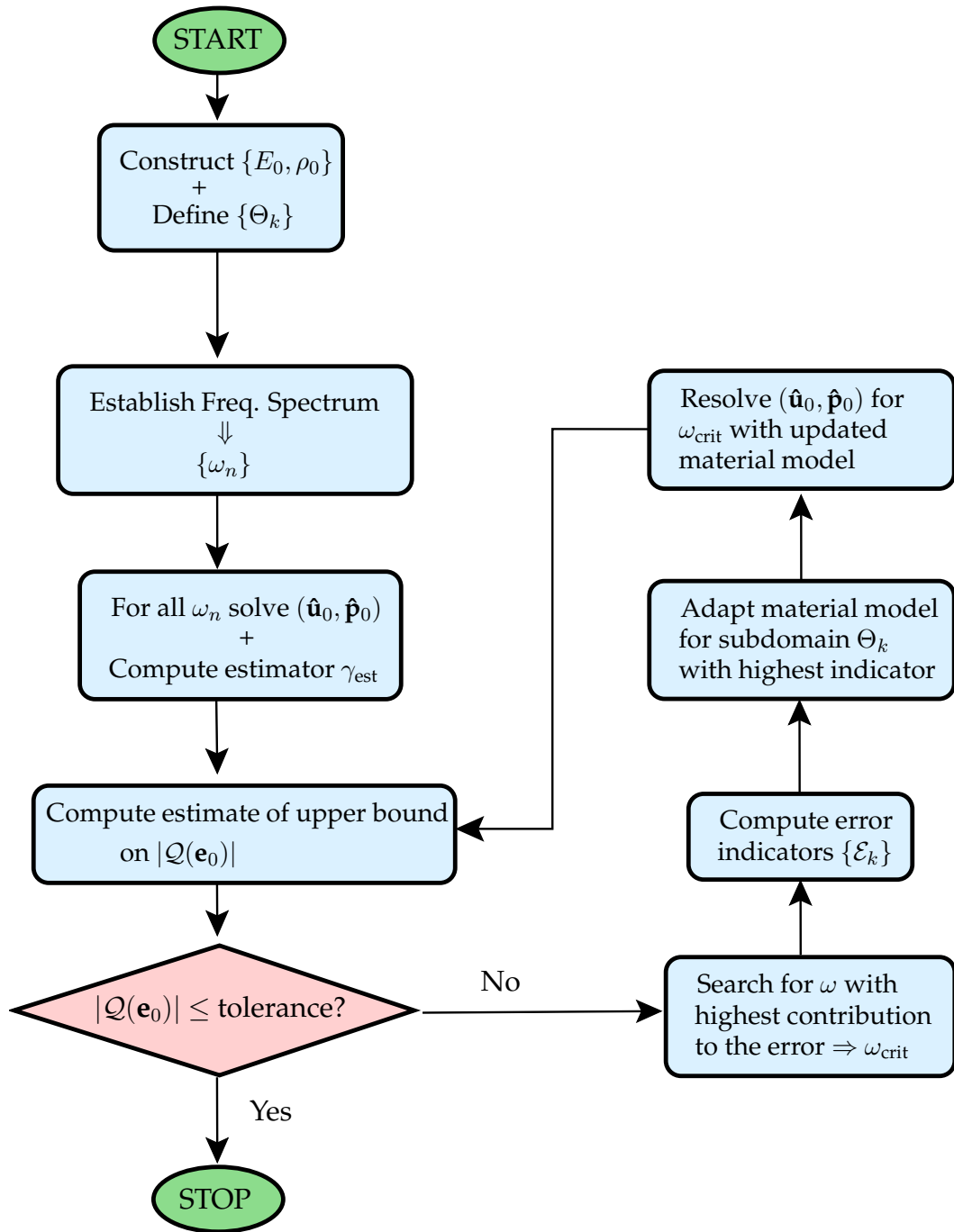


Figure 4.1: Flow diagram of the adaptive modeling algorithm.

an overkill discretization of the frequency spectrum is used. The overkill discretization is assumed to deliver the desired accuracy.

- Step 3.* For every frequency  $\omega_n$ , the solution pair  $(\hat{\mathbf{u}}_0, \hat{\mathbf{p}}_0)$  to (3.4) is computed. Since the numerical experiments in Section 3.6 show that the estimator  $\gamma_{\text{est}}$  (see Section 3.5.1) has highest accuracy, this estimator is chosen to assess the modeling error and, consequently, is computed for every frequency as well.
- Step 4.* By using the  $\{\gamma_{\text{est}}\}$  for all the frequencies, the upper bound in time on  $|\mathcal{Q}(\mathbf{e}_0)|$ , the error in the average stress on  $S$ , is computed by applying (3.33). In the case where  $N = 1$ , only  $|\gamma_{\text{est}}|$  needs to be computed.
- Step 5.* The estimate of the error bound is compared with a user-set tolerance. If the estimate exceeds the error tolerance, the analysis proceeds to *Step 6*, if not, the analysis **ends**.
- Step 6.* A search through the frequency spectrum is performed to identify the frequency  $\omega_{\text{crit}}$  that has the highest contribution to the error bound of *Step 4*.
- Step 7.* Subsequently, the error indicators  $\{\mathcal{E}_k\}$ , as given in (4.3), are computed for all the subdomains  $\{\Theta_k\}$ .
- Step 8.* Next, for  $\omega_{\text{crit}}$ , the material model is adapted in the subdomain  $\Theta_k$  that has the highest relative error indicator  $\frac{\mathcal{E}_k}{|\Theta_k|}$ . In this study, the adaptation implies the inclusion of the exact material properties  $\{E, \rho\}$  in  $\Theta_k$ . Of course, in general applications, one can choose different adaptation techniques, *e.g.* by using a hierarchy of material properties. It is emphasized that at the end of the process, the approximate material model is generally different for different frequencies.
- Step 9.* Finally, for  $\omega_{\text{crit}}$  only, the solution pair  $(\hat{\mathbf{u}}_0, \hat{\mathbf{p}}_0)$  to (3.4) is recomputed by employing the updated material model  $\{E_0(x), \rho_0(x)\}$ , and  $\gamma_{\text{est}}$  is recomputed for this frequency. Then *Step 5* is revisited.

## 4.3 Numerical Examples

In this section, a set of numerical examples is presented to demonstrate the application of the adaptive algorithm proposed in Section 4.2. The application to steady states wave of one frequency is given in Section 4.3.1, whereas Section 4.3.2 treats transient waves that are bandlimited.

### 4.3.1 Steady State Waves

The problem configuration considered is shown in Figure 4.2: a beam with 3 zones with different dimensions of inhomogeneity. As in Section 3.6, the material is made out of two constituents: carbon and epoxy (see Section 3.6 for material properties). The beam has a damping boundary condition at its right edge, and a nonhomogeneous Dirichlet boundary condition  $\hat{\mathbf{u}}(0) = 0.1$  at the left edge.

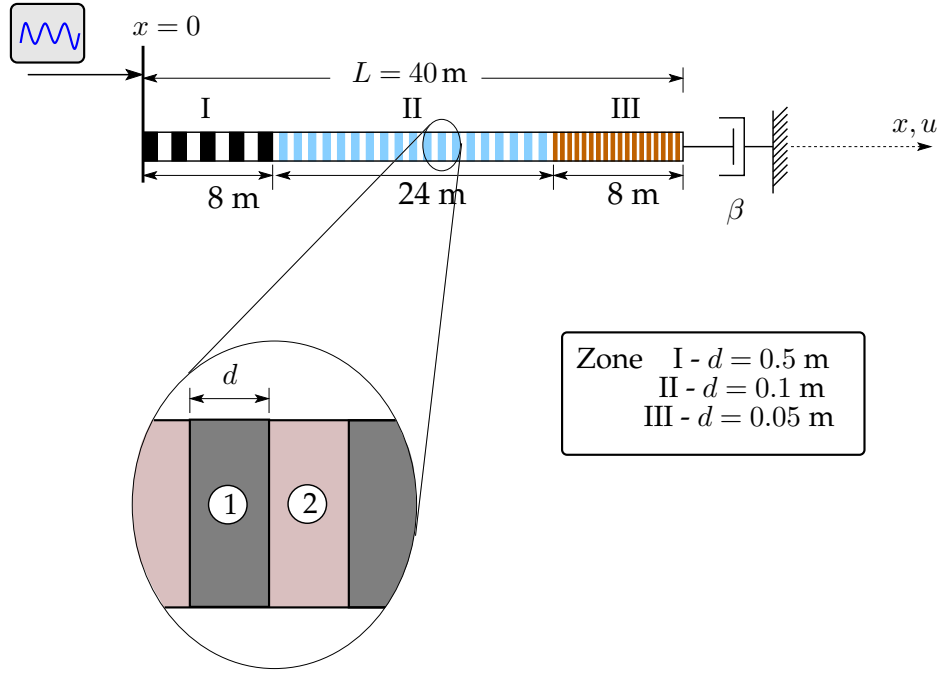


Figure 4.2: Steady state problem of a beam with 3 zones of inhomogeneities.

The beam is partitioned into 7 subdomains, such that:

$$\begin{aligned}
 \Theta_1 &= (0, 8), && \text{(contains zone I)} \\
 \Theta_2 &= (8, 16), && \text{(in zone II)} \\
 \Theta_3 &= (16, 24), && \text{(in zone II)} \\
 \Theta_4 &= (24, 32), && \text{(in zone II)} \\
 \Theta_5 &= (32, 36), && \text{(in zone III)} \\
 \Theta_6 &= (36.0, 36.1), && \text{(domain of interest)} \\
 \Theta_7 &= (36.1, 40). && \text{(in zone III)}
 \end{aligned}$$

The domain of interest  $S$ , on which the average stress is computed, is represented by  $\Theta_6$ . This small subdomain consists of only two layers and is a representative cell for the inhomogeneity in zone III. The approximate material properties at the beginning of the adaptive process,  $\{E_0, \rho_0\}$ , are obtained by applying the classical asymptotic homogenization technique and using the domain of interest  $S$  as the representative unit cell of the entire beam. Thus,

$$E_0 = 11.4 \text{ GPa}, \quad \rho_0 = 5.5 \text{ g/cm}^3.$$

The adaptive algorithm is first applied to the case in which the radial frequency is low, *i.e.*  $\omega = 200 \text{ Hz}$ . In Table 4.1 a data log is shown for every iteration step in the algorithm. It lists the relative error, the effectivity index for the estimator  $\gamma_{\text{est}}$ , and the list

of the distribution of the relative error indicators. The subdomain that has the highest relative error indicator is highlighted red and for the next iteration step, the material properties are adapted in these domains by taking the exact material properties (see Section 4.2). From the results for the relative errors, it is observed that the problem behavior is still rather local for this low frequency. A drop from a relative error of 4.5 to 0.03 is observed. This significant increase in accuracy is achieved by just including the exact material properties in the domain of interest. For iteration 1 and 3, it is observed that the effectivity index of  $\gamma_{\text{est}}$  exhibits good accuracy. However, for iteration 2, a poorer effectivity of approximately 3 is observed. This behavior is observed when the relative error drops below 10%. The effectivity indices range from 1 to 3 (though an effectivity index of 3 is rarely seen). This is due to the fact that, though the error is small, the estimator involves the difference between terms  $\|\hat{\mathbf{e}}_1 \pm (i)\varepsilon_1\|_{\mathcal{H}}$  (see (3.29)) that still remain very large. Since the accuracy of the estimates of these terms,  $\xi_{(i)}^{\pm}$ , does not improve proportionally (see also results in Tables 3.14 and 3.15), accuracy is lost in the overall estimator  $\gamma_{\text{est}}$ . Still, the estimator is of the right order. After iteration 3, the adaptive process is stopped, as a very high accuracy, of less than 1%, is achieved.

For the three iterations, Figure 4.3 shows the real and imaginary parts of the solutions, where the fine scale solution  $\hat{\mathbf{u}}$  is plotted as a solid red line and the approximate solution  $\hat{\mathbf{u}}_0$  as a green dashed green line. The graphs on the left show that the coarse material model for  $E_0$  (the profiles for  $\rho_0$  are similar) changes with each iteration step.

Iteration	$\frac{ \hat{Q}(\hat{\mathbf{e}}_0) }{ \hat{Q}(\hat{\mathbf{u}}) }$	$\frac{ \gamma_{\text{est}} }{ \hat{Q}(\hat{\mathbf{e}}_0) }$	Error Indicators $\frac{\mathcal{E}_k}{ \Theta_k }$
1	0.452(1)	0.98	1 - 0.910(9) 2 - 0.303(9) 3 - 0.704(9) 4 - 0.810(9) 5 - 0.208(9) 6 - 0.128(12) 7 - 0.200(9)
2	0.298(-1)	3.08	1 - 0.165(9) 2 - 0.548(8) 3 - 0.127(9) 4 - 0.147(9) 5 - 0.357(8) 7 - 0.368(8)
3	0.335(-2)	1.31	2 - 0.558(8) 3 - 0.128(9) 4 - 0.154(9) 5 - 0.386(8) 7 - 0.329(8)

Table 4.1: Data review of the adaptive modeling process for the steady state wave with a radial frequency of 200 Hz.

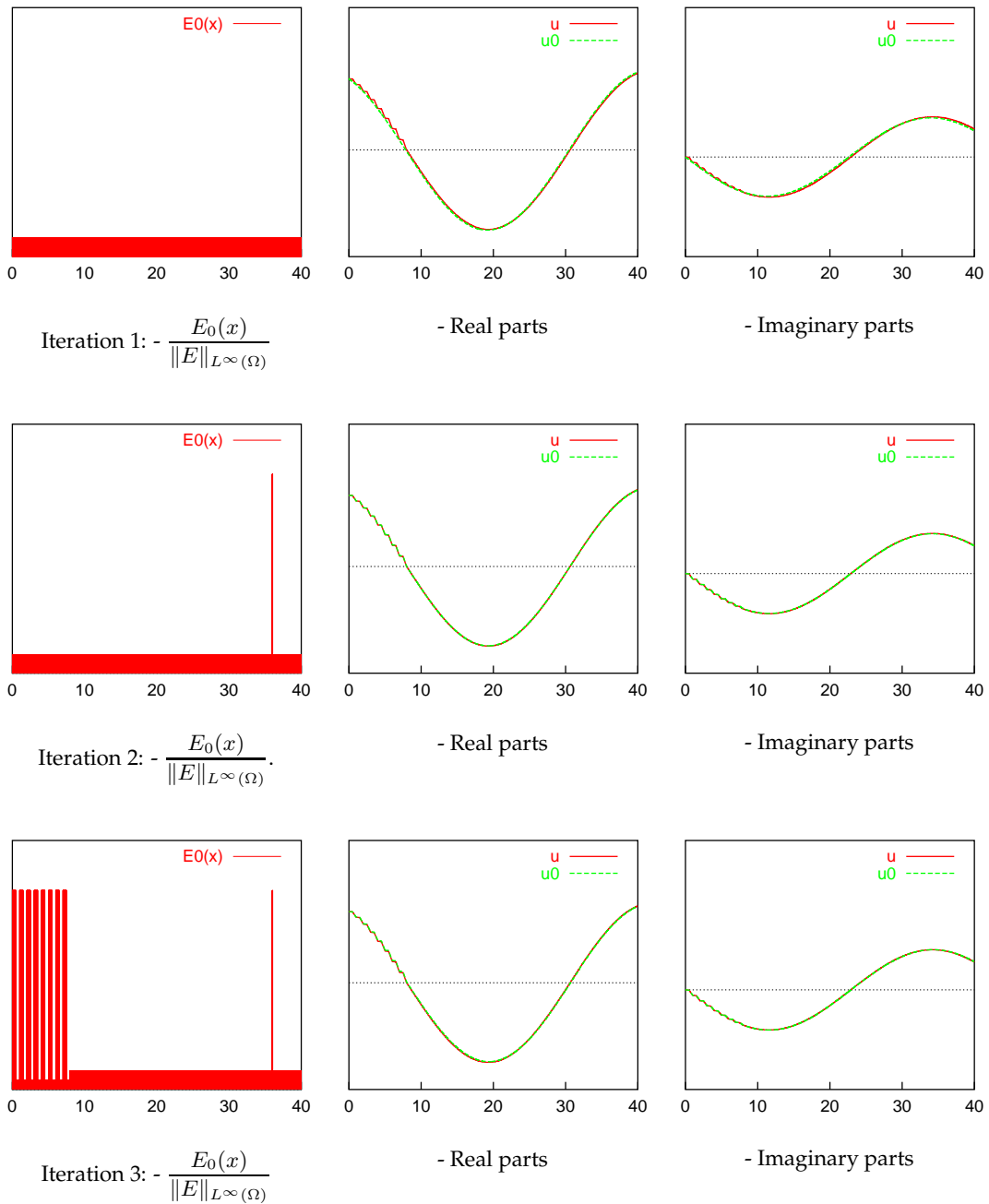


Figure 4.3: Snapshot solutions of the adaptive modeling analysis for the steady state wave, with  $\omega=200$  Hz, normalized by  $\|\mathbf{u}_0\|_{L^\infty(\Omega)}$ .

In Table 4.2, the adaptation results are listed for the more interesting case in which the frequency is high,  $\omega = 3000$  Hz. The relative error again decreases with each iteration and between some steps a factor 10 difference is observed. For iteration 1 through 6, the effectivity indices for  $\gamma_{\text{est}}$  exhibit good accuracy, with values close to 1. For the last iteration step, in which the relative error is  $\leq 10\%$ , a loss in accuracy for  $\gamma_{\text{est}}$  is observed, but the estimator is still of the right order. The explanation for the loss in accuracy is identical to the case in which  $\omega = 200$  Hz, iteration 2 (see previous remarks on Table 4.1).

Figure 4.4 displays the coarse material model, and the real and imaginary parts of the solutions  $\hat{\mathbf{u}}$  and  $\hat{\mathbf{u}}_0$  for iteration steps 1, 4, and 7. For iteration 4 and 7, Figure 4.4 shows that the adaptive process has incorporated the exact material properties in some subdomains into the coarse model.

Iteration	$\frac{ \hat{Q}(\hat{\mathbf{e}}_0) }{ \hat{Q}(\hat{\mathbf{u}}) }$	$\frac{ \gamma_{\text{est}} }{ \hat{Q}(\hat{\mathbf{e}}_0) }$	Error Indicators $\frac{\mathcal{E}_k}{ \Theta_k }$
1	0.152(2)	1.44	1 - 0.521(12) 2 - 0.468(12) 3 - 0.481(12) 4 - 0.503(12) 5 - 0.445(12) 6 - 0.424(13) 7 - 0.577(12)
2	0.354(1)	0.85	1 - 0.928(11) 2 - 0.835(11) 3 - 0.858(11) 4 - 0.896(11) 5 - 0.794(11) 7 - 0.106(12)
3	0.353(1)	1.41	1 - 0.885(11) 2 - 0.796(11) 3 - 0.820(11) 4 - 0.854(11) 5 - 0.758(11)
4	0.324(0)	1.19	2 - 0.244(11) 3 - 0.246(11) 4 - 0.260(11) 5 - 0.231(11)
5	0.278(0)	0.94	2 - 0.196(11) 3 - 0.197(11) 5 - 0.222(11)
6	0.253(0)	0.81	2 - 0.228(11) 3 - 0.229(11)
7	0.889(-1)	2.33	

Table 4.2: Data review of the adaptive modeling process for the steady state wave with a radial frequency of 3000 Hz.

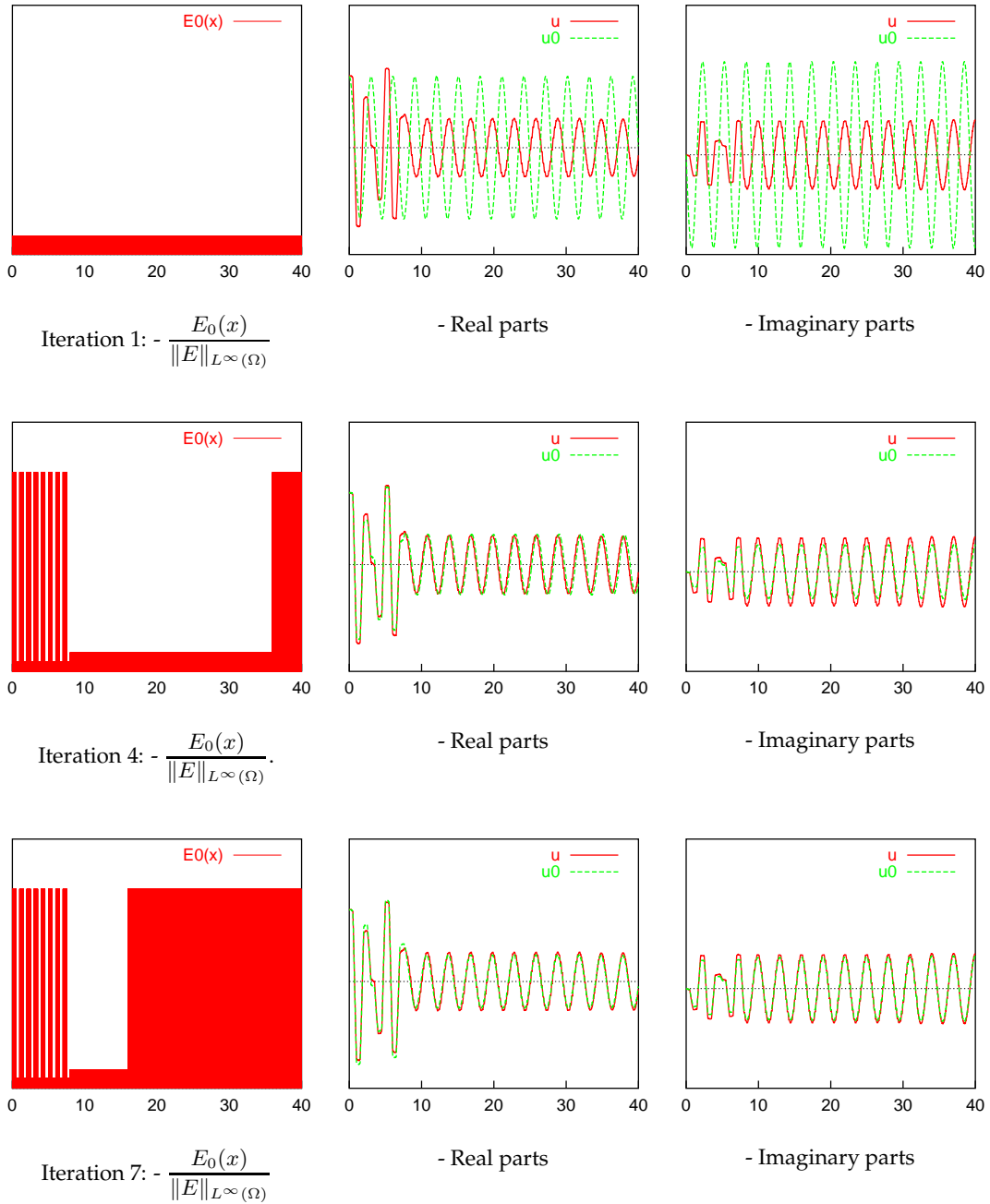


Figure 4.4: Snapshot solutions of the adaptive modeling analysis for the steady state wave, with  $\omega=3000$  Hz.

Note that the scale used in these graphical representations is such that the highly oscillatory material properties of adapted subdomains in zone II and III appear to be constant. For this frequency, capturing dispersion plays an important role in achieving an accurate solution. At the first iteration, with all homogeneous approximate material properties, there is a significant mismatch between the exact and approximate solution. The results for iteration 4, reveal that the sensitivity of the wave to the heterogeneity in zone I (or  $\Theta_1$ ) is the main source of error at the first iteration.

The step between iteration 3 and 4 clearly shows the nonlocal behavior of the adaptation process. After the material model in  $\Theta_1$ , far away from the domain of interest  $S$ , is adapted, a considerable increase of accuracy of the approximate solution is observed.

Finally, for a radial frequency of 4000 Hz, Table 4.3 and Figure 4.5 display similar results as seen for  $\omega = 3000$  Hz. Again,  $\gamma_{\text{est}}$  exhibits good accuracy and nonlocal model adaptation appears between iteration 3 and 4, and iteration 5 and 6. An extremely large range of the relative error is noted. For iteration 1, a relative error of approximately 3,000,000% is observed, which decreases continuously as the adaptive process is performed until it reaches a value of approximately 10% at iteration 7. For analyses in which the computational cost is a dominant criterion over solution accuracy, this final value of 10% suggests that error tolerances in the range of 5% may not be practical.

Iteration	$\frac{ \hat{Q}(\hat{\mathbf{e}}_0) }{ \hat{Q}(\hat{\mathbf{u}}) }$	$\frac{ \gamma_{\text{est}} }{ \hat{Q}(\hat{\mathbf{e}}_0) }$	Error Indicators $\frac{\mathcal{E}_k}{ \Theta_k }$
1	0.292(5)	1.51	1 - 0.550(12) 2 - 0.539(12) 3 - 0.538(12) 4 - 0.537(12) 5 - 0.505(12) 6 - 0.506(13) 7 - 0.567(12)
2	0.523(4)	0.84	1 - 0.971(11) 2 - 0.953(11) 3 - 0.951(11) 4 - 0.950(11) 5 - 0.839(11) 7 - 0.110(12)
3	0.479(1)	1.39	1 - 0.800(11) 2 - 0.784(11) 3 - 0.781(11) 4 - 0.781(11) 5 - 0.739(11)
4	0.609(0)	1.03	2 - 0.254(8) 3 - 0.253(8) 4 - 0.254(8) 5 - 0.263(8)
5	0.304(0)	0.65	2 - 0.196(8) 3 - 0.195(8) 4 - 0.195(8)
6	0.278(0)	0.81	3 - 0.172(8) 4 - 0.173(8)
7	0.127(0)	0.99	

Table 4.3: Data review of the adaptive modeling process for the steady state wave with a radial frequency of 4000 Hz.

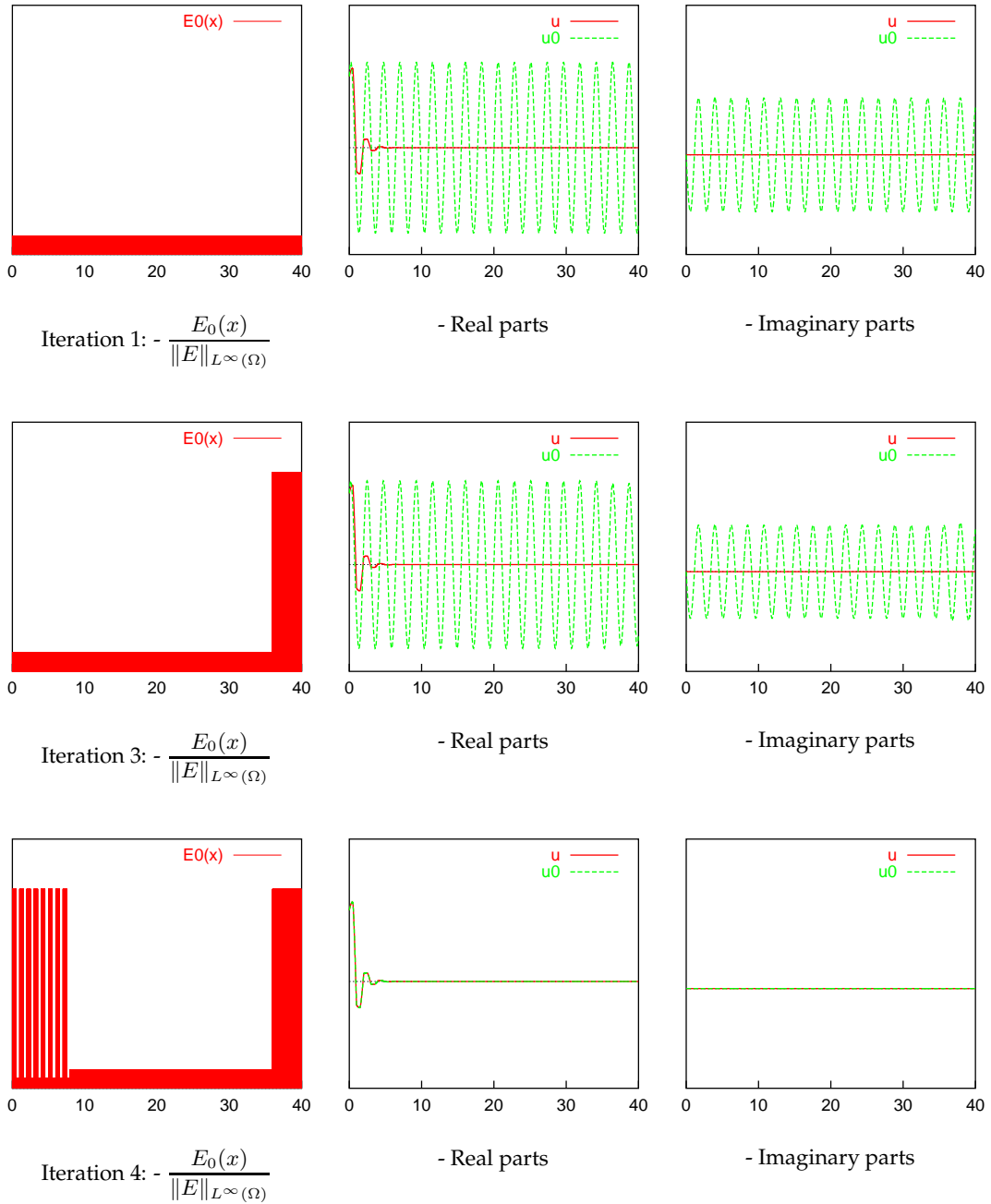


Figure 4.5: Snapshot solutions of the adaptive modeling analysis for the steady state wave, with  $\omega=4000$  Hz.

### 4.3.2 Transient Bandlimited Waves

The problem configuration is shown in Figure 4.6: a beam with 4 zones with different dimensions of inhomogeneity. Again, the material is made out of layers of carbon and epoxy (see Section 3.6 for material properties). The beam has a damping boundary condition at its right edge, and a driven displacement (Dirichlet) boundary condition at the left edge, whose frequency spectrum is bandlimited with a maximum frequency  $\omega_{\max}$ , *i.e.*

$$\hat{\mathbf{u}}(0) = \begin{cases} 1, & \text{for } |\omega| \leq \omega_{\max}, \\ 0, & \text{for } |\omega| > \omega_{\max}. \end{cases}$$

The domain is partitioned into 9 subdomains, such that:

$$\begin{aligned} \Theta_1 &= (0, 4), && \text{(contains zone I)} \\ \Theta_2 &= (4, 10), && \text{(in zone II)} \\ \Theta_3 &= (10, 16), && \text{(in zone II)} \\ \Theta_4 &= (16, 22), && \text{(in zone II)} \\ \Theta_5 &= (22, 25), && \text{(contains zone III)} \\ \Theta_6 &= (25, 30), && \text{(in zone IV)} \\ \Theta_7 &= (30, 31), && \text{(domain of interest)} \\ \Theta_8 &= (31, 35), && \text{(in zone IV)} \\ \Theta_9 &= (35, 40). && \text{(in zone IV)} \end{aligned}$$

The domain of interest  $S$ , on which the average stress is sought, is represented by  $\Theta_7$ . The approximate material properties at the beginning of the adaptive process are again obtained by applying the classical asymptotic homogenization technique and using the domain of interest  $S$  as the representative unit cell of the entire beam. Thus,

$$E_0 = 14.2 \text{ GPa}, \quad \rho_0 = 6.0 \text{ g/cm}^3.$$

The case in which  $\omega_{\max}$  is relatively low,  $\omega_{\max} = 1000 \text{ Hz}$ , is considered. The adaptive algorithm is applied by using a discretization of the frequency spectrum into 10 frequencies. The radial frequency  $\omega_n$  of a wave with frequency number  $n$ , is given by:

$$\omega_n = \frac{2\pi n}{T}, \quad n = 0, 1, \dots, 9$$

where the end time of the analysis  $T$  is 57 ms. In Table 4.4, an overview of the results after the first iteration step is shown, for 9 of the 10 frequencies. Here, the approximate material model consists of homogenized material properties. The results for  $n = 0$  are not listed as this mode does not have a contribution to the quantity of interest (a zero estimate is therefore 100% accurate).

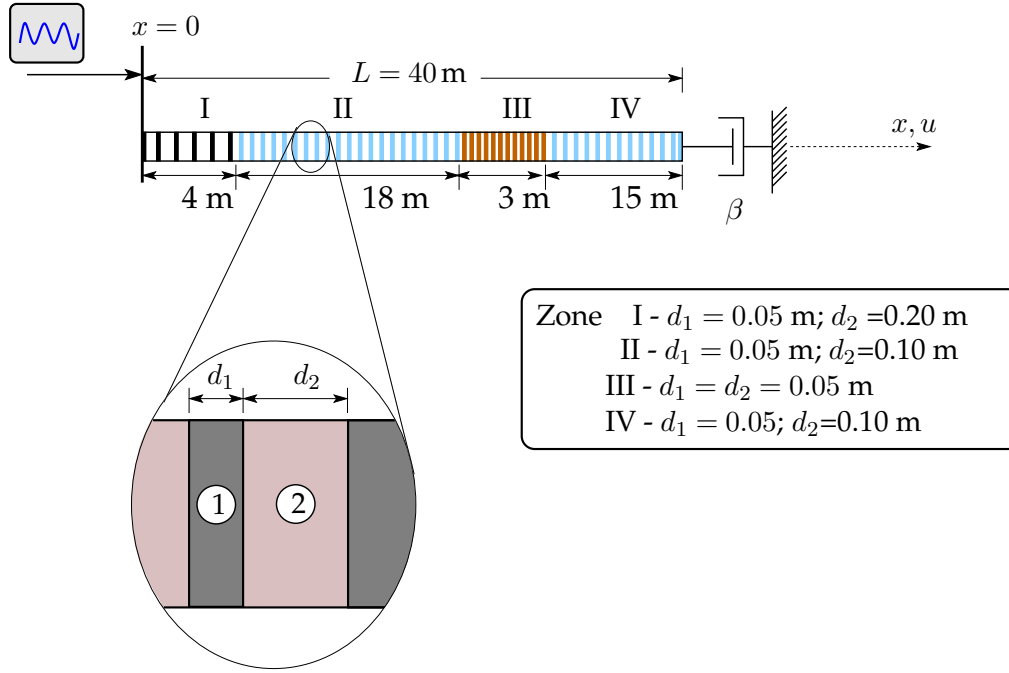


Figure 4.6: Transient problem of a beam with 4 zones of inhomogeneities.

By applying (3.33) upper bounds in time are obtained on the error in the quantity of interest and the quantity of interest itself. For this specific case, the ratio of the upper bound on the error and the bound on the quantity of interest is 9.1 after the first iteration step, which suggests high relative error for the time frame  $[0, T]$ .

frequency no.	$\omega$ (Hz)	$\frac{ \hat{Q}(\hat{\mathbf{e}}_0) }{ \hat{Q}(\hat{\mathbf{u}}) }$	$\frac{ \gamma_{\text{est}} }{ \hat{Q}(\hat{\mathbf{e}}_0) }$
1	111	4.94	1.07
2	222	7.56	1.35
3	333	6.00	1.55
4	444	8.70	1.96
5	556	6.73	1.25
6	667	13.3	1.40
7	778	11.8	1.06
8	889	10.9	1.67
9	1000	4.34	1.30

Table 4.4: Relative errors and effectivity indices for the estimator  $\gamma_{\text{est}}$ , after the first iteration step, when  $\omega_{\text{max}} = 1000$  Hz.

By using the estimates  $\{\gamma_{\text{est}}\}$ , an upper bound in time on the error estimate is obtained. After the first iteration step of the of the adaptive loop, the ratio of the bounds on the error estimate and the error itself is 1.38, which represents good accuracy of the estimator. The adaptive modeling algorithm is applied until the ratio of the upper bounds on the error and quantity of interest reaches a value below 0.4. In Table 4.5, an overview of the entire adaptive iteration procedure is recorded. For every iteration step, the critical frequency number, the subdomain with the highest contribution to the error, the ratio of the upper bounds on the error and the quantity of interest, and the effectivity index of the error estimator are listed. Note that the latter is defined as follows:

$$\text{Effectivity Index} = \frac{\text{upper bound on the error estimator}}{\text{upper bound on the error}}.$$

Initially, it is the domain of interest  $\Theta_7$  where the adaptation is applied for the first 7 iterations. The adaptation process subsequently concentrates on other subdomains. It is observed that especially for the higher frequencies the material model is adapted. Apparently, these waves are most sensitive to the inhomogeneity in the material. Overall, the estimate of the upper bound on the error shows good accuracy. Toward the end of the adaptive process, the effectivity index is pushed toward 2. This is caused by the effect observed previously: in those cases, there are waves for which the relative error is below 10%, and for which the effectivity index of the estimator  $\gamma_{\text{est}}$  moves toward an effectivity of 2 (see remarks on Tables 4.1 and 4.2 in Section 4.3.1). As a result, the overall effectivity index shifts to slightly higher values.

The solutions in time are computed by applying the discrete inverse Fourier transformation, as given in (3.32). The results for the computed stresses at times  $t = 14, 16$ , and  $18$  ms are plotted in Figure 4.7. In these graphs the exact stress is drawn as a solid red line. In the graphs in the left column, the approximate solution, as obtained after the first iteration (by using the homogenized material properties), is drawn as a dashed blue line. The approximate solution, obtained at the end of the adaptive modeling process, is drawn as a dashed green line in the graphs in the right column. At  $t = 14$  and  $18$  ms, it is observed that the mismatch in the homogenized and exact solution is large on the domain of interest  $S$  (also indicated in these graphs). The “adapted” solution, however, is very accurate and follows the exact solution quite nicely.

Results where the maximum frequency is higher, namely:  $\omega_{\text{max}} = 2000, 3000$ , and  $4000$  Hz, are also obtained. For these cases, the results after the first and the last iteration of the adaptive process are listed in respectively Tables 4.6 and 4.7. At the end of the first iteration, the ratios of the upper bounds on the error and the quantity of interest are large, close to 7 for all three cases, which suggest large relative errors for the time frame  $[0, T]$ . The estimate of the upper bound on the error appears to be accurate and the effectivity index varies between 1.1 to 1.3. At the end of the adaptive process, the relative error has been reduced significantly, since the ratio of the upper bounds on the error and the quantity of interest is low, close to 0.3, for all three frequencies. The effectivity index of the estimator has shifted to slightly higher values closer to 2. For the cases with higher  $\omega_{\text{max}}$ , more iterations are needed to obtain the required accuracy. This is caused by the fact that the inhomogeneity in this problem has a small scale. Only waves with small wave length (thus, high frequencies) will be sensitive to the inhomogeneity.

Iteration No.	Critical Freq. No.	$\Theta_{\text{crit}}$	$\frac{ Q(\mathbf{e}_0) }{ Q(\mathbf{u}) }$	Eff. Index of estimate on upper bound
1	7	7	7.09	1.45
2	6	7	5.41	1.43
3	8	7	3.08	1.25
4	9	7	2.90	1.41
5	5	7	2.33	1.25
6	3	7	1.81	1.17
7	4	7	1.40	0.94
8	6	2	1.32	1.04
9	4	7	1.05	1.56
10	7	9	1.01	1.04
11	7	4	0.94	1.05
12	8	4	0.86	1.00
13	6	9	0.81	1.03
14	7	3	0.75	1.11
15	6	6	0.72	1.12
16	8	3	0.66	1.18
17	6	3	0.64	1.18
18	6	8	0.63	1.12
19	7	2	0.58	1.18
20	1	7	0.48	1.21
21	6	5	0.45	1.26
22	5	6	0.44	1.50
23	5	4	0.44	1.57
24	5	2	0.43	1.69
25	8	6	0.39	1.79

Table 4.5: Summary on iterative adaption process for  $\omega_{\text{max}}=1000$  Hz.

$\omega_{\max}$ (Hz)	Number of frequencies	$\frac{ Q(\mathbf{e}_0) }{ Q(\mathbf{u}) }$	Eff. Index for estimate on the upper bound
2000	19	7.35	1.31
3000	28	6.99	1.10
4000	37	7.46	1.18

Table 4.6: Ratios of the upper bounds on the error and the quantity of interest, and effectivity indices for the upper bounds on the error estimator, after the first iteration step.

$\omega_{\max}$ (Hz)	Number of iterations	$\frac{ Q(\mathbf{e}_0) }{ Q(\mathbf{u}) }$	Eff. Index for estimate on the upper bound
2000	47	0.35	1.32
3000	93	0.33	1.64
4000	128	0.32	2.33

Table 4.7: Ratios of the upper bounds on the error and the quantity of interest, and effectivity indices for the upper bounds on the error estimator, after the last iteration step.

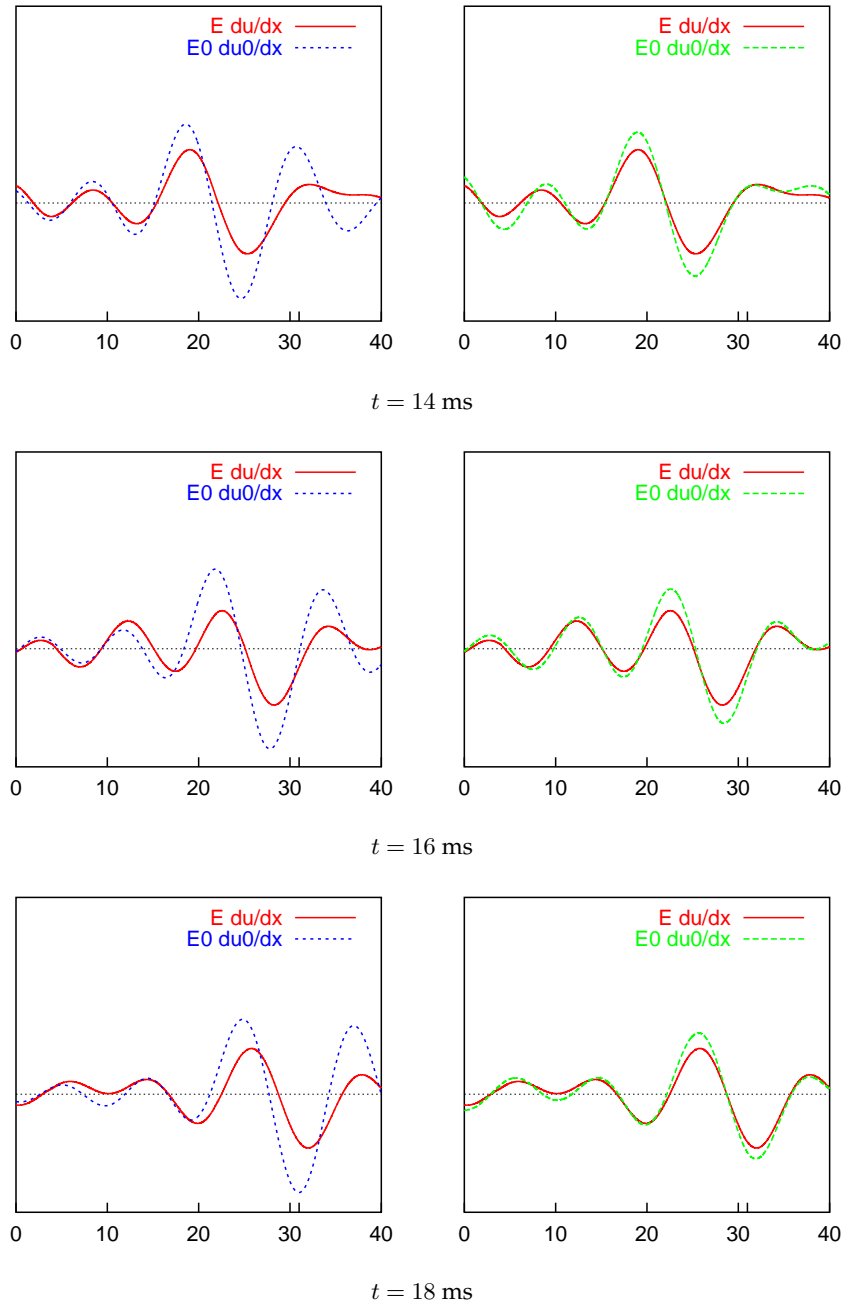


Figure 4.7: Bandlimited wave,  $\omega_{max} = 1000 \text{ Hz}$ : Comparison of the exact solution with the homogenized solution (left), and the adapted solution (right); all are normalized by maximum of  $E \mathbf{d}u(x, t) / dx$ ,  $x \in \Omega$ ,  $t \in [0, 0.057]$ .

In Figures 4.8 through 4.10, the computed evolution of stresses is shown. As expected, the effect of dispersion is observed to increase as  $\omega_{\max}$  increases. As a consequence, the homogenized solutions represent a very poor approximation as  $\omega_{\max}$  reaches higher values. The phenomenon of trailing waves [3] is observed in particular for the solutions for  $\omega_{\max} = 4000$  Hz. The solutions obtained through the adaptive modeling process not only follow the exact solution in the domain of interest, but also globally are much more accurate.

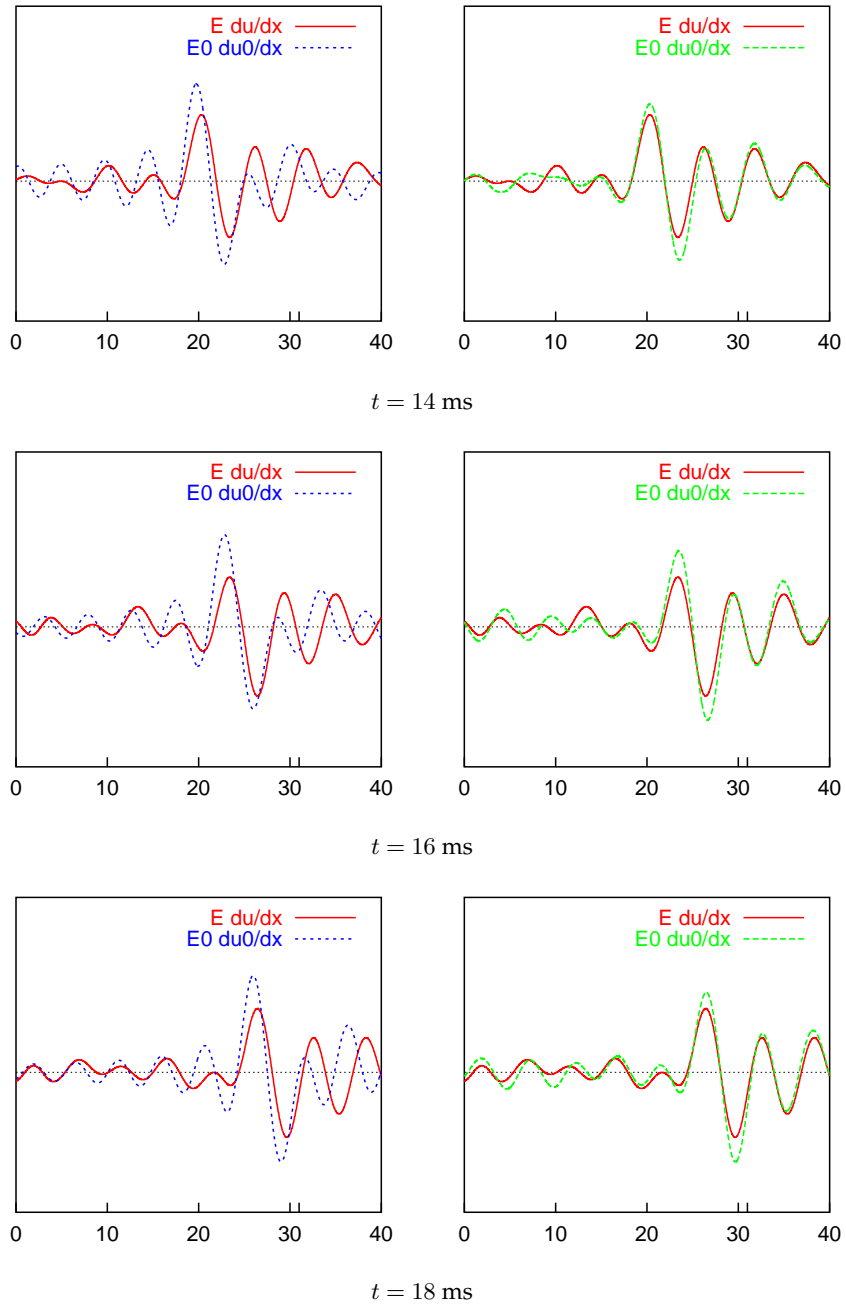


Figure 4.8: Bandlimited wave,  $\omega_{max} = 2000 \text{ Hz}$ : Comparison of the exact solution with the homogenized solution (left), and the adapted solution (right); all are normalized by maximum of  $E \mathbf{d} \mathbf{u}(x, t) / \mathbf{d} x$ ,  $x \in \Omega$ ,  $t \in [0, 0.057]$ .

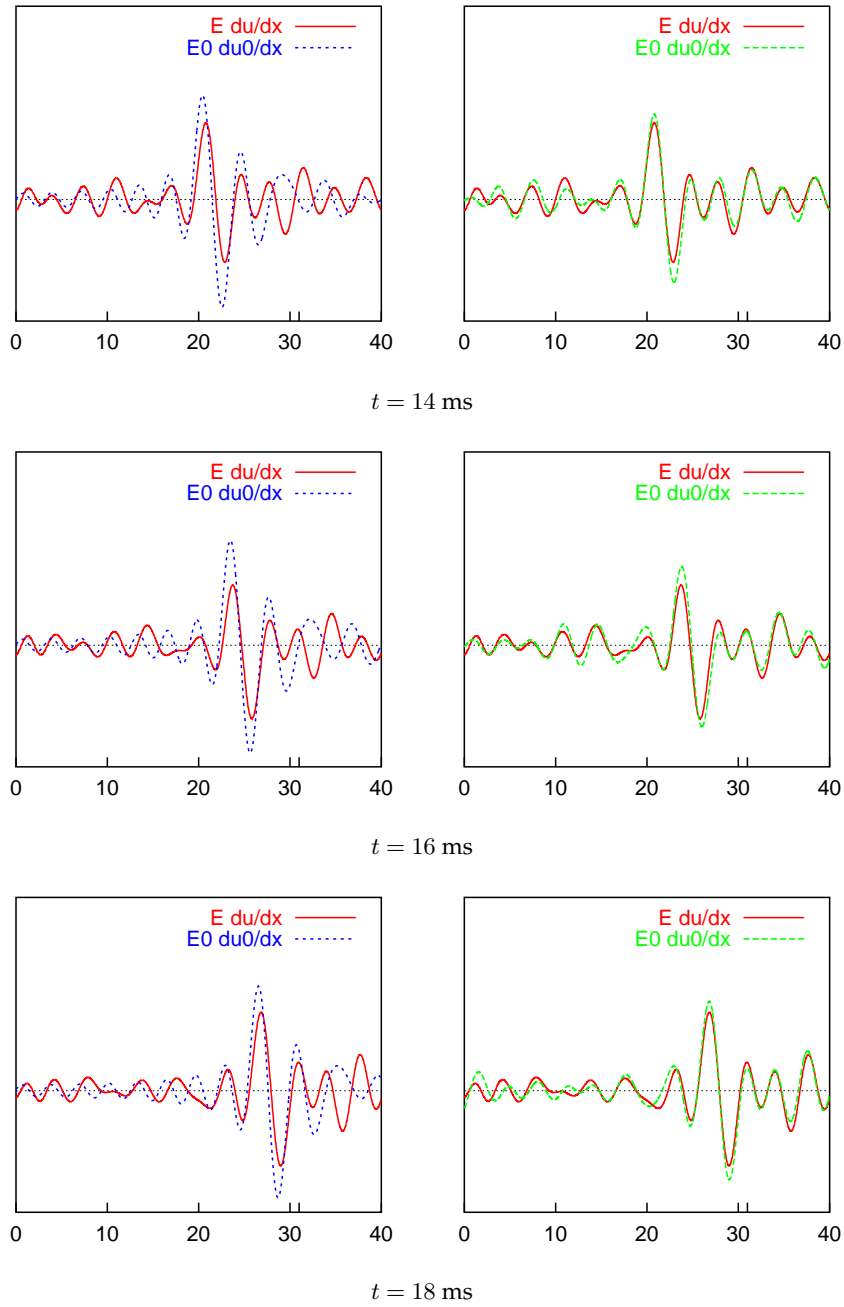


Figure 4.9: Bandlimited wave,  $\omega_{max} = 3000 \text{ Hz}$ : Comparison of the exact solution with the homogenized solution (left), and the adapted solution (right); all are normalized by maximum of  $E \mathbf{d}u(x, t) / dx$ ,  $x \in \Omega$ ,  $t \in [0, 0.057]$ .

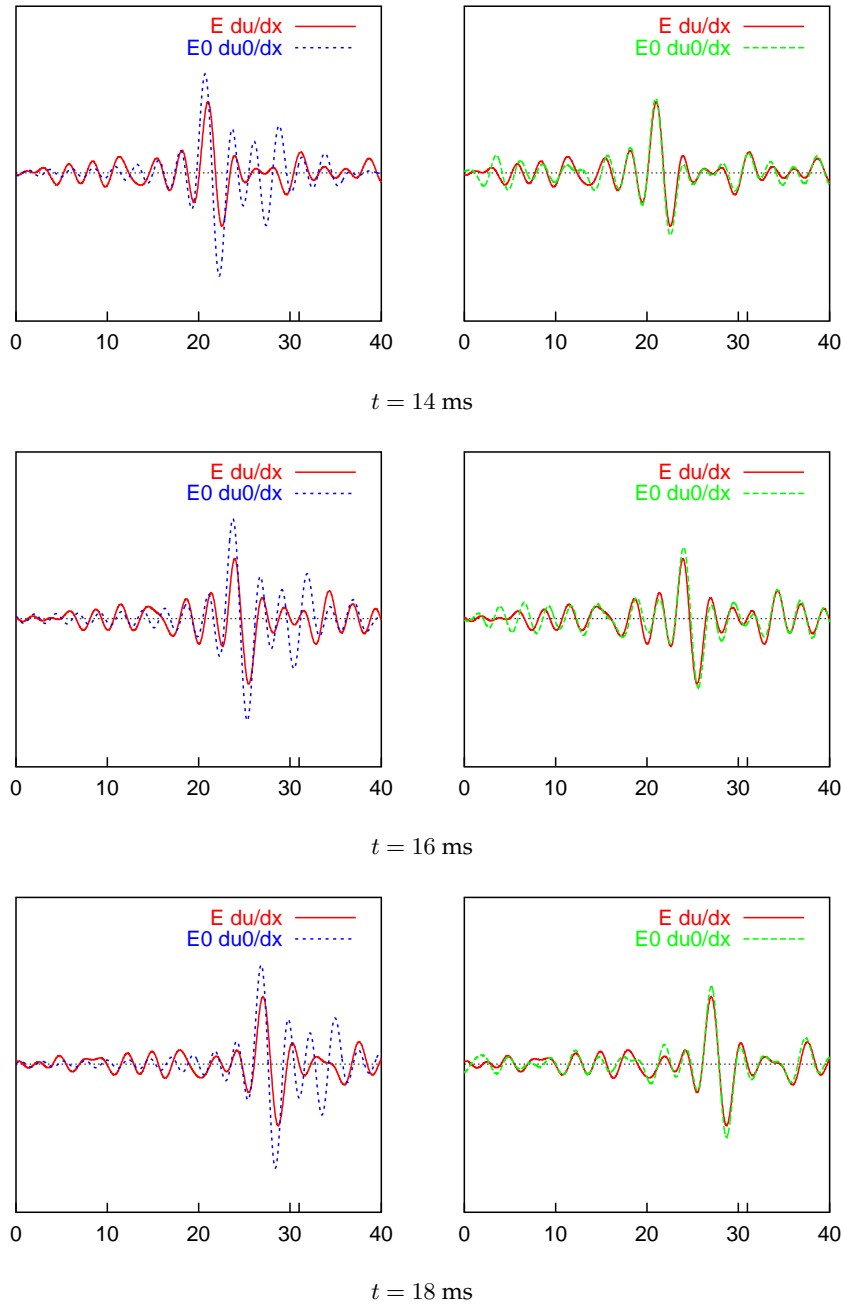


Figure 4.10: Bandlimited wave,  $\omega_{max} = 4000 \text{ Hz}$ : Comparison of the exact solution with the homogenized solution (left), and the adapted solution (right); all are normalized by maximum of  $E \mathbf{d}u(x, t) / dx$ ,  $x \in \Omega$ ,  $t \in [0, 0.057]$ .

## 5 Concluding Remarks

A mathematical theory and computational procedures are presented for a systematic analysis of wave propagation in elastic heterogeneous media. The issue of mathematical modeling of this phenomenon is addressed by applying a general notion [17] of residual-based *a posteriori* analysis of errors occurring in problems in computational engineering sciences. The main conclusions of this work can be summarized as follows:

- The general framework [17] for error analysis is applied to derive an *a posteriori* estimate of the modeling error in a quantity of interest, the average stress on a subdomain. This makes possible the accurate assessment of the error caused by the occurrence of geometric wave dispersion, characteristic to dynamic behavior in heterogeneous media, but also of errors caused by local features, such as inaccurate descriptions of the local material model.
- Lower bounds to a global norm of the modeling error are derived, that in the presence of sufficient damping in the system, represent reasonably accurate *a posteriori* estimates.
- Nonlocal error indicators are introduced that enable nonlocal model adaptation and, therefore, make possible the successful control of geometric dispersion.
- The concept of goal-oriented adaptive modeling, introduced by Zohdi, Oden and Rodin [29], and Oden and Vemaganti [19, 20, 26, 27], is extended and successfully applied to the elastodynamic wave problem. An adaptive modeling algorithm is presented that solves the wave problem in the frequency domain and allows an adaptation of the models only for those waves that contribute most to the error. In practical applications, this implies that the algorithm makes possible the identification of waves that are most dispersion sensitive to the dimension of the inhomogeneity in the material. The error indicators can then be used to adapt the material model nonlocally for these critical frequencies and enable the identification of those regions in the elastic body that contribute to dispersion.

As future extensions of this work, one could consider the application of the adaptive modeling methodology to the inverse problem, *i.e.* knowing the response one would seek the actual material model within a degree of certainty or accuracy. This application finds its interest in many disciplines of engineering sciences, such as *e.g.* seismology and structural acoustics.

Also, the incorporation of control of the numerical approximation error into the algorithm is a possible extension. The resulting methodology would consequently address both the issues of Verification and Validation of wave propagation in heterogeneous media.

Apart from these areas, there are many fields to be explored for future extension of the GOALS methodology, such as, for example: nonlinear elasticity, visco-elasticity, plasticity, and fluid flow problems.

### **Acknowledgment**

The support of this work, under DoD Navy Grant No. N00014-99-1-0124, is gratefully acknowledged.

# References

- [1] BALENDRAN, B., AND NEMAT-NASSER, S. Bounds on elastic moduli of composites. *Journal of Mechanics, Physics and Solids* 43 (1995), 1825–1853.
- [2] BECKER, R., AND RANNACHER, R. An optimal control approach to a *posteriori* error estimation in finite element methods. In *Acta Numerica*, A. Iserles, Ed., vol. 10. Cambridge University Press, 2002, pp. 1–102.
- [3] BEDFORD, A., AND DRUMHELLER, D. S. *Introduction to Elastic Wave Propagation*. John Wiley & Sons, 1994.
- [4] BEDFORD, A., DRUMHELLER, D. S., AND SUTHERLAND, H. J. On modeling the dynamics of composite materials. In *Mechanics Today*, S. Nemat-Nasser, Ed., vol. 3. Pergamom Press, 1976, pp. 1–54.
- [5] BENSOUSSAN, A., LIONS, J. L., AND PAPANICOLAOU, G. *Asymptotic Analysis for Periodic Structures*, vol. 5 of *Studies in Mathematics and its Applications*. North-Holland, Amsterdam, 1978.
- [6] FISH, J., CHEN, W., AND NAGAI, G. Non-local dispersive model for wave propagation in heterogeneous media: Multi-dimensional case. *International Journal for Numerical Methods in Engineering* 54 (2002), 347–363.
- [7] FISH, J., CHEN, W., AND NAGAI, G. Non-local dispersive model for wave propagation in heterogeneous media: One-dimensional case. *International Journal for Numerical Methods in Engineering* 54 (2002), 331–346.
- [8] FU, Y., KLIMKOWSKI, K. J., RODIN, G. J., BERGER, E., BROWNE, J. C., SINGER, J. K., VAN DE GEIJN, R. A., AND VEMAGANTI, K. A fast solution method for three-dimensional many particle problems of linear elasticity. *International Journal for Numerical Methods in Engineering* 42 (1998), 1215–1229.
- [9] GHOSH, S., LEE, K., AND MOORTHY, S. Two scale analysis of heterogeneous elastic-plastic materials with asymptotic homogenization and Voronoi Cell Finite Element Method. *Computer Methods in Applied Mechanics and Engineering* 132 (1996), 63–116.
- [10] GHOSH, S., AND LIU, Y. Voronoi Cell Finite Element model based on micropolar theory of thermoelasticity for heterogeneous materials. *International Journal for Numerical Methods in Engineering* 38 (1995), 1361–1398.

- [11] GHOSH, S., AND MOORTHY, S. Elastic-plastic analysis of arbitrary heterogeneous materials with the Voronoi Cell Finite Element Method. *Computer Methods in Applied Mechanics and Engineering* 121 (1995), 373–409.
- [12] GUEDES, J. M., AND KIKUCHI, N. Preprocessing and postprocessing for materials based on the homogenization method with adaptive finite element methods. *Computer Methods in Applied Mechanics and Engineering* 83 (1990), 143–198.
- [13] HASHIN, Z. Analysis of composite materials, a survey. *Journal of Applied Mechanics* 50 (1983), 481–505.
- [14] HILL, R. The elastic behavior of crystalline aggregate. In *Proc. Phys. Soc. London* (1952), vol. 65, pp. 349–354.
- [15] NEMAT-NASSER, S., AND HORI, M. Universal bounds for overall properties of linear and nonlinear heterogeneous solids. *J. Engng. Mat. Tech* 117 (1995), 412–432.
- [16] ODEN, J. T., AND DEMKOWICZ, L. F. *Applied Functional Analysis*. CRC Press, New York, 1996.
- [17] ODEN, J. T., AND PRUDHOMME, S. Estimation of modeling error in computational mechanics. *Journal of Computational Physics* 182 (2002), 496–515.
- [18] ODEN, J. T., AND PRUDHOMME, S. Computable error estimators and adaptive techniques for fluid flow problems. In *Lecture Notes in Computational Science and Engineering*, T. J. Barth and H. Deconinck, Eds., vol. 25. Springer Verlag, 2003, pp. 207–268.
- [19] ODEN, J. T., AND VEMAGANTI, K. Estimation of local modeling error and goal-oriented adaptive modeling of heterogeneous materials. part I: Error estimates and adaptive algorithms. *Journal of Computational Physics* 164 (2000), 22–47.
- [20] ODEN, J. T., AND VEMAGANTI, K. S. Adaptive modeling of composite structures: Modeling error estimation. *Int. Journal Comp. Civil Str. Engrg.* 1 (2000), 1–16.
- [21] ODEN, J. T., AND ZOHDI, T. I. Analysis and adaptive modeling of highly heterogeneous elastic structures. *Computer Methods in Applied Mechanics and Engineering* 148 (1997), 367–391.
- [22] ROMKES, A. *Modeling of Wave Phenomena in Heterogeneous Elastic Solids*. PhD thesis, The University of Texas at Austin, 2003.
- [23] SANCHEZ-PALENCIA, E. *Lecture Notes in Physics, Nonhomogeneous Media and Vibration Theory*, vol. 127. Springer Verlag, Berlin Heidelberg New York, 1980.
- [24] TERADA, K., AND KIKUCHI, N. Nonlinear homogenization method for practical applications. In *Computational Methods in Micromechanics*, S. Ghosh and M. Ostoja-Starzewski, Eds., vol. 212. ASMD AMD, 1995, pp. 1–16.
- [25] TERADA, K., MIURA, T., AND KIKUCHI, N. Digital image based modeling applied to the homogenization analysis of composite materials. *Comp. Mech.* 20 (1997), 331–346.

- [26] VEMAGANTI, K. *Goal-Oriented Adaptive Modeling of Heterogeneous Elastic Solids*. PhD thesis, The University of Texas at Austin, 2000.
- [27] VEMAGANTI, K., AND ODEN, J. T. Estimation of local modeling error and goal-oriented adaptive modeling of heterogeneous materials. part II: A computational environment for adaptive modeling of heterogeneous elastic solids. *Computer Methods in Applied Mechanics and Engineering* 190 (2001), 6089–6124.
- [28] ZOHDİ, T. I. *Analysis and Adaptive Modeling of Highly Heterogeneous Elastic Structures*. PhD thesis, The University of Texas at Austin, 1997.
- [29] ZOHDİ, T. I., ODEN, J. T., AND RODIN, G. J. Hierarchical modeling of heterogeneous bodies. *Computer Methods in Applied Mechanics and Engineering* 138 (1996), 273–298.

# Appendix A

## Derivation of Optimal Lower Bounds $\eta_{\text{low}(,i)}^\pm$

In this section, a more detailed derivation is presented of the bounds  $\eta_{\text{low}(,i)}^\pm$  that are introduced in Lemma 3.4.1. Since the derivations of the four bounds are similar, the derivation of only one bound,  $\eta_{\text{low}}^+$ , is shown. First, by recalling the result in the proof of Lemma 3.4.1, one gets:

$$\|\hat{\mathbf{e}}_1 + \hat{\varepsilon}_1\|_{\mathcal{H}} \geq \frac{|\mathcal{R}(\hat{\mathbf{u}}_0 + \hat{\mathbf{p}}_0, \hat{\mathbf{u}}_0 + \theta^+ \hat{\mathbf{p}}_0)|}{\|\hat{\mathbf{u}}_0 + \theta^+ \hat{\mathbf{p}}_0\|_{\mathcal{H}}}, \quad \forall \theta^+ \in \mathbb{C}.$$

$\eta_{\text{low}}^+$  is chosen to be equal to the RHS with a value of  $\theta^+$  for which this RHS reaches a maximum. Clearly a lower bound that is closer to  $\|\hat{\mathbf{e}}_1 + \hat{\varepsilon}_1\|_{\mathcal{H}}$ , provides a more accurate estimate of this norm and, inherently, the modeling error. Hence, the RHS has to be minimized with respect to  $\theta^+$ . By taking the following expansion:  $\theta^+ = a + bi$ , the RHS of the above expression can be rewritten as follows:

$$\frac{|\mathcal{R}(\hat{\mathbf{u}}_0 + \hat{\mathbf{p}}_0, \hat{\mathbf{u}}_0 + (a + bi)\hat{\mathbf{p}}_0)|}{\|\hat{\mathbf{u}}_0 + (a + bi)\hat{\mathbf{p}}_0\|_{\mathcal{H}}} = \Phi(a, b), \quad \forall a, b \in \mathbb{R}.$$

By applying the definition (3.13) of the norm  $\|\cdot\|_{\mathcal{H}}$  and the norm definition of a complex-valued number:  $|z| = \sqrt{z\bar{z}}$ , one gets:

$$\Phi(a, b) = \sqrt{\frac{\mathcal{R}(\hat{\mathbf{u}}_0 + \hat{\mathbf{p}}_0, \hat{\mathbf{u}}_0 + (a + bi)\hat{\mathbf{p}}_0)\overline{\mathcal{R}(\hat{\mathbf{u}}_0 + \hat{\mathbf{p}}_0, \hat{\mathbf{u}}_0 + (a + bi)\hat{\mathbf{p}}_0)}}{\mathcal{H}(\hat{\mathbf{u}}_0 + (a + bi)\hat{\mathbf{p}}_0, \hat{\mathbf{u}}_0 + (a + bi)\hat{\mathbf{p}}_0)}} = \sqrt{\varphi(a, b)}.$$

The minimizers of this terms are numbers  $a$  and  $b$  such that  $\frac{\partial \Phi}{\partial a} = \frac{\partial \Phi}{\partial b} = 0$ . This implies:

$$\left. \begin{aligned} \frac{\partial \Phi}{\partial \varphi} \frac{\partial \varphi}{\partial a} = \frac{1}{2\sqrt{\varphi}} \frac{\partial \varphi}{\partial a} = 0, \\ \frac{\partial \Phi}{\partial \varphi} \frac{\partial \varphi}{\partial b} = \frac{1}{2\sqrt{\varphi}} \frac{\partial \varphi}{\partial b} = 0, \end{aligned} \right\} \Rightarrow \boxed{\frac{\partial \varphi}{\partial a} = 0, \quad \frac{\partial \varphi}{\partial b} = 0.}$$

After several algebraic manipulations, the following is obtained for  $\frac{\partial \varphi}{\partial a}$ :

$$\begin{aligned}
\frac{\partial \varphi}{\partial a} = & \frac{1}{\|\hat{\mathbf{u}}_0 + (a + bi)\hat{\mathbf{p}}_0\|_{\mathcal{H}}^2} \left\{ 2 \left[ \operatorname{Re} \left\{ \mathcal{R}(\hat{\mathbf{u}}_0 + \hat{\mathbf{p}}_0, \hat{\mathbf{p}}_0) \overline{\mathcal{R}(\hat{\mathbf{u}}_0 + \hat{\mathbf{p}}_0, \hat{\mathbf{u}}_0)} \right\} \|\hat{\mathbf{u}}_0\|_{\mathcal{H}}^2 \right. \right. \\
& \left. \left. - |\mathcal{R}(\hat{\mathbf{u}}_0 + \hat{\mathbf{p}}_0, \hat{\mathbf{u}}_0)|^2 \operatorname{Re} \{ \mathcal{H}(\hat{\mathbf{u}}_0, \hat{\mathbf{p}}_0) \} \right] \right. \\
& + 2a \left[ |\mathcal{R}(\hat{\mathbf{u}}_0 + \hat{\mathbf{p}}_0, \hat{\mathbf{p}}_0)|^2 \|\hat{\mathbf{u}}_0\|_{\mathcal{H}}^2 - |\mathcal{R}(\hat{\mathbf{u}}_0 + \hat{\mathbf{p}}_0, \hat{\mathbf{u}}_0)|^2 \|\hat{\mathbf{p}}_0\|_{\mathcal{H}}^2 \right] \\
& + 4ab \left[ \operatorname{Im} \left\{ \mathcal{R}(\hat{\mathbf{u}}_0 + \hat{\mathbf{p}}_0, \hat{\mathbf{u}}_0) \overline{\mathcal{R}(\hat{\mathbf{u}}_0 + \hat{\mathbf{p}}_0, \hat{\mathbf{p}}_0)} \right\} \|\hat{\mathbf{p}}_0\|_{\mathcal{H}}^2 \right. \\
& \left. + |\mathcal{R}(\hat{\mathbf{u}}_0 + \hat{\mathbf{p}}_0, \hat{\mathbf{p}}_0)|^2 \operatorname{Im} \{ \mathcal{H}(\hat{\mathbf{u}}_0, \hat{\mathbf{p}}_0) \} \right] \\
& - 2a^2 \left[ \operatorname{Re} \left\{ \mathcal{R}(\hat{\mathbf{u}}_0 + \hat{\mathbf{p}}_0, \hat{\mathbf{u}}_0) \overline{\mathcal{R}(\hat{\mathbf{u}}_0 + \hat{\mathbf{p}}_0, \hat{\mathbf{p}}_0)} \right\} \|\hat{\mathbf{p}}_0\|_{\mathcal{H}}^2 \right. \\
& \left. - |\mathcal{R}(\hat{\mathbf{u}}_0 + \hat{\mathbf{p}}_0, \hat{\mathbf{p}}_0)|^2 \operatorname{Re} \{ \mathcal{H}(\hat{\mathbf{u}}_0, \hat{\mathbf{p}}_0) \} \right] \\
& + 4b \left[ \operatorname{Re} \left\{ \mathcal{R}(\hat{\mathbf{u}}_0 + \hat{\mathbf{p}}_0, \hat{\mathbf{p}}_0) \overline{\mathcal{R}(\hat{\mathbf{u}}_0 + \hat{\mathbf{p}}_0, \hat{\mathbf{u}}_0)} \right\} \operatorname{Im} \{ \mathcal{H}(\hat{\mathbf{u}}_0, \hat{\mathbf{p}}_0) \} \right. \\
& \left. + \operatorname{Im} \left\{ \mathcal{R}(\hat{\mathbf{u}}_0 + \hat{\mathbf{p}}_0, \hat{\mathbf{u}}_0) \overline{\mathcal{R}(\hat{\mathbf{u}}_0 + \hat{\mathbf{p}}_0, \hat{\mathbf{p}}_0)} \right\} \operatorname{Re} \{ \mathcal{H}(\hat{\mathbf{u}}_0, \hat{\mathbf{p}}_0) \} \right] \\
& + 2b^2 \left[ \operatorname{Re} \left\{ \mathcal{R}(\hat{\mathbf{u}}_0 + \hat{\mathbf{p}}_0, \hat{\mathbf{p}}_0) \overline{\mathcal{R}(\hat{\mathbf{u}}_0 + \hat{\mathbf{p}}_0, \hat{\mathbf{u}}_0)} \right\} \|\hat{\mathbf{p}}_0\|_{\mathcal{H}}^2 \right. \\
& \left. - |\mathcal{R}(\hat{\mathbf{u}}_0 + \hat{\mathbf{p}}_0, \hat{\mathbf{p}}_0)|^2 \operatorname{Re} \{ \mathcal{H}(\hat{\mathbf{u}}_0, \hat{\mathbf{p}}_0) \} \right] \left. \right\}.
\end{aligned}$$

Whereas, for  $\frac{\partial \varphi}{\partial b}$  one gets:

$$\begin{aligned}
\frac{\partial \varphi}{\partial b} = & \frac{1}{\|\hat{\mathbf{u}}_0 + (a + bi)\hat{\mathbf{p}}_0\|_{\mathcal{H}}^2} \left\{ 2 \left[ \mathcal{I}m \left\{ \mathcal{R}(\hat{\mathbf{u}}_0 + \hat{\mathbf{p}}_0, \hat{\mathbf{p}}_0) \overline{\mathcal{R}(\hat{\mathbf{u}}_0 + \hat{\mathbf{p}}_0, \hat{\mathbf{u}}_0)} \right\} \|\hat{\mathbf{u}}_0\|_{\mathcal{H}}^2 \right. \right. \\
& \left. \left. - |\mathcal{R}(\hat{\mathbf{u}}_0 + \hat{\mathbf{p}}_0, \hat{\mathbf{u}}_0)|^2 \mathcal{I}m \{ \mathcal{H}(\hat{\mathbf{u}}_0, \hat{\mathbf{p}}_0) \} \right] \right. \\
& + 4a \left[ \mathcal{I}m \left\{ \mathcal{R}(\hat{\mathbf{u}}_0 + \hat{\mathbf{p}}_0, \hat{\mathbf{p}}_0) \overline{\mathcal{R}(\hat{\mathbf{u}}_0 + \hat{\mathbf{p}}_0, \hat{\mathbf{u}}_0)} \right\} \mathcal{R}e \{ \mathcal{H}(\hat{\mathbf{u}}_0, \hat{\mathbf{p}}_0) \} \right. \\
& \left. \left. - \mathcal{R}e \left\{ \mathcal{R}(\hat{\mathbf{u}}_0 + \hat{\mathbf{p}}_0, \hat{\mathbf{u}}_0) \overline{\mathcal{R}(\hat{\mathbf{u}}_0 + \hat{\mathbf{p}}_0, \hat{\mathbf{p}}_0)} \right\} \mathcal{I}m \{ \mathcal{H}(\hat{\mathbf{u}}_0, \hat{\mathbf{p}}_0) \} \right] \right. \\
& - 4ab \left[ \mathcal{R}e \left\{ \mathcal{R}(\hat{\mathbf{u}}_0 + \hat{\mathbf{p}}_0, \hat{\mathbf{u}}_0) \overline{\mathcal{R}(\hat{\mathbf{u}}_0 + \hat{\mathbf{p}}_0, \hat{\mathbf{p}}_0)} \right\} \|\hat{\mathbf{p}}_0\|_{\mathcal{H}}^2 \right. \\
& \left. \left. - |\mathcal{R}(\hat{\mathbf{u}}_0 + \hat{\mathbf{p}}_0, \hat{\mathbf{p}}_0)|^2 \mathcal{R}e \{ \mathcal{H}(\hat{\mathbf{u}}_0, \hat{\mathbf{p}}_0) \} \right] \right. \\
& + 2a^2 \left[ \mathcal{I}m \left\{ \mathcal{R}(\hat{\mathbf{u}}_0 + \hat{\mathbf{p}}_0, \hat{\mathbf{p}}_0) \overline{\mathcal{R}(\hat{\mathbf{u}}_0 + \hat{\mathbf{p}}_0, \hat{\mathbf{u}}_0)} \right\} \|\hat{\mathbf{p}}_0\|_{\mathcal{H}}^2 \right. \\
& \left. \left. - |\mathcal{R}(\hat{\mathbf{u}}_0 + \hat{\mathbf{p}}_0, \hat{\mathbf{p}}_0)|^2 \mathcal{I}m \{ \mathcal{H}(\hat{\mathbf{u}}_0, \hat{\mathbf{p}}_0) \} \right] \right. \\
& + 2b \left[ |\mathcal{R}(\hat{\mathbf{u}}_0 + \hat{\mathbf{p}}_0, \hat{\mathbf{p}}_0)|^2 \|\hat{\mathbf{u}}_0\|_{\mathcal{H}}^2 - |\mathcal{R}(\hat{\mathbf{u}}_0 + \hat{\mathbf{p}}_0, \hat{\mathbf{u}}_0)|^2 \|\hat{\mathbf{p}}_0\|_{\mathcal{H}}^2 \right] \\
& + 2b^2 \left[ \mathcal{I}m \left\{ \mathcal{R}(\hat{\mathbf{u}}_0 + \hat{\mathbf{p}}_0, \hat{\mathbf{u}}_0) \overline{\mathcal{R}(\hat{\mathbf{u}}_0 + \hat{\mathbf{p}}_0, \hat{\mathbf{p}}_0)} \right\} \|\hat{\mathbf{p}}_0\|_{\mathcal{H}}^2 \right. \\
& \left. \left. + |\mathcal{R}(\hat{\mathbf{u}}_0 + \hat{\mathbf{p}}_0, \hat{\mathbf{p}}_0)|^2 \mathcal{I}m \{ \mathcal{H}(\hat{\mathbf{u}}_0, \hat{\mathbf{p}}_0) \} \right] \right\}.
\end{aligned}$$

To simplify notations,  $\hat{\varphi}_a$  and  $\hat{\varphi}_b$  are introduced, such that:

$$\frac{\partial \varphi}{\partial a} = \frac{1}{\|\hat{\mathbf{u}}_0 + (a + bi)\hat{\mathbf{p}}_0\|_{\mathcal{H}}^2} \hat{\varphi}_a, \quad \frac{\partial \varphi}{\partial b} = \frac{1}{\|\hat{\mathbf{u}}_0 + (a + bi)\hat{\mathbf{p}}_0\|_{\mathcal{H}}^2} \hat{\varphi}_b.$$

It is clear that  $a$  and  $b$  that maximize the lower bound, satisfy  $\hat{\varphi}_a = \hat{\varphi}_b = 0$ . This non-linear set of equations is solved numerically by applying a Newton-Raphson scheme. Thus, an iterative procedure is started, where at step  $i$  the values for  $a$  and  $b$  are determined by  $a_i = a_{i-1} + \Delta a_i$  and  $b_i = b_{i-1} + \Delta b_i$ , where  $\Delta a_i$  and  $\Delta b_i$  are computed by solving:

$$\begin{pmatrix} \left( \frac{\partial \hat{\varphi}_a}{\partial a} \right)_{i-1} & \left( \frac{\partial \hat{\varphi}_a}{\partial b} \right)_{i-1} \\ \left( \frac{\partial \hat{\varphi}_b}{\partial a} \right)_{i-1} & \left( \frac{\partial \hat{\varphi}_b}{\partial b} \right)_{i-1} \end{pmatrix} \begin{pmatrix} \Delta a_i \\ \Delta b_i \end{pmatrix} = - \begin{pmatrix} (\hat{\varphi}_a)_{i-1} \\ (\hat{\varphi}_b)_{i-1} \end{pmatrix},$$

where the coefficients of the matrix are given by:

$$\begin{aligned} \frac{\partial \hat{\varphi}_a}{\partial a} = & 2 \left[ |\mathcal{R}(\hat{\mathbf{u}}_0 + \hat{\mathbf{p}}_0, \hat{\mathbf{p}}_0)|^2 \|\hat{\mathbf{u}}_0\|_{\mathcal{H}}^2 - |\mathcal{R}(\hat{\mathbf{u}}_0 + \hat{\mathbf{p}}_0, \hat{\mathbf{u}}_0)|^2 \|\hat{\mathbf{p}}_0\|_{\mathcal{H}}^2 \right] \\ & + 4b \left[ \mathcal{I}m \left\{ \mathcal{R}(\hat{\mathbf{u}}_0 + \hat{\mathbf{p}}_0, \hat{\mathbf{u}}_0) \overline{\mathcal{R}(\hat{\mathbf{u}}_0 + \hat{\mathbf{p}}_0, \hat{\mathbf{p}}_0)} \right\} \|\hat{\mathbf{p}}_0\|_{\mathcal{H}}^2 \right. \\ & \quad \left. + |\mathcal{R}(\hat{\mathbf{u}}_0 + \hat{\mathbf{p}}_0, \hat{\mathbf{p}}_0)|^2 \mathcal{I}m \{ \mathcal{H}(\hat{\mathbf{u}}_0, \hat{\mathbf{p}}_0) \} \right] \\ & - 4a \left[ \mathcal{R}e \left\{ \mathcal{R}(\hat{\mathbf{u}}_0 + \hat{\mathbf{p}}_0, \hat{\mathbf{u}}_0) \overline{\mathcal{R}(\hat{\mathbf{u}}_0 + \hat{\mathbf{p}}_0, \hat{\mathbf{p}}_0)} \right\} \|\hat{\mathbf{p}}_0\|_{\mathcal{H}}^2 \right. \\ & \quad \left. - |\mathcal{R}(\hat{\mathbf{u}}_0 + \hat{\mathbf{p}}_0, \hat{\mathbf{p}}_0)|^2 \mathcal{R}e \{ \mathcal{H}(\hat{\mathbf{u}}_0, \hat{\mathbf{p}}_0) \} \right], \end{aligned}$$

$$\begin{aligned} \frac{\partial \hat{\varphi}_a}{\partial b} = & 4a \left[ \mathcal{I}m \left\{ \mathcal{R}(\hat{\mathbf{u}}_0 + \hat{\mathbf{p}}_0, \hat{\mathbf{u}}_0) \overline{\mathcal{R}(\hat{\mathbf{u}}_0 + \hat{\mathbf{p}}_0, \hat{\mathbf{p}}_0)} \right\} \|\hat{\mathbf{p}}_0\|_{\mathcal{H}}^2 \right. \\ & \quad \left. + |\mathcal{R}(\hat{\mathbf{u}}_0 + \hat{\mathbf{p}}_0, \hat{\mathbf{p}}_0)|^2 \mathcal{I}m \{ \mathcal{H}(\hat{\mathbf{u}}_0, \hat{\mathbf{p}}_0) \} \right] \\ & + 4 \left[ \mathcal{R}e \left\{ \mathcal{R}(\hat{\mathbf{u}}_0 + \hat{\mathbf{p}}_0, \hat{\mathbf{p}}_0) \overline{\mathcal{R}(\hat{\mathbf{u}}_0 + \hat{\mathbf{p}}_0, \hat{\mathbf{u}}_0)} \right\} \mathcal{I}m \{ \mathcal{H}(\hat{\mathbf{u}}_0, \hat{\mathbf{p}}_0) \} \right. \\ & \quad \left. + \mathcal{I}m \left\{ \mathcal{R}(\hat{\mathbf{u}}_0 + \hat{\mathbf{p}}_0, \hat{\mathbf{u}}_0) \overline{\mathcal{R}(\hat{\mathbf{u}}_0 + \hat{\mathbf{p}}_0, \hat{\mathbf{p}}_0)} \right\} \mathcal{R}e \{ \mathcal{H}(\hat{\mathbf{u}}_0, \hat{\mathbf{p}}_0) \} \right] \\ & + 4b \left[ \mathcal{R}e \left\{ \mathcal{R}(\hat{\mathbf{u}}_0 + \hat{\mathbf{p}}_0, \hat{\mathbf{p}}_0) \overline{\mathcal{R}(\hat{\mathbf{u}}_0 + \hat{\mathbf{p}}_0, \hat{\mathbf{u}}_0)} \right\} \|\hat{\mathbf{p}}_0\|_{\mathcal{H}}^2 \right. \\ & \quad \left. - |\mathcal{R}(\hat{\mathbf{u}}_0 + \hat{\mathbf{p}}_0, \hat{\mathbf{p}}_0)|^2 \mathcal{R}e \{ \mathcal{H}(\hat{\mathbf{u}}_0, \hat{\mathbf{p}}_0) \} \right], \end{aligned}$$

$$\begin{aligned} \frac{\partial \hat{\varphi}_b}{\partial a} = & 4 \left[ \mathcal{I}m \left\{ \mathcal{R}(\hat{\mathbf{u}}_0 + \hat{\mathbf{p}}_0, \hat{\mathbf{p}}_0) \overline{\mathcal{R}(\hat{\mathbf{u}}_0 + \hat{\mathbf{p}}_0, \hat{\mathbf{u}}_0)} \right\} \mathcal{R}e \{ \mathcal{H}(\hat{\mathbf{u}}_0, \hat{\mathbf{p}}_0) \} \right. \\ & \quad \left. - \mathcal{R}e \left\{ \mathcal{R}(\hat{\mathbf{u}}_0 + \hat{\mathbf{p}}_0, \hat{\mathbf{u}}_0) \overline{\mathcal{R}(\hat{\mathbf{u}}_0 + \hat{\mathbf{p}}_0, \hat{\mathbf{p}}_0)} \right\} \mathcal{I}m \{ \mathcal{H}(\hat{\mathbf{u}}_0, \hat{\mathbf{p}}_0) \} \right] \\ & - 4b \left[ \mathcal{R}e \left\{ \mathcal{R}(\hat{\mathbf{u}}_0 + \hat{\mathbf{p}}_0, \hat{\mathbf{u}}_0) \overline{\mathcal{R}(\hat{\mathbf{u}}_0 + \hat{\mathbf{p}}_0, \hat{\mathbf{p}}_0)} \right\} \|\hat{\mathbf{p}}_0\|_{\mathcal{H}}^2 \right. \\ & \quad \left. - |\mathcal{R}(\hat{\mathbf{u}}_0 + \hat{\mathbf{p}}_0, \hat{\mathbf{p}}_0)|^2 \mathcal{R}e \{ \mathcal{H}(\hat{\mathbf{u}}_0, \hat{\mathbf{p}}_0) \} \right] \\ & + 4a \left[ \mathcal{I}m \left\{ \mathcal{R}(\hat{\mathbf{u}}_0 + \hat{\mathbf{p}}_0, \hat{\mathbf{p}}_0) \overline{\mathcal{R}(\hat{\mathbf{u}}_0 + \hat{\mathbf{p}}_0, \hat{\mathbf{u}}_0)} \right\} \|\hat{\mathbf{p}}_0\|_{\mathcal{H}}^2 \right. \\ & \quad \left. - |\mathcal{R}(\hat{\mathbf{u}}_0 + \hat{\mathbf{p}}_0, \hat{\mathbf{p}}_0)|^2 \mathcal{I}m \{ \mathcal{H}(\hat{\mathbf{u}}_0, \hat{\mathbf{p}}_0) \} \right], \end{aligned}$$

$$\begin{aligned}
\frac{\partial \hat{\varphi}_b}{\partial b} = & -4a \left[ \mathcal{R}e \left\{ \mathcal{R}(\hat{\mathbf{u}}_0 + \hat{\mathbf{p}}_0, \hat{\mathbf{u}}_0) \overline{\mathcal{R}(\hat{\mathbf{u}}_0 + \hat{\mathbf{p}}_0, \hat{\mathbf{p}}_0)} \right\} \|\hat{\mathbf{p}}_0\|_{\mathcal{H}}^2 \right. \\
& \left. - |\mathcal{R}(\hat{\mathbf{u}}_0 + \hat{\mathbf{p}}_0, \hat{\mathbf{p}}_0)|^2 \mathcal{R}e \{ \mathcal{H}(\hat{\mathbf{u}}_0, \hat{\mathbf{p}}_0) \} \right] \\
& + 2 \left[ |\mathcal{R}(\hat{\mathbf{u}}_0 + \hat{\mathbf{p}}_0, \hat{\mathbf{p}}_0)|^2 \|\hat{\mathbf{u}}_0\|_{\mathcal{H}}^2 - |\mathcal{R}(\hat{\mathbf{u}}_0 + \hat{\mathbf{p}}_0, \hat{\mathbf{u}}_0)|^2 \|\hat{\mathbf{p}}_0\|_{\mathcal{H}}^2 \right] \\
& + 4b \left[ \mathcal{I}m \left\{ \mathcal{R}(\hat{\mathbf{u}}_0 + \hat{\mathbf{p}}_0, \hat{\mathbf{u}}_0) \overline{\mathcal{R}(\hat{\mathbf{u}}_0 + \hat{\mathbf{p}}_0, \hat{\mathbf{p}}_0)} \right\} \|\hat{\mathbf{p}}_0\|_{\mathcal{H}}^2 \right. \\
& \left. + |\mathcal{R}(\hat{\mathbf{u}}_0 + \hat{\mathbf{p}}_0, \hat{\mathbf{p}}_0)|^2 \mathcal{I}m \{ \mathcal{H}(\hat{\mathbf{u}}_0, \hat{\mathbf{p}}_0) \} \right].
\end{aligned}$$